TECHNISCHE
UNIVERSITÄT
WIEN
Vienna University of Technology

MASTERARBEIT

Particle accumulation in thermocapillary liquid bridges

ausgeführt am Institut für

Strömungsmechanik und Wärmeübertragung

der Technischen Universität Wien

unter der Anleitung von

Univ.-Prof. Dipl.-Phys. Dr. Hendrik C. Kuhlmann

durch

Ernst Hofmann, BSc.
0430537

Floßgasse 1a/19 , A–1020 Wien

Wien, im Februar 2010

Ernst Hofmann

Abstract

The motion of small, density-matched particles in a thermocapillary flow of a liquid bridge under zero gravity is considered. Due to the absence of buoyancy, the flow is driven by thermally induced Marangoni forces only. The present work proposes that the interaction of particle and liquid free surface is the key effect for the formation of so-called particle accumulation structures (PAS).

The particle motion is determined by using a simplified version of the Maxey–Riley equation. It turns out that particle trajectories and flow streamlines agree in excellent approximation for sufficiently small and density-matched tracers in zero gravity. From this observation follows a close linkage of PAS to a closed streamline in a supercritical flow. This closed streamline arises within a frame of reference that rotates at the same angular velocity as the travelling hydrothermal wave. This results in a new perception of PAS - from now on primarily a phenomenon of the hydrothermal wave's flow topology.

In supercritical flows, PAS arises as a nearly closed trajectory orbiting around a closed streamline of the supercritical flow. The attraction of all particles to the vicinity of this closed streamline is modelled by sequenced interactions of particle and liquid free surface caused by the finite size of the tracer.

The result of this work can explain particle accumulation for small, density-matched tracers in supercritical, incompressible flows in liquid bridges under zero gravity.

Kurzfassung

Die vorliegende Arbeit behandelt die Dynamik von kleinen, dichtegleichen Teilchen in der thermokapillaren Strömung einer Flüssigkeitsbrücke unter Schwerelosigkeit. Durch Fehlen natürlicher Konvektion ist die Strömung ausschließlich vom thermisch induzierten Marangonieffekt getrieben. In weiterer Folge wird ein Vorschlag erarbeitet, der die Wechselwirkung der Teilchen mit der freien Flüssigkeitsoberfläche als den Schlüsseleffekt zur Ausbildung der so genannten PAS (particle accumulation structure) identifiziert.

Die Berechnung der Teilchendynamik erfolgt mit einer vereinfachten Form der Maxey–Riley Gleichung. Die Ergebnisse zeigen, dass Teilchentrajektorien und Stromlinien für hinreichend kleine, dichtegleiche Teilchen unter Schwerelosigkeit übereinstimmen. Daraus folgt eine enge Verknüpfung von PAS mit einer geschlossenen Stromlinie der überkritischen Strömung. Diese geschlossene Stromlinie zeigt sich in einem rotierenden Bezugssystem, welches mit der gleichen Winkelgeschwindigkeit umläuft wie die Hydrothermalwelle. Damit erscheint PAS unter einem völlig neuen Blickwinkel - von nun an primär als ein Phänomen der Strömungstopologie.

Für überkritische Strömungen folgt PAS als eine nahezu geschlossene Trajektorie, die eine geschlossene Stromlinie der überkritischen Strömung umkreist. Die Attraktion der Teilchen in die Nähe dieser Stromlinie erfolgt durch aufeinanderfolgende Wechselwirkungen zwischen Teilchen und freier Oberfläche, bedingt durch die endliche Größe der Teilchen.

Die Ergebnisse dieser Arbeit geben eine Erklärung für die Akkumulation kleiner, dichtegleicher Teilchen in der überkritischen, inkompressiblen Strömung einer Flüssigkeitsbrücke unter Schwerelosigkeit.

Contents

1 Motivation

Particle-laden flows are of great importance in nature and for industrial applications. An important aspect is to understand the process of dispersion and the spatial distribution of the particulate phase. The clustering of inertial particles has recently been considered by Haller and Sapsis [1]. But even in the absence of inertial effects small particles can accumulate in an incompressible flow [2].

This work is motivated by recent results of experiments on thermocapillary flows, hence flows that are driven by thermally induced Marangoni convection only. The considered experimental setup consists of a differentially heated cylindrical liquid bridge, corresponding to the **half zone model of the floating zone process**.

In a model experiment Schwabe et al. [3] observed that tracer particles used for flow visualization did not remain well distributed in the liquid volume: under certain conditions, they accumulate along a closed line that moves in the unsteady flow. They called this phenomenon dynamic **particle accumulation structure** (PAS).

Dynamic PAS can take various shapes [4, 2, 5], depending on the Marangoni number. Typically, a closed ribbon of particles seems to be wound once or several times around a toroid and rotates like a rigid body with constant angular velocity. An experiment under nearly zero gravity conditions confirmed, that gravity is not required for PAS to occur [6]. Additionally, PAS formation is most rapid for density-matched tracers [2]. A necessary prerequisite for dynamic PAS, however, is an underlying flow in form of a pure azimuthally travelling hydrothermal wave [7, 8].

Yet, the fundamental mechanism by which PAS is realized has remained illusive.

2 Introduction to PAS

This section should give an overview of some basics concerning the phenomena of particle accumulation structures (PAS) in cylindrical liquid bridges.

2.1 Zone melting

The zone melting process or floating zone process is a technique for the fabrication of high-purity single crystals.

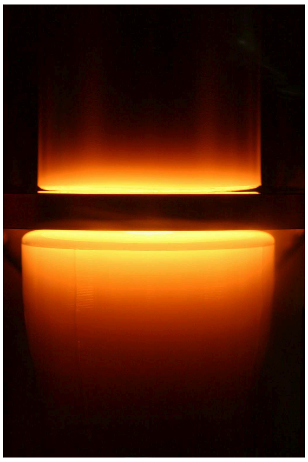

Zone melting process

In principle this crucible-free process converts a solid polycrystalline rod into a monocrystalline one. The picture shows a typical arrangement of the floating zone process consisting of an upright (slowly rotating) rod in an inert atmosphere where a small part of the rod is heated and molten inductively.
The process starts at one end of the rod melting it and exposing it to a seed crystal. Once the melt is seeded, the heater and the narrow region of molten polycrystalline material, respectively, move axially to the other end of the rod.

The achievements of zone melting are firstly a monocrystalline solidification due to the seed crystal and secondly a purification due to the chemical potential ratio which forces impurities to diffuse into the liquid, accumulate there and get transferred to the other end of the rod. Finally, the former polycrystalline rod is transformed into a high purity monocrystalline rod. Repetition of the process increases purity.

The floating zone process provides high purity at high costs. The vast majority of industrial manufactured (silicon) single crystals is obtained from the cheaper Czochralski process.

2.2 The liquid bridge

For the present work, the most interesting detail of the floating zone process is the mentioned narrow region of molten material. This molten zone represents a liquid bridge limited by solid rods on both sides, the polycrystalline rod on one side, the monocrystalline rod on the other and the liquid free surface as boundary to the ambient atmosphere. A principle sketch of the liquid bridge is shown in the central image of figure 2.1.

2.2.1 Models

The most common models for the liquid bridge of the floating zone process are the full zone model and the half zone model as shown in figure 2.1.

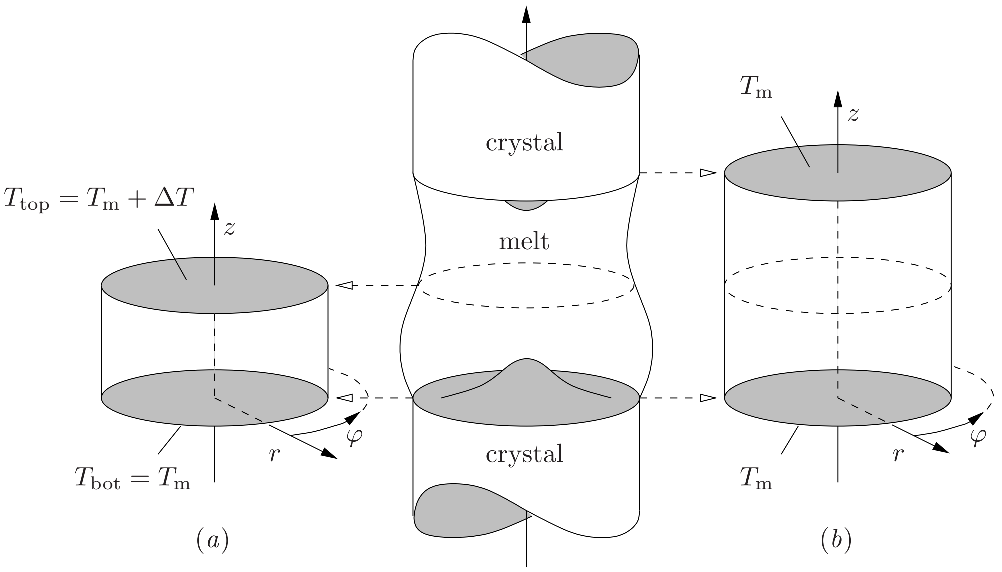

Figure 2.1: The image in the center shows the principle sketch of the liquid bridge in the floating zone crystal growth process. The half zone model is shown on the left (a) and the full zone model on the right (b). Taken from Leypoldt [9].

The most obvious simplification of both models is the assumption of a non-deformable liquid free surface. The liquid bridge is therefore modelled as a cylinder of height d and of radius R and the fundamental geometrical parameter is the **aspect ratio**

$$\Gamma = \frac{d}{R}\,. \tag{2.1}$$

With some proper boundary conditions, numerical investigations can be done for both models, but experiments are carried out using the so-called half zone model. The experimental half zone consists of a liquid bridge connecting two rods and being kept in place by its surface tension σ. Both rods are sustained at a constant temperature difference ΔT, responsible for the thermocapillary flow inside the liquid bridge after all. According to the half zone model, shown in figure 2.1, the bottom rod at melting temperature $T_{\text{bot}} = T_{\text{m}}$ represents the cold side and the top rod at $T_{\text{bot}} = T_{\text{m}} + \Delta T$ represents the hot side. The **liquid bridge** will be from now on a synonym for the half zone model of the floating zone process.

2.2.2 Convection

Before focussing on the fluid motion inside the liquid bridge, a short summary and subdivision of two of the three well-known basic principles of heat and mass transfer will be given (thermal radiation as third principle does not play any role for the present case).

1. **convective heat transfer**, thermal convection, convection - energy transfer due to mass transfer and fluid motion respectively
    a) **forced convection**, advective convection, advection: fluid motion is driven by external forces
    b) **natural convection**, free convection: fluid motion is caused by thermal induced density variations (subject to the presence of gravity)
    c) **Marangoni convection**: fluid motion is caused by surface tension gradients (Marangoni effect)
        i. thermocapillary convection: surface tension gradients are induced by temperature variations
        ii. solutocapillary convection: surface tension gradients are induced by concentration variations
2. **heat conduction**, conduction - energy transfer due to collisions of molecules

In the liquid bridge, heat transfer is a result of conduction and convection. Due to the absence of external mechanisms, convection is thermally induced only and the arising flow in the liquid bridge is therefore a result of the temperature difference ΔT between the rods. The thermally induced convection is again partly thermocapillary convection and partly natural convection. The smaller liquid bridges are, the more thermocapillary convection dominates the natural convection. This is due to the fact that the Marangoni number scales with d whereas the Rayleigh number scales with d^3. In case of zero gravity, free convection is disabled anyway and the flow is driven by the Marangoni effect only.

2.3 Thermocapillary flow structures

Numerical and experimental investigations have shown several types of thermocapillary flows. The Marangoni number

$$\mathrm{Ma} = -\frac{\partial\sigma}{\partial T^*}\frac{d}{\mu\kappa}\Delta T \;=\; \frac{\gamma d}{\rho_0\nu^2}\frac{\nu}{\kappa}\Delta T \;=\; \mathrm{Re}\,\mathrm{Pr}\,, \tag{2.2}$$

as product of thermocapillary Reynolds number

$$\mathrm{Re} = \frac{\gamma d}{\rho_0\nu^2}\Delta T \tag{2.3}$$

and Prandtl number

$$\mathrm{Pr} = \frac{\nu}{\kappa} \tag{2.4}$$

is helpful for the characterization of these thermocapillary flow structures. The given parameters are the surface tension coefficient $\gamma = -\partial\sigma/\partial T^*$ with surface tension σ and (dimensional) fluid temperature T^*, fluid density ρ_0, kinematic viscosity ν, dynamic viscosity $\mu = \nu\rho_0$, thermal diffusivity κ and reference temperature difference $\Delta T = T_{\mathrm{top}} - T_{\mathrm{bot}}$. Appendix A gives an overview of the systematics in the nomenclature, introduces the scaling procedure and summarizes all dimensional and dimensionless parameters.

The transition from the two-dimensional steady flow to a three-dimensional, time dependent oscillatory flow marks a significant change in state and is indicated by the critical Marangoni number $\mathrm{Ma_c}$ which is directly related to a critical Reynolds number $\mathrm{Re_c}$. Both can be related to a critical temperature difference ΔT_{c}, hence

$$\mathrm{Ma_c} = \mathrm{Re_c}\,\mathrm{Pr} \propto \Delta T_{\mathrm{c}}\,. \tag{2.5}$$

2.3.1 Subcritical flow state

In the subcritical case $\mathrm{Ma} < \mathrm{Ma_c}$ the flow is a steady, two-dimensional, toroidal vortex flow. A schematic sketch of this flow, also called **basic flow**, is given in figure 2.2.

2.3.2 Supercritical flow states

If the critical Marangoni number is exceeded, i.e. $\mathrm{Ma} > \mathrm{Ma_c}$, the basic flow gets unstable and disturbance waves get amplified. After a period of exponential growth the amplitude of the most dangerous perturbation saturates. The result is a three-dimensional, time

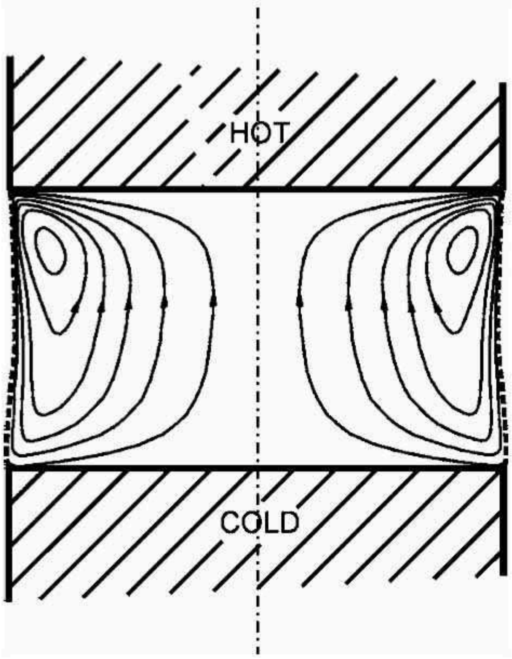

Figure 2.2: Principle sketch of the steady thermocapillary two-dimensional flow (basic flow) in a liquid bridge. Taken from Schwabe et al. [2].

dependent oscillatory flow. The arising instability at $\mathrm{Ma_c}$ is the result of a Hopf bifurcation and commonly referred to as **hydrothermal wave** (HTW) according to Smith and Davis [7]. In the region between $\mathrm{Ma_c}$ and the chaotic state there are again two distinguishable states which are called the standing wave (pulsating flow) and the travelling wave (rotating flow). The prediction which state will arise as long-time-asymptotic solution is nontrivial. For zero gravity and adiabatic boundary conditions Leypoldt et al. [10] found for $1.5 \leq \mathrm{Pr} < 7.8$ travelling waves as stable solutions immediately above the critical value $\mathrm{Re_c}$. Additionally for $4 \leq \mathrm{Pr} \leq 7$ these waves will be stabilized if the Reynolds number is further increased.

The travelling wave is the most important flow structure for PAS where in turn the standing wave state is of no interest because PAS does not develop there. More information about the standing wave can be found in Tanaka et al. [4].

Both states appear with the same azimuthal wave number m, which is called the **fundamental wave number of the HTW**. It depends primarily on the aspect ratio Γ via the relation

$$m\Gamma \approx 2.2 \,. \tag{2.6}$$

With given fundamental wave numbers $m = 1, 2, 3, \ldots$ and (2.6), the optimum aspect ratios are $\Gamma \approx 2.2, 1.1, 0.7, \ldots$. Otherwise the fundamental wave number of the HTW is not very robust and certain interactions of modes with different wave numbers can lead to a complicated flow dynamics. If the aspect ratio is chosen such that (2.6) is almost fulfilled and if in addition the Marangoni number is not too large, i.e. $\mathrm{Ma} \approx (2 \ldots 3)\mathrm{Ma_c}$, the HTW has a pure modal structure composed by the fundamental wave number and its harmonics only. In that case the flow is strictly space and time periodic. Experiments have shown that this periodicity is required for PAS to be observed. Figure 2.3 shows regions of well developed PAS in the $\Gamma-$Ma-plane.

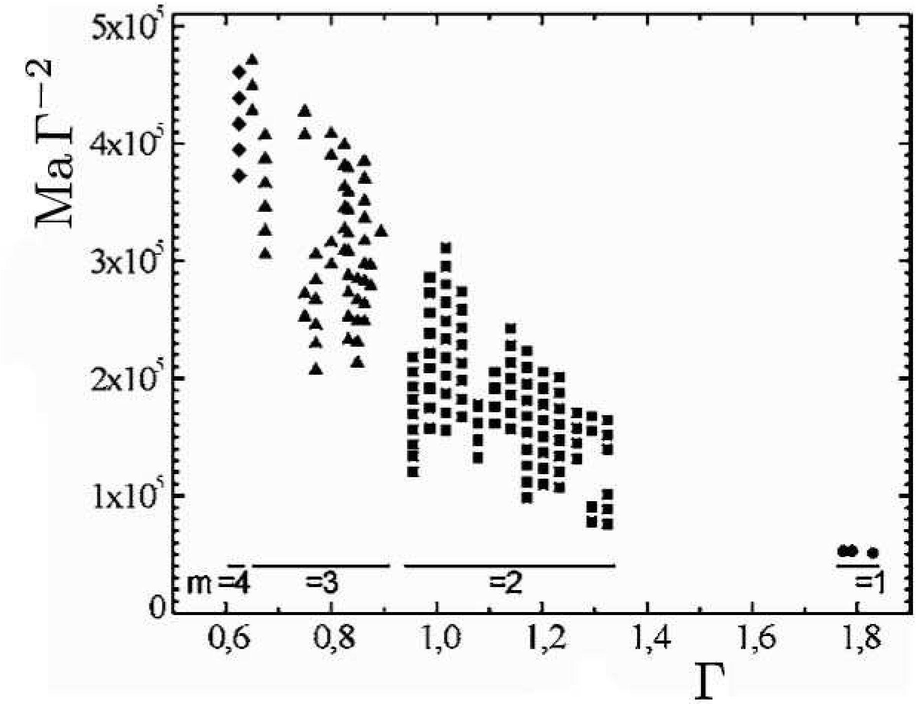

Figure 2.3: Well developed PAS regions in the $\Gamma-$Ma-plane for $\mathrm{NaNO_3}$ ($\mathrm{Pr} = 8$). The symbols indicate the fundamental wave number: $m = 1$ (●), $m = 2$ (■), $m = 3$ (▲), $m = 4$ (◆). In empty regions PAS did not develop or developed only faintly. Taken from Schwabe et al. [2].

The most important requirements for experiments on liquid bridges and PAS respectively are transparency of the fluid and moderate working temperatures. These properties are typically provided by fluids of high Prandtl numbers. Fluids of low Prandtl numbers, like metals, are unfavorable for experiments due to opacity and high melting points.

2.4 Particle accumulation structures

If PAS is observed from above (axially) it appears as a *windmill pattern* with m (fundamental wave number of HTW) blades rotating at a constant angular velocity. Figure 2.4 shows PAS with different fundamental wave numbers, corresponding to different aspect ratios Γ.

Figure 2.4: Different experimental PAS ($\mathrm{Pr} = 8$) with fundamental wave numbers. From left to right: $m = 2$, $m = 3$, $m = 4$, $m = 5$. Taken from Tanaka et al. [4].

All for now mentioned particle accumulation structures at relatively low Marangoni numbers are called by Tanaka SL-I-PAS - **spiral loop I PAS**. At higher Marangoni numbers more complicated particle accumulation structures may arise like the SL-II-PAS, shown next to the SL-I-PAS in figure 2.5 for $m = 3$. These structures typically arise at higher temperature differences, corresponding to $\mathrm{Ma} \approx 3\mathrm{Ma}_c$. Figure 2.6 shows the regions of existence for particle accumulation structures of different wave numbers and different shapes for a melt with $\mathrm{Pr} = 8$.

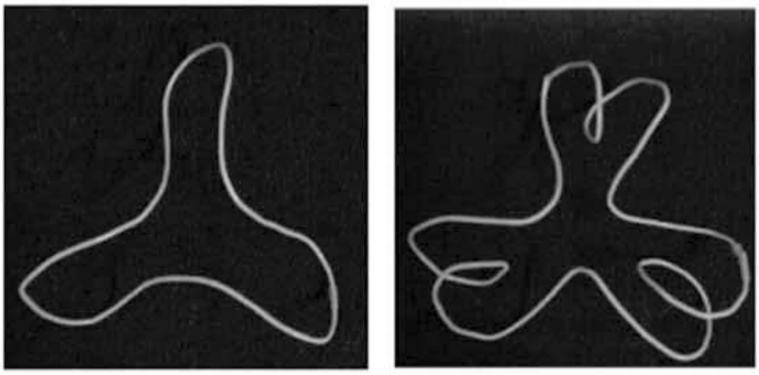

Figure 2.5: Wire models for the visualization of SL-I-PAS (left) and SL-II-PAS (right) of fundamental wave number $m = 3$. Taken from Tanaka et al. [4].

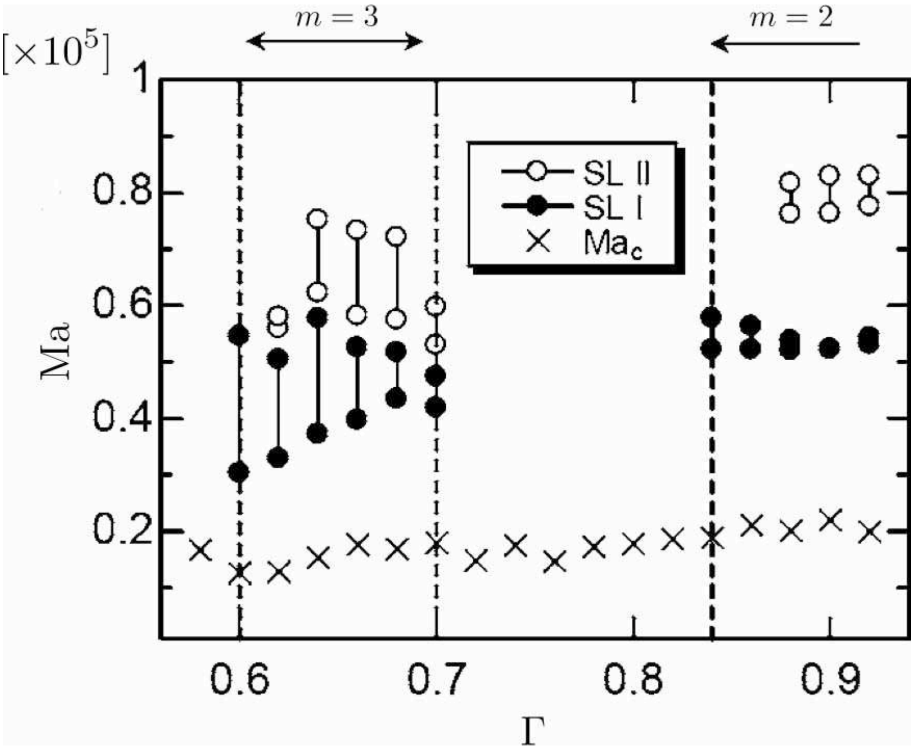

Figure 2.6: Regions of existence for SL-I-PAS and SL-II-PAS in the $\Gamma-$Ma-plane for a melt with $\mathrm{Pr} = 8$. Taken from Tanaka et al. [4].

3 The Flow

The flow in a liquid bridge is driven by two different driving forces. Firstly one finds buoyancy forces due to thermally induced density variations, hence natural convection. Secondly surface tension gradients along the liquid free surface lead to surface stresses and drive a thermocapillary flow. One speaks of thermocapillary convection, if the surface tension gradients are induced by temperature variations. For the present model, both, the density and the surface tension variations are implemented as discussed in the following section.

3.1 Oberbeck–Boussinesq approximation

The velocity field $\boldsymbol{u}(\boldsymbol{x}, t)$, the temperature field $T(\boldsymbol{x}, t)$ and the pressure field $p(\boldsymbol{x}, t)$ in a cylindrical liquid bridge are calculated using Leypoldt's code **Poseidon** [9]. The calculation bases on the Oberbeck–Boussinesq approximation, see e.g. Drazin & Reid [11], applicable for incompressible fluids and small temperature variations. This means that the temperature variation over the liquid bridge ΔT has to be small compared to the mean temperature $T_0 = (T_{\text{top}} + T_{\text{bot}})/2$, hence $\Delta T \ll T_0$. Here is a short summary of the major assumptions of the mentioned model implemented in Poseidon.

3.1.1 Fluid parameters

For the description of the fluid motion some material parameters are required. The primary material parameters of an incompressible, Newtonian fluid are the density ρ_{f} and the dynamic viscosity μ or alternatively the kinematic viscosity ν. For the liquid free surface one additionally needs the surface tension σ and the surface tension coefficient γ. The required parameters concerning heat transfer are the heat transfer coefficient h and the thermal conductivity λ or alternatively the thermal diffusivity $\kappa = \lambda/\rho_{\text{f}} c_p$ with the specific heat capacity c_p. All mentioned parameters are in general functions of temperature, pressure and concentration.

For the Oberbeck–Boussinesq approximation firstly only the temperature dependencies are taken into account. Secondly the assumption of small temperature variations motivates a first-order Taylor series approximation at the mean temperature T_0. Some analysis of the coefficient's magnitudes excuses to set all of the material parameters, except the density ρ_f and the surface tension σ, to constants, namely to their values at T_0.

The first-order Taylor series approximation of the density

$$\rho_\mathrm{f} = \rho_\mathrm{f}(T^*) \approx \rho_0 \left(1 - \beta(T^* - T_0)\right) \tag{3.1}$$

with the dimensional temperature difference $T^* - T_0$, the mean temperature T_0, the density at the mean temperature $\rho_0 = \rho_\mathrm{f}(T_0)$ and the isobaric thermal expansion coefficient at T_0

$$\beta = -\frac{1}{\rho_0} \left(\frac{\partial \rho_\mathrm{f}}{\partial T^*} \right)_{p^*} \Bigg|_{T_0} = \text{const.} \tag{3.2}$$

shows a non negligible first-order term. Nevertheless the first-order term is in turn only included in the momentum equation as the buoyancy term and the constant fraction ρ_0 is added to the hydrostatic pressure

$$\begin{aligned} -\nabla p^* + \rho_\mathrm{f} g \boldsymbol{e}_g &\approx -\nabla p^* - \rho_0 \left(1 - \beta(T^* - T_0)\right) g \boldsymbol{e}_z = \\ &= -\nabla(p^* + \rho_0 g z^*) + \rho_0 \beta g (T^* - T_0) \boldsymbol{e}_z \,. \end{aligned} \tag{3.3}$$

Similarly the first-order Taylor series approximation of the surface tension yields

$$\sigma = \sigma(T^*) \approx \sigma_0 - \gamma(T^* - T_0) \tag{3.4}$$

with the surface tension at the mean temperature $\sigma_0 = \sigma(T_0)$ and the surface tension coefficient at T_0

$$\gamma = -\frac{\partial \sigma}{\partial T^*} \bigg|_{T_0} = \text{const.} \tag{3.5}$$

The surface tension approximation is used to model the boundary condition at the liquid free surface, as can be studied in the next section.

3.1.2 Boundary conditions

Walls

The boundary conditions for the flow at the upper and lower walls, at $z = \pm 0.5$, are taken as the no-slip condition for the velocity field and temperature-matching of wall and fluid, i.e.

$$\boldsymbol{u} = 0 \qquad \text{and} \qquad T = \pm\frac{1}{2} \qquad \text{at} \qquad z = \pm\frac{1}{2} \,. \tag{3.6}$$

Constant temperature conditions imply that the heat conductivity of the support material is infinitely large. These boundary conditions are approximated experimentally by using e.g. copper as wall material.

Liquid free surface

The code of Poseidon assumes a non deformed liquid free surface, which is of perfect upright cylindrical shape. This can be achieved by vanishingly small Bond and Capillary numbers

$$\mathrm{Bo} = \frac{\rho_0 g d^2}{\sigma_0} \ll 1 \qquad , \qquad \mathrm{Ca} = \frac{\gamma \Delta T}{\sigma_0} \ll 1\,. \tag{3.7}$$

The Bond number, as measure for the importance of the capillary force compared to the gravitational force, gives an estimate to the gravitational induced surface deformation. These static surface deformations vanish completely at the absence of gravity or are negligibly small in case of a very small liquid bridge. In turn the importance of the dynamic pressure induced surface deformations can be estimated with the Capillary number.

With the assumed perfect cylindrical shape of the liquid free surface and by considering an inviscid gas, the tangential stress balance reads (see appendix B.4)

$$2\mathbf{D} \cdot \boldsymbol{e}_r + \mathrm{Re}(\mathbf{I} - \boldsymbol{e}_r\boldsymbol{e}_r) \cdot \nabla T = 0 \tag{3.8}$$

with the strain-rate tensor $\mathbf{D}$, the unity matrix $\mathbf{I}$, the outward normal unit vector $\boldsymbol{e}_r$, the dimensionless temperature difference $T = (T^* - T_0)/\Delta T$ and the thermocapillary Reynolds number (2.3). With the boundary condition for the radial velocity $u_r = 0$, one can obtain from (3.8) and (B.18) the boundary conditions for the tangential velocity field at the liquid free surface, which are

$$\left.\begin{aligned} \left(\partial_r - \frac{1}{r}\right) u_\varphi + \frac{\mathrm{Re}}{r}\partial_\varphi T = 0 \\ \partial_r u_z + \mathrm{Re}\,\partial_z T = 0 \end{aligned}\right\} \qquad \text{at} \qquad r = R = \frac{1}{\Gamma}\,. \tag{3.9}$$

These are the **thermocapillary boundary conditions**. Poseidon can also treat the liquid free surface with rigid boundary conditions, i.e. with $\boldsymbol{u} = 0$. In this case, the Marangoni convection is disabled and the flow is driven by buoyancy only.

The heat transfer between fluid and ambient gas is given by Newton's law of heat transfer

$$\partial_r T + \mathrm{Bi}(T - T_\mathrm{a}) = 0 \tag{3.10}$$

where different temperature profiles can be assumed. A common choice for the half zone model is a linear temperature profile in axial direction of the ambient gas, like $T_\mathrm{a} = z$. In the full zone model, Poseidon provides instead of the linear temperature profile of the ambient gas a Gaussian and a parabolic profile.

A nondimensional measure for the heat transfer is the Biot number

$$\mathrm{Bi} = \frac{hd}{\lambda}\,. \tag{3.11}$$

The Biot number is a measure for the strength of the heat exchange with the ambient atmosphere. Setting $\mathrm{Bi} = 0$ means adiabatic boundary conditions where the heat transfer over the liquid free surface is disabled and one speaks of thermal insulation. In this case the ambient gas temperature profile is irrelevant. In turn, $\mathrm{Bi} = \infty$ forces the temperature profile of the liquid free surface to be equal to the temperature profile of the ambient gas.

3.1.3 The dynamic equations

The dimensionless Oberbeck–Boussinesq equations for momentum and heat transfer, together with the incompressible continuity equation are

$$(\partial_t + \boldsymbol{u}\cdot\nabla)\boldsymbol{u} = -\nabla p + \nabla^2\boldsymbol{u} + \mathrm{Gr}\,T\boldsymbol{e}_z\,, \tag{3.12}$$

$$(\partial_t + \boldsymbol{u}\cdot\nabla)T = \frac{1}{\mathrm{Pr}}\nabla^2 T\,, \tag{3.13}$$

$$\nabla\cdot\boldsymbol{u} = 0\,. \tag{3.14}$$

The chosen time scale d^2/ν is the viscous diffusion time.

Together with the boundary conditions, the flow depends on **5 dimensionless parameters**. These are the fundamental aspect ratio (2.1), the Prandtl number (2.4), the thermocapillary Reynolds number (2.3), the Biot number (3.11) and the Grashof number

$$\mathrm{Gr} = \frac{\beta g d^3}{\nu^2}\Delta T\,. \tag{3.15}$$

The thermocapillary Reynolds number and the Biot number are required to model the boundary conditions at the liquid free surface.

3.2 Hydrothermal waves

For supercritical conditions, nonlinear hydrothermal waves are solutions of the problem. In a certain range of Marangoni numbers, stable hydrothermal waves of constant amplitudes exist for $t \to \infty$. Since theses waves are periodic with a fundamental azimuthal wave number, they can be represented by a Fourier series, which writes in the inertial frame of reference $\mathcal{K}$ as

$$\boldsymbol{u}(\boldsymbol{x}, t) = \sum_{n=0}^{\infty} \boldsymbol{u}_n(r, z)\, \mathrm{e}^{in(m\varphi - \omega t)} + \text{c.c.} \;=\; u_i(\boldsymbol{x}, t)\boldsymbol{e}_i \tag{3.16}$$

with complex amplitudes $\boldsymbol{u}_n$ including the relative phases of the Fourier modes. All considered Fourier components are harmonics of the HTW's fundamental mode m and propagate at the same azimuthal phase velocity (no dispersion), such that the entire flow field rotates like a rigid body with the constant angular velocity

$$\boldsymbol{\Omega} = \frac{\omega}{m}\boldsymbol{e}_z = \Omega\boldsymbol{e}_z = \text{const.} \tag{3.17}$$

The data provided by Poseidon represents a snapshot of the velocity field at $t = t_0$ (with t_0 as end of simulation) from the $\mathcal{K}-$frame of reference according to (3.16). The upper image of figure 3.1 shows such a snapshot including the rotational direction of the wave.

Due to the behaviour of the travelling HTW, a coordinate transformation

$$\boldsymbol{x} = x_i\boldsymbol{e}_i \qquad \longrightarrow \qquad \boldsymbol{x}'(t) = x'_i(t)\boldsymbol{e}'_i \tag{3.18}$$

to the rotating coordinates

$$r' = r \quad , \quad \varphi'(t) = \varphi - \Omega t \quad , \quad z' = z \quad , \tag{3.19}$$

yields the $\mathcal{K}-$field again, but now denoted in rotating coordinates

$$\boldsymbol{u}(\boldsymbol{x}') = \sum_{n=0}^{\infty} \boldsymbol{u}_n(r', z')\, \mathrm{e}^{inm\varphi'} + \text{c.c.} \;=\; u_i(\boldsymbol{x}')\boldsymbol{e}'_i\,. \tag{3.20}$$

This notation will be very helpful in section 4.3 but is to handle with care, because the executed coordinate substitution is only half way of the field transformation from $\mathcal{K}$ to $\mathcal{K}'$. The observer in $\mathcal{K}'$ notices beside the already transformed coordinates ($\boldsymbol{x} \to \boldsymbol{x}'$), transformed velocities ($\boldsymbol{u} \to \boldsymbol{u}'$) as well, i.e.

$$\boldsymbol{u}(\boldsymbol{x}') = u_i(\boldsymbol{x}')\boldsymbol{e}'_i \qquad \longrightarrow \qquad \boldsymbol{u}'(\boldsymbol{x}') = u'_i(\boldsymbol{x}')\boldsymbol{e}'_i \tag{3.21}$$

with the velocity transformation

$$\boldsymbol{u}'(\boldsymbol{x}') \;=\; \boldsymbol{u}(\boldsymbol{x}') - \boldsymbol{\Omega} \times \boldsymbol{x}' \,. \tag{3.22}$$

Finally, the velocity field $\boldsymbol{u}'(\boldsymbol{x}')$ of (3.22) represents the steady flow, as seen by a rotating observer in $\mathcal{K}'$. It is shown in the lower image of figure 3.1.

At this point some reader would probably tend to identify the images the other way round, such that the upper image shows the steady flow and lower one the flow with the travelling wave due to the strong azimuthal component - but this is a delusion. One should keep in mind, that waves, like the HTW, do not show their propagation velocity on a snapshot.

The observation of the fluid from the rotating frame of reference $\mathcal{K}'$ yields the benefit of a steady flow, but for the observation of the particle and for its equation of motion, one has to implement Coriolis- and centrifugal-forces, which is described in chapter 4.3.

Again, even if $\boldsymbol{u}(\boldsymbol{x}')$ stands for a notation in rotating coordinates $\boldsymbol{x}'(t)$, the velocity field is still observed from the $\mathcal{K}-$frame, corresponding to the space-time-point $(\boldsymbol{x}, t)$ and $\boldsymbol{x}'(t)$ respectively. On the other hand the velocity field $\boldsymbol{u}'(\boldsymbol{x}')$ is the flow described in rotating coordinates and observed from the $\mathcal{K}'-$frame. Therefore, one has to distinguish

$$\boldsymbol{u}(\boldsymbol{x}, t) = \boldsymbol{u}(\boldsymbol{x}') \qquad \text{but} \qquad \boldsymbol{u}(\boldsymbol{x}') \neq \boldsymbol{u}'(\boldsymbol{x}') \,. \tag{3.23}$$

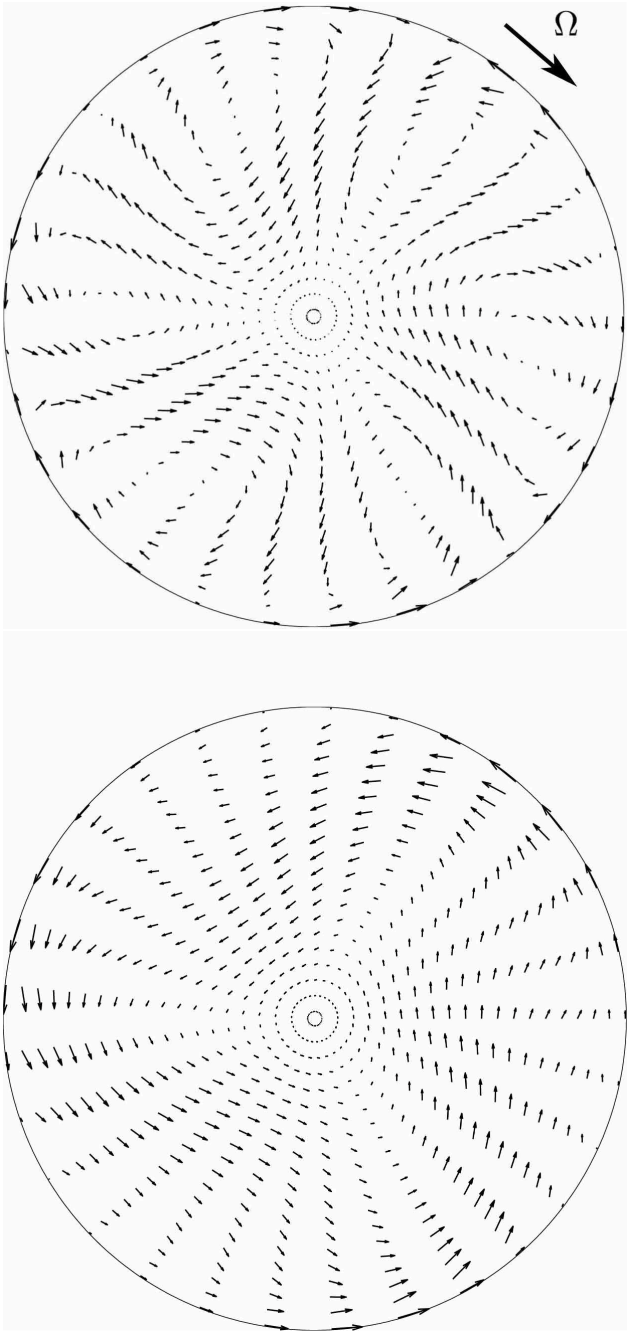

Figure 3.1: Flow field observation in $\mathcal{K}$ and $\mathcal{K}'$ at $z = 0$ from above. The flow is defined by the parameters $\Gamma = 0.66$, $\mathrm{Pr} = 4$, $\mathrm{Re} = 1800$, $\mathrm{Gr} = \mathrm{Bi} = 0$, the fundamental wave number of the HTW is $m = 3$ and its angular velocity $\Omega = -10.145$. Upper image: Snapshot of the flow field $\boldsymbol{u}(\boldsymbol{x}, t)$ for $t = t_0$ in $\mathcal{K}$. The entire flow rotates like a rigid body with the constant angular velocity Ω in the indicated direction. Lower image: Steady flow field $\boldsymbol{u}'(\boldsymbol{x}')$ in $\mathcal{K}'$.

4 The Particle

4.1 Equations of motion

The derivation of a realistic equation of motion for a small rigid spherical tracer in a nonuniform flow was provided by Maxey and Riley [12]. The following section gives an overview of their article to show the major ideas.

Following the mentioned article, all (kinematic) quantities are dimensional in this section 4.1. The dimensionless form will be worked out in section 4.2.

The considerations start in an inertial frame of reference $\mathcal{K}$. Within this frame of reference space and time is denoted with $\boldsymbol{x}$ and t, the undisturbed flow field (in absence of the particle) with $\boldsymbol{u}(\boldsymbol{x}, t)$, the position of the particle's center of mass and its velocity with $\boldsymbol{y}(t)$ and $\dot{\boldsymbol{y}}(t)$. The particle is a sphere of radius a and mass m_p. The fluid has a density of ρ_0, a dynamic viscosity of μ and a kinematic viscosity of $\nu = \mu/\rho_0$.

Due to the motion of the particle through the flow, the undisturbed flow $\boldsymbol{u}(\boldsymbol{x}, t)$ is modified, represented by the real flow $\boldsymbol{w}(\boldsymbol{x}, t)$. This modified flow has to satisfy the Navier–Stokes equations for incompressible fluids, which are

$$\rho_0 \left(\frac{\partial w_i}{\partial t} + w_j \frac{\partial w_i}{\partial x_j} \right) = -\frac{\partial p}{\partial x_i} + \mu \frac{\partial^2 w_i}{\partial x_j \partial x_j} + \rho_0 g_i \qquad \text{and} \qquad \frac{\partial w_i}{\partial x_i} = 0\,. \tag{4.1}$$

The additional conditions

$$\boldsymbol{w} = \dot{\boldsymbol{y}} + \boldsymbol{\omega} \times (\boldsymbol{x} - \boldsymbol{y}) \qquad \text{with } \boldsymbol{x} \text{ on the particle surface} \tag{4.2}$$

$$\boldsymbol{w} = \boldsymbol{u} \qquad \text{as} \quad |\boldsymbol{x} - \boldsymbol{y}\,| \to \infty \tag{4.3}$$

are the no-slip condition (4.2), that constitutes full velocity matching on the particle's surface including a rotational motion of the tracer with angular velocity $\boldsymbol{\omega}(t)$, and the second condition (4.3) ensures, that the real flow $\boldsymbol{w}(\boldsymbol{x}, t)$ and the undisturbed flow $\boldsymbol{u}(\boldsymbol{x}, t)$ are identical at infinity.

The equations of motion for a particle of mass m_p in an arbitrary flow are

$$m_\mathrm{p}\ddot{y}_i = \oint_O S_{ij} n_j \,\mathrm{d}o + m_\mathrm{p} g_i \,. \tag{4.4}$$

Hence the acceleration of a particle $\ddot{\boldsymbol{y}}(t)$ in a flow is given by the integral of the fluid stress tensor S_{ij} over the particle surface O with its outward normal vector $\boldsymbol{n}$ and the acceleration of gravity $\boldsymbol{g}$. The main challenge will be the evaluation of the fluid stress tensor.

In the next step one changes into the new frame of reference $\mathcal{K}''$, which is moving with the particle and is located in its center of mass. Within this frame of reference the space coordinate is denoted by $\boldsymbol{x}''$ and the real flow field by $\boldsymbol{w}''(\boldsymbol{x}'', t)$. In the new frame of reference $\mathcal{K}''$, the real flow is decomposed into the fraction of the undisturbed flow $\boldsymbol{u}''(\boldsymbol{x}'', t)$ and the disturbance flow $\boldsymbol{v}''(\boldsymbol{x}'', t)$ caused by the particle. Summarized, one finds for the structure of the real flow in the particle frame of reference $\mathcal{K}''$

$$\begin{aligned} \boldsymbol{x}'' &= \boldsymbol{x} - \boldsymbol{y} \,, && (4.5)\\ \boldsymbol{u}'' &= \boldsymbol{u} - \dot{\boldsymbol{y}} \,, && (4.6)\\ \boldsymbol{w}'' &= \boldsymbol{w} - \dot{\boldsymbol{y}} \;=\; \boldsymbol{u}'' + \boldsymbol{v}'' \,. && (4.7) \end{aligned}$$

In the new frame $\mathcal{K}''$ the Navier–Stokes equations for the **undisturbed flow** are

$$\rho_0 \left(\frac{\partial u_i''}{\partial t} + u_j'' \frac{\partial u_i''}{\partial x_j''} \right) = -\frac{\partial p''^{(u)}}{\partial x_i''} + \mu \frac{\partial^2 u_i''}{\partial x_j'' \partial x_j''} + \rho_0 \left(g_i - \ddot{y}_i \right) \tag{4.8}$$

and those for the **disturbance flow**

$$\rho_0 \left(\frac{\partial v_i''}{\partial t} + u_j'' \frac{\partial v_i''}{\partial x_j''} + v_j'' \frac{\partial u_i''}{\partial x_j''} + v_j'' \frac{\partial v_i''}{\partial x_j''} \right) = -\frac{\partial p''^{(v)}}{\partial x_i''} + \mu \frac{\partial^2 v_i''}{\partial x_j'' \partial x_j''} \tag{4.9}$$

with the pressure fractions $p''^{(u)}(\boldsymbol{x}'')$ and $p''^{(v)}(\boldsymbol{x}'')$ caused by the respective flow.

In equations (4.9), Maxey & Riley neglect all convective terms. This can be done in case of a sufficiently small perturbation flow due to the particle. This condition can be cast more precisely into a particle Reynolds number Re_p and a Stokes number St. With the representative velocity $W_0 = |\dot{\boldsymbol{y}} - \boldsymbol{u}|$, describing the velocity mismatch of particle and (undisturbed) flow, characteristic length and velocity of the flow L_0 and U_0 respectively, the particle Reynolds number and the (interim) Stokes number are

$$\mathrm{Re}_\mathrm{p} = \frac{a W_0}{\nu} \qquad , \qquad \mathrm{St} = \frac{a^2 U_0}{\nu L_0} = \left(\frac{a}{L_0} \right)^2 \mathrm{Re} \tag{4.10}$$

with the fluid Reynolds number $\mathrm{Re} = L_0 U_0 / \nu$.

Only if $\mathrm{Re}_\mathrm{p} \ll 1$ and $\mathrm{St} \ll 1$, the simplification of dropping the convective terms in (4.9) is justified. If the approximation should hold for high fluid Reynolds numbers as well, i.e. for $\mathrm{Re} \gg 1$, the condition of a small Stokes number implies a condition for the size of the tracer, which is then

$$\frac{a}{L_0} \ll 1\,. \tag{4.11}$$

The transformation to $\mathcal{K}''$ and the decomposition of the flow field $\boldsymbol{w}''(\boldsymbol{x}'', t)$ yields the decomposed stress tensor

$$S''_{ij} = S''^{(u)}_{ij} + S''^{(v)}_{ij} = -p''^{(u)}\delta_{ij} + \mu\left(\frac{\partial u''_i}{\partial x''_j} + \frac{\partial u''_j}{\partial x''_i}\right) - p''^{(v)}\delta_{ij} + \mu\left(\frac{\partial v''_i}{\partial x''_j} + \frac{\partial v''_j}{\partial x''_i}\right)\,. \tag{4.12}$$

The force, the fluid exerts on the sphere, can thus be decomposed into a force from the undisturbed flow $\boldsymbol{F}^{(u)}$ and a force from the disturbance flow $\boldsymbol{F}^{(v)}$, i.e.

$$\oint_O S''_{ij} n_j \,\mathrm{d}o = \oint_O \left(S''^{(u)}_{ij} + S''^{(v)}_{ij}\right) n_j \,\mathrm{d}o = F^{(u)}_i + F^{(v)}_i\,. \tag{4.13}$$

4.1.1 The force from the undisturbed flow

To calculate $\boldsymbol{F}^{(u)}$, the respective surface integral of (4.13) is transformed into a volume integral, thus

$$F^{(u)}_i = \oint_O S''^{(u)}_{ij} n_j \,\mathrm{d}o = \int_V \partial_j S''^{(u)}_{ij} \,\mathrm{d}V\,. \tag{4.14}$$

Under the assumption that the sphere is sufficiently small compared to the variations of the undisturbed flow, Maxey and Riley followed that the integrand is nearly uniform over the sphere and find the approximation

$$F^{(u)}_i = \partial_j S''^{(u)}_{ij} \int_V \mathrm{d}V = \frac{4\pi}{3} a^3 \left(-\frac{\partial p''^{(u)}}{\partial x''_i} + \mu \frac{\partial^2 u''_i}{\partial x''_j \partial x''_j}\right)\,. \tag{4.15}$$

With equations (4.8) and back transformation into the inertial frame of reference $\mathcal{K}$ by using (4.6), one finds

$$F^{(u)}_i = -m_\mathrm{f} g_i + m_\mathrm{f} \left(\frac{\partial u_i}{\partial t} + u_j \frac{\partial u_i}{\partial x_j}\right)_{\boldsymbol{x}=\boldsymbol{y}(t)} \tag{4.16}$$

with the particle-displaced fluid mass m_f. The buoyancy force $-m_\mathrm{f} g_i$ arises as part of the hydrostatic pressure distribution contained in $p''^{(u)}$.

The intermediate result for the equations of motion is then given by

$$\begin{aligned} m_\mathrm{p}\ddot{y}_i &= F_i^{(v)} + F_i^{(\mathrm{B})} + F_i^{(\mathrm{P})} = \\ &= F_i^{(v)} + (m_\mathrm{p} - m_\mathrm{f})g_i + m_\mathrm{f}\frac{\mathrm{D}u_i}{\mathrm{D}t} \,. \end{aligned} \tag{4.17}$$

The arising forces are due to buoyancy $\boldsymbol{F}^{(\mathrm{B})}$ and due to the pressure-gradient of the undisturbed flow $\boldsymbol{F}^{(\mathrm{P})}$.

Equations (4.17) use the convective derivative following a fluid element of the undisturbed flow $\boldsymbol{u}$ on its pathline, but evaluated at the instantaneous particle position, thus

$$\frac{\mathrm{D}u_i}{\mathrm{D}t} = \left(\frac{\partial u_i}{\partial t} + u_j\frac{\partial u_i}{\partial x_j}\right)_{\boldsymbol{x}=\boldsymbol{y}(t)} \tag{4.18}$$

which is to distinguish from the convective derivative following the particle through the undisturbed flow $\boldsymbol{u}$ on its trajectory, denoted by

$$\frac{\mathrm{d}u_i}{\mathrm{d}t} = \left(\frac{\partial u_i}{\partial t} + \dot{y}_j\frac{\partial u_i}{\partial x_j}\right)_{\boldsymbol{x}=\boldsymbol{y}(t)} \,. \tag{4.19}$$

The implementation of these two different derivatives into the final equations of motion is subject of rich discussions, as one can study in [12] or [13]. Nevertheless, in case of small particle Reynolds numbers, the difference between these two derivatives is negligibly small.

4.1.2 The force from the disturbance flow

For the completion of the equations of motion, the force from the disturbance flow

$$F_i^{(v)} = \oint_O S_{ij}^{\prime\prime(v)} n_j \,\mathrm{d}o \tag{4.20}$$

must still be evaluated. This requires much more effort than the evaluation of $\boldsymbol{F}^{(u)}$, as can be estimated from the result

$$\begin{aligned} F_i^{(v)} &= F_i^{(\mathrm{A})} + F_i^{(\mathrm{S})} + F_i^{(\mathrm{H})} = \\ &= -\frac{m_\mathrm{f}}{2}\left[\ddot{y}_i - \frac{\mathrm{d}}{\mathrm{d}t}\left(u_i + \frac{a^2}{10}\nabla^2 u_i\right)\right] - 6\pi a\mu\left(\dot{y}_i - u_i - \frac{a^2}{6}\nabla^2 u_i\right) - \\ &\quad - \frac{6\pi a^2\mu}{\sqrt{\pi\nu}}\int_0^t \mathrm{d}t' \frac{1}{\sqrt{(t-t')}}\frac{\mathrm{d}}{\mathrm{d}t'}\left(\dot{y}_i - u_i - \frac{a^2}{6}\nabla^2 u_i\right) \,, \end{aligned} \tag{4.21}$$

which holds in the $\mathcal{K}-$frame of reference. The terms are the added mass $\boldsymbol{F}^{(\mathrm{A})}$, viscous Stokes drag $\boldsymbol{F}^{(\mathrm{S})}$ and viscous drag from the Basset history term $\boldsymbol{F}^{(\mathrm{H})}$. The term $\sim a^2\nabla^2\boldsymbol{u}$, arising three times in the equations, is the so-called Faxén correction.

The final equations of motion for a small rigid spherical tracer in a general nonuniform flow read

$$\boxed{\begin{aligned} m_\mathrm{p}\ddot{y}_i &= F_i^{(\mathrm{B})} + F_i^{(\mathrm{P})} + F_i^{(\mathrm{S})} + F_i^{(\mathrm{A})} + F_i^{(\mathrm{H})} = \\ &= (m_\mathrm{p} - m_\mathrm{f})g_i \;+\; m_\mathrm{f}\frac{\mathrm{D}u_i}{\mathrm{D}t} \;-\; 6\pi a\mu\left(\dot{y}_i - u_i - \frac{a^2}{6}\nabla^2 u_i\right) - \\ &\quad - \frac{m_\mathrm{f}}{2}\left[\ddot{y}_i - \frac{\mathrm{d}}{\mathrm{d}t}\left(u_i + \frac{a^2}{10}\nabla^2 u_i\right)\right] - \\ &\quad - \frac{6\pi a^2\mu}{\sqrt{\pi\nu}}\int_0^t \mathrm{d}t' \frac{1}{\sqrt{(t-t')}}\frac{\mathrm{d}}{\mathrm{d}t'}\left(\dot{y}_i - u_i - \frac{a^2}{6}\nabla^2 u_i\right) \end{aligned}} \tag{4.22}$$

valid under the restrictions mentioned above,

$$\mathrm{Re}_\mathrm{p} \ll 1 \quad , \quad \mathrm{St} \ll 1 \quad , \quad \frac{a}{L_0} \ll 1\,. \tag{4.23}$$

Additionally, equations (4.22) require for their validity as initial conditions $t_0 = 0$ and particle–flow velocity-matching at t_0, i.e.

$$\dot{\boldsymbol{y}}(t_0) = \boldsymbol{u}(\boldsymbol{x}_0, t_0)|_{\boldsymbol{x}_0 = \boldsymbol{y}(t_0)}\,. \tag{4.24}$$

The field variable $\boldsymbol{u}$ in (4.22) has to be evaluated at the current particle position and is to read as

$$\boldsymbol{u} = \boldsymbol{u}(\boldsymbol{x}, t) \mathrel{\widehat{=}} \boldsymbol{u}(\boldsymbol{x}, t)|_{\boldsymbol{x} = \boldsymbol{y}(t)}\,. \tag{4.25}$$

Due to the assumption of a vanishing particle Reynolds number Re_p, the final equations of Maxey and Riley do not include finite-size particle effects. These are the Saffman effect due to the shear of the undisturbed flow and the Oseen correction to the Stokes drag, arising due to particle rotation. With the assumption of a small particle Reynolds numbers, these effects are small compared to the dominating Stokes drag and can be neglected, whereupon these conclusion holds for now only for the interior region of the liquid bridge. A detailed discussion, whether the Saffman effect plays a relevant role for the liquid bridge, where shear flows are induced by thermocapillary forces as well, can be found in Domesi [14]. He worked out the magnitude of the lift force, a generalized form of the Saffman effect, and concluded that the formation of PAS will not be affected by the lift force, but particle trajectories will deviate slightly, especially in the transient period, from those without lift force.

Moreover, particle–particle interactions are excluded anyway and particle–boundary interactions are still to work out.

4.2 Simplifications

In most cases equations (4.22) can be simplified. Following the arguments of Maxey and Riley, the Basset history force $\boldsymbol{F}^{(\mathrm{H})}$ is important in case of high-amplitude oscillating flows and corresponding to Babiano et al. [13] one can neglect the Faxén corrections, again for the case of a sufficiently small particle. Taking into account the spherical geometry of the tracer with masses $m_\mathrm{p} = V\rho_\mathrm{p}$, $m_\mathrm{f} = V\rho_0$ and volume $V = 4\pi a^3/3$, equations (4.22) reduce to

$$\left(\rho_\mathrm{p} + \frac{\rho_0}{2}\right)\frac{\mathrm{d}\dot{y}_i^*}{\mathrm{d}t^*} = -\frac{9\mu}{2a^2}\left(\dot{y}_i^* - u_i^*\right) + \rho_0\left(\frac{\mathrm{D}u_i^*}{\mathrm{D}t^*} + \frac{1}{2}\frac{\mathrm{d}u_i^*}{\mathrm{d}t^*}\right) + (\rho_\mathrm{p} - \rho_0)g_i\,. \tag{4.26}$$

In contrast to the last section 4.1, all dimensional kinematic quantities are now indicated by an asterisk and the dimensionless ones are denoted without asterisk. Dividing the equations by the fluid density ρ_0, using the density ratio $\varrho = \rho_\mathrm{p}/\rho_0$ and the common scaling method, as it is shown in appendix A.3, one finds the dimensionless form of (4.26)

$$\left(\varrho + \frac{1}{2}\right)\frac{U_0^2}{L_0}\frac{\mathrm{d}}{\mathrm{d}t}\dot{y}_i \;=\; -\frac{9\nu U_0}{2a^2}\left(\dot{y}_i - u_i\right) + \frac{U_0^2}{L_0}\left(\frac{\mathrm{D}u_i}{\mathrm{D}t} + \frac{1}{2}\frac{\mathrm{d}u_i}{\mathrm{d}t}\right) + (\varrho - 1)g_i\,. \tag{4.27}$$

Babiano et al. [13] exchanged the derivative of the flow field in the added mass term from (4.19) to (4.18). This is the correct form, already mentioned by Maxey & Riley [12]. Again, for small particle Reynolds numbers, as considered for the present investigations, these two derivatives are identical in excellent approximation anyway. The mentioned exchange leads to another simplification, which is

$$\frac{\mathrm{D}u_i}{\mathrm{D}t} + \frac{1}{2}\frac{\mathrm{d}u_i}{\mathrm{d}t} \quad\rightarrow\quad \frac{3}{2}\frac{\mathrm{D}u_i}{\mathrm{D}t}\,. \tag{4.28}$$

Introducing the Froude number and the Stokes number, which is now modified compared to (4.10),

$$\mathrm{Fr} = \frac{U_0}{\sqrt{gL_0}} = \frac{\nu}{\sqrt{gd^3}} \quad , \quad \mathrm{St} = \frac{2}{9}\frac{a^2U_0}{\nu L_0} = \frac{2}{9}\frac{a^2}{d^2}\,, \tag{4.29}$$

the equations of motion in the dimensionless form finally become

$$\boxed{\ddot{\boldsymbol{y}} \;=\; \frac{1}{\varrho + \frac{1}{2}}\left[-\frac{1}{\mathrm{St}}(\dot{\boldsymbol{y}} - \boldsymbol{u}) \;+\; \frac{3}{2}\frac{\mathrm{D}\boldsymbol{u}}{\mathrm{D}t} \;+\; \frac{\varrho - 1}{\mathrm{Fr}^2}\boldsymbol{e}_g\right]} \tag{4.30}$$

with the unit vector $\boldsymbol{e}_g$ pointing into the direction of gravity.

The equations of motion (4.30) are a system of three coupled non-linear ordinary differential equations (ODE) of second order for $y_i(t)$.

4.3 Transformations

4.3.1 Transformation to the rotating frame of reference

As mentioned in section 3.2, the flow field can be observed from a distinguished frame of reference in which the flow is steady. This is the rotating and, hence, an accelerated frame of reference $\mathcal{K}'$. For the equations of motion one has to take into account the additional Coriolis and centrifugal accelerations (see appendix B.2), so that the equations of motion in $\mathcal{K}'$ read

$$\ddot{\boldsymbol{y}}' = \underbrace{\frac{1}{\varrho+\frac{1}{2}}\left[-\frac{1}{\mathrm{St}}(\dot{\boldsymbol{y}}-\boldsymbol{u})+\frac{3}{2}\frac{\mathrm{D}\boldsymbol{u}}{\mathrm{D}t}+\frac{\varrho-1}{\mathrm{Fr}^2}\boldsymbol{e}_g\right]}_{\ddot{\boldsymbol{y}}} -2\boldsymbol{\Omega}\times\dot{\boldsymbol{y}}'-\boldsymbol{\Omega}\times(\boldsymbol{\Omega}\times\boldsymbol{y}')\,. \tag{4.31}$$

The interpretation of these new equations must be considered with caution, because they contain quantities from both frames of reference, $\mathcal{K}$ and $\mathcal{K}'$. In particular the treatment of the field variable $\boldsymbol{u}$ requires some diligent review. For a consistent differential equation, all quantities concerning the particle have to be exclusively denoted in the $\mathcal{K}'-$frame. For now all underbraced terms of (4.31), representing the acceleration $\ddot{\boldsymbol{y}}(t)$, are to read in the $\mathcal{K}-$frame.

The Stokes term of (4.31) accounts for the particle–flow velocity-mismatch in $\mathcal{K}$, which is, as in general relative velocities are, invariant under coordinate transformation and reads for both frames of reference

$$\dot{\boldsymbol{y}}-\boldsymbol{u} \;=\; \underbrace{\dot{\boldsymbol{y}}(t)-\boldsymbol{u}(\boldsymbol{x},t)|_{\boldsymbol{x}=\boldsymbol{y}(t)}}_{\text{in }\mathcal{K}} \;=\; \underbrace{\dot{\boldsymbol{y}}'(t)-\boldsymbol{u}'(\boldsymbol{x}')|_{\boldsymbol{x}'=\boldsymbol{y}'(t)}}_{\text{in }\mathcal{K}'} \;=\; \dot{\boldsymbol{y}}'-\boldsymbol{u}'\,. \tag{4.32}$$

The transformation of the substantive derivative is shown in appendix B.3 and reads as

$$\frac{\mathrm{D}\boldsymbol{u}}{\mathrm{D}t} = \Big(\boldsymbol{u}'\cdot\nabla'\boldsymbol{u}'+2\boldsymbol{\Omega}\times\boldsymbol{u}'+\boldsymbol{\Omega}\times(\boldsymbol{\Omega}\times\boldsymbol{x}')\Big)_{\boldsymbol{x}'=\boldsymbol{y}'(t)} \tag{4.33}$$

Due to the assumed orientation of the liquid bridge, the direction of gravity, the cylinder axis and therefore the rotational axis match, i.e.

$$\boldsymbol{e}_g = -\boldsymbol{e}_z = -\boldsymbol{e}_z' \qquad \Longrightarrow \qquad \Omega = \Omega'\,. \tag{4.34}$$

Starting from the $\mathcal{K}-$frame equations of motion (4.30) one ends up at the final $\mathcal{K}'-$frame equations:

$$\begin{aligned}\ddot{\boldsymbol{y}}' = \frac{1}{\varrho+\frac{1}{2}}\left[-\frac{1}{\mathrm{St}}(\dot{\boldsymbol{y}}'-\boldsymbol{u}')+\frac{3}{2}\boldsymbol{u}'\cdot\nabla'\boldsymbol{u}'-\frac{\varrho-1}{\mathrm{Fr}^2}\boldsymbol{e}_z\right]-2\boldsymbol{\Omega}\times\left(\dot{\boldsymbol{y}}'-\frac{3}{2\varrho+1}\boldsymbol{u}'\right)- \\ -\boldsymbol{\Omega}\times(\boldsymbol{\Omega}\times\boldsymbol{y}')\left(1-\frac{3}{2\varrho+1}\right)\qquad\text{with}\qquad \boldsymbol{u}'=\boldsymbol{u}'(\boldsymbol{x}')|_{\boldsymbol{x}'=\boldsymbol{y}'(t)}\,.\end{aligned}\tag{4.35}$$

Due to the output format of Poseidon $\boldsymbol{u}(\boldsymbol{x}')$, representing the velocity field in $\mathcal{K}$ but described in rotating coordinates, the alternative version of the substantive derivative (B.40) seems to be more practical and the equations of motion follow as

$$\begin{aligned}\ddot{\boldsymbol{y}}' = \frac{1}{\varrho+\frac{1}{2}}\left\{-\frac{1}{\mathrm{St}}\left(\dot{\boldsymbol{y}}'-(\boldsymbol{u}-\boldsymbol{\Omega}\times\boldsymbol{y}')\right)+\frac{3}{2}\Big[(\boldsymbol{u}-\boldsymbol{\Omega}\times\boldsymbol{y}')\cdot\nabla'\boldsymbol{u}+\boldsymbol{\Omega}\times\boldsymbol{u}\Big]-\frac{\varrho-1}{\mathrm{Fr}^2}\boldsymbol{e}_z\right\}- \\ -2\boldsymbol{\Omega}\times\dot{\boldsymbol{y}}'-\boldsymbol{\Omega}\times(\boldsymbol{\Omega}\times\boldsymbol{y}')\qquad\text{with}\qquad \boldsymbol{u}=\boldsymbol{u}(\boldsymbol{x}')|_{\boldsymbol{x}'=\boldsymbol{y}'(t)}\end{aligned}\tag{4.36}$$

where all quantities concerning the particle are again given in $\mathcal{K}'$ but the flow is now described in the inertial frame of reference in rotating coordinates, hence $\boldsymbol{u}=\boldsymbol{u}(\boldsymbol{x}')$, as used by Poseidon.

4.3.2 Transformation to cylindrical coordinates

Expressing the time derivatives of the position vector and the convective derivative in cylindrical coordinates (see appendix B.1), separation of the cylindrical unit vectors and ordering by the second derivatives, equations (4.36) get to

$$\begin{aligned}\ddot{r}' &= \frac{1}{\varrho+\frac{1}{2}}\left\{-\frac{1}{\mathrm{St}}(\dot{r}'-u_{r'})+\right. \\ &\qquad\left.+\frac{3}{2}\left[\left(u_{r'}\partial_{r'}+\left(\frac{u_{\varphi'}}{r'}-\Omega\right)\partial_{\varphi'}+u_{z'}\partial_{z'}\right)u_{r'}-\frac{u_{\varphi'}^2}{r'}\right]\right\}+r'\left(\dot{\varphi}'+\Omega\right)^2\,, \\ \ddot{\varphi}' &= \frac{1}{\varrho+\frac{1}{2}}\left\{-\frac{1}{\mathrm{St}}\left(\dot{\varphi}'-\left(\frac{u_{\varphi'}}{r'}-\Omega\right)\right)+\right. \\ &\qquad\left.+\frac{1}{r'}\frac{3}{2}\left[\left(u_{r'}\partial_{r'}+\left(\frac{u_{\varphi'}}{r'}-\Omega\right)\partial_{\varphi'}+u_{z'}\partial_{z'}\right)u_{\varphi'}+\frac{u_{r'}u_{\varphi'}}{r'}\right]\right\}-\frac{2\dot{r}'}{r'}(\dot{\varphi}'+\Omega)\,, \\ \ddot{z}' &= \frac{1}{\varrho+\frac{1}{2}}\left\{-\frac{1}{\mathrm{St}}(\dot{z}'-u_{z'})+\frac{3}{2}\left(u_{r'}\partial_{r'}+\left(\frac{u_{\varphi'}}{r'}-\Omega\right)\partial_{\varphi'}+u_{z'}\partial_{z'}\right)u_{z'}-\frac{\varrho-1}{\mathrm{Fr}^2}\right\}\,.\end{aligned}\tag{4.37}$$

4.3.3 Transformation to ODEs of first order

For any MATLAB-solver `odeXX`, one needs to transform the system of 3 ODEs of second order in a system of 6 ODEs of first order. This is done with the substitutions

$$\begin{array}{ccccccccccc} r' & \rightarrow & y_1 & , & \varphi' & \rightarrow & y_2 & , & z' & \rightarrow & y_3 \; , \\ \dot{r}' & \rightarrow & y_4 & , & \dot{\varphi}' & \rightarrow & y_5 & , & \dot{z}' & \rightarrow & y_6 \; . \end{array} \tag{4.38}$$

Due to computational economy, the constant factors

$$C_\varrho = \frac{1}{\varrho + \frac{1}{2}} \quad , \quad C_{\mathrm{St}} = -\frac{1}{\mathrm{St}} \quad , \quad C_{\mathrm{Fr}} = \frac{\varrho - 1}{\mathrm{Fr}^2} \tag{4.39}$$

are computed only once and the repeatedly used factors

$$\bar{y}_1 = \frac{1}{r'} \quad , \quad y_5^* = \dot{\varphi}' + \Omega \quad , \quad \Omega^* = \frac{u_{\varphi'}}{r'} - \Omega \tag{4.40}$$

are computed once for each integration step.

For convenience, all primed characters are renamed from now, i.e.

$$\partial_{\xi'} \quad \rightarrow \quad \partial_\xi \qquad \text{and} \qquad u_{\xi'} \quad \rightarrow \quad u_\xi \qquad \text{with} \qquad \xi = r, \varphi, z \, . \tag{4.41}$$

With all definitions from above, one finds the required ODE-system of first order

$$\boxed{\begin{aligned} \dot{y}_1 &= y_4 \; , \\ \dot{y}_2 &= y_5 \; , \\ \dot{y}_3 &= y_6 \; , \\ \dot{y}_4 &= C_\varrho C_{\mathrm{St}} \left(y_4 - u_r \right) + 1.5\, C_\varrho \left(u_r \partial_r u_r + \Omega^* \partial_\varphi u_r + u_z \partial_z u_r - \bar{y}_1 u_\varphi^2 \right) + y_1 y_5^{*2} \; , \\ \dot{y}_5 &= C_\varrho C_{\mathrm{St}} \left(y_5 - \Omega^* \right) + 1.5\, C_\varrho \bar{y}_1 \left(u_r \partial_r u_\varphi + \Omega^* \partial_\varphi u_\varphi + u_z \partial_z u_\varphi + \bar{y}_1 u_r u_\varphi \right) - 2 \bar{y}_1 y_4 y_5^* \; , \\ \dot{y}_6 &= C_\varrho C_{\mathrm{St}} \left(y_6 - u_z \right) + 1.5\, C_\varrho \left(u_r \partial_r u_z + \Omega^* \partial_\varphi u_z + u_z \partial_z u_z \right) - C_\varrho C_{\mathrm{Fr}} \, . \end{aligned}} \tag{4.42}$$

4.4 Particle–boundary interaction

The equations of motion are valid for the interior region of the liquid bridge. In case the particle reaches any physical boundary of the liquid bridge, which are in vertical direction the bottom and top disks at $z = \pm 1/2$ and in radial direction the liquid free surface at

$r = R = 1/\Gamma$, the model must be modified. This is in detail contents of section 5.2.3. Here only some more quantities concerning the particle–boundary interaction are introduced.

From a given Stokes number St, the common scales (see appendix A.3) and with equation (4.29), one can easily derive the dimensionless particle radius a/d as

$$\mathrm{St} = \frac{2a^2 U_0}{9\nu L_0} = \frac{2a^2}{9d^2} \quad \longrightarrow \quad \frac{a}{d} = \sqrt{\frac{9}{2}\mathrm{St}}\,. \tag{4.43}$$

Due to the finite size of the particle, the maximum reachable (dimensionless) positions for the particle's center of mass are the **contact radius** $R^\dagger$ in radial direction and the **vertical contact position** $z^\dagger$, which read

$$R^\dagger = \frac{R}{d} - \frac{a}{d} \qquad \text{and} \qquad z^\dagger = \frac{1}{2} - \frac{a}{d}\,. \tag{4.44}$$

Figure 4.1 is a principle sketch to illustrate the introduced contact boundaries, shown as dashed lines.

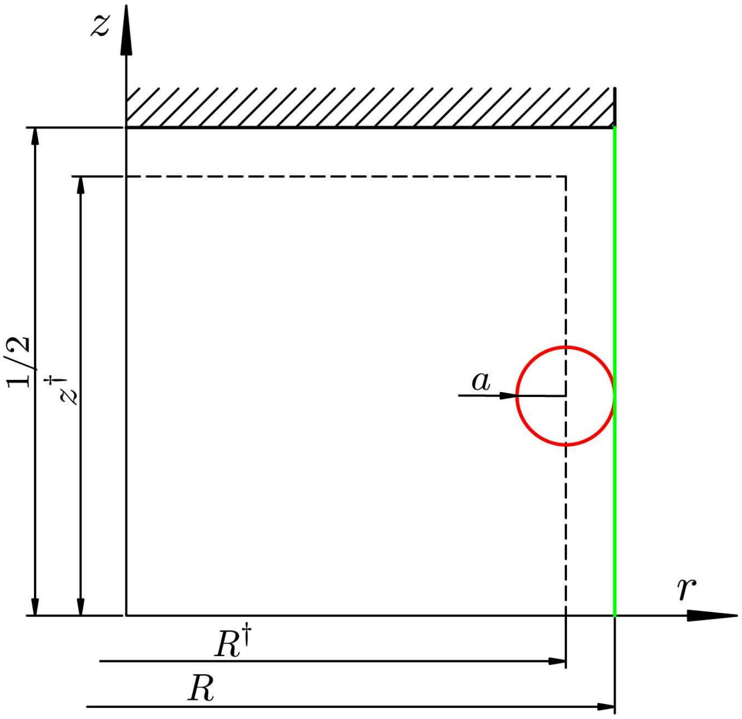

Figure 4.1: Principle sketch with the maximum reachable positions (dashed lines) for a spherical particle (red) of radius a. The physical boundaries are the liquid free surface (green) at $r = R$ and in this case the upper disk (hatched) at $z = 1/2$. The contact boundaries are $R^\dagger$ and $z^\dagger$.

5 Numerics

The assumed one-way coupling and the structure of the travelling hydrothermal wave allows to decouple the calculations of flow field and particle trajectory. Firstly the flow field is determined with Leypoldt's code Poseidon [9] (FORTRAN 90) and secondly the trajectories are derived with MTrace (MATLAB) which was developed exclusively for this purpose. The following chapter gives an overview on the basic internal structure of both simulation programmes.

5.1 Poseidon

Poseidon integrates the Oberbeck–Boussinesq equations by a finite volume method in radial and axial direction coupled to a pseudo-spectral Fourier method in azimuthal direction on a so-called staggered grid. The velocity field $\boldsymbol{u}(\boldsymbol{x}, t)$ is represented by a sequence of flow states at each time step provided within the inertial frame of reference $\mathcal{K}$ in cylindrical coordinates on the staggered grid, hence for $t = t_0$ this is

$$\boldsymbol{u}(\boldsymbol{x}, t_0) = u_r(r, \varphi, z, t_0)\boldsymbol{e}_r + u_\varphi(r, \varphi, z, t_0)\boldsymbol{e}_\varphi + u_z(r, \varphi, z, t_0)\boldsymbol{e}_z \,. \tag{5.1}$$

5.1.1 Staggered grid

For a staggered grid the five field variables $u_r, u_\varphi, u_z, T, p$ are not given at every grid point, but rather in a staggered fashion as shown in figure 5.1. The thin lines appearing in the figure are the cell boundaries of the discrete mesh generated by Poseidon. One can easily notice that the pressure p, the temperature T and the azimuthal velocity u_φ are not given on the cell boundaries but in the center of each cell. On the other hand the radial velocity u_r is only given on the vertical cell boundaries and the axial velocity u_z is only given on the horizontal cell boundaries. Due to the staggered grid, all matrices holding the respective flow variables are of different size, which yields some more effort for the data management (see appendix C.2).

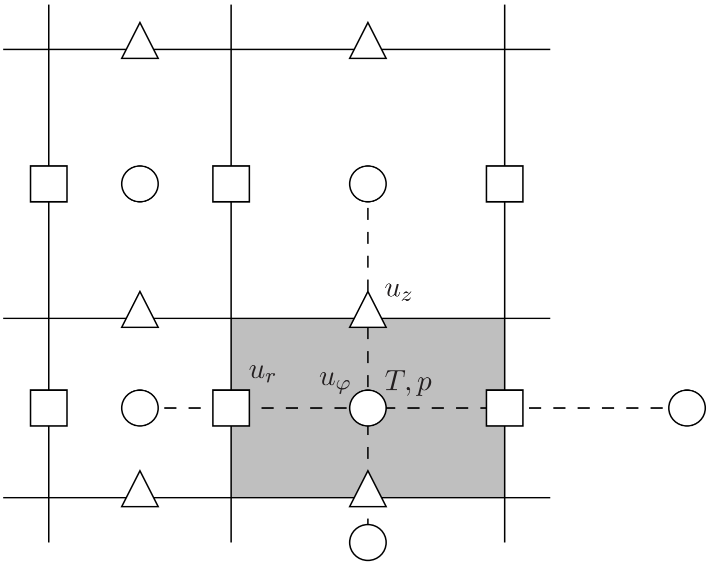

Figure 5.1: Staggered grid with the arrangement of all flow field variables, (○ - u_φ, T, p), (△ - u_z) and (□ - u_r). Taken from Leypoldt [9].

5.1.2 Pseudo-spectral method

In any case, the azimuthal periodicity of the arising flow calls for a spectral method in φ. The finite azimuthal grid resolution implies a truncation of the (theoretically infinite) Fourier series and this truncation error becomes manifest as the so-called **aliasing effect**. Hence, all Fourier components with wave numbers higher than the maximum representable wave number appear as contributions to lower but represented wave numbers. Poseidon has no implemented strategy to suppress aliasing. Nevertheless, the effects due to aliasing can be reduced by increasing the azimuthal resolution, such that any flow can be achieved with an adequate accuracy by using a moderate azimuthal grid resolution N_φ.

If the Reynolds number is slightly above the critical value, three-dimensional flows in liquid bridges of aspect ratios $\Gamma = \mathcal{O}(1)$ contain only a small number of relevant Fourier modes. If the Reynolds number is increased, higher Fourier modes are excited and have to be taken into account. This is done by increasing the azimuthal resolution N_φ. For instance, the arising HTW in a liquid bridge of aspect ratio $\Gamma = 0.66$ has the fundamental wave number $m = 3$. For covering the first two harmonics, i.e. $n = \{0, 3, 6\}$, one will need at least an azimuthal grid resolution of $N_\varphi = 2(n_{\max} + 1) = 14$.

Aliasing mainly affects those modes with higher wave numbers. For a quantitative estimate onto the aliased contributions, Leypoldt [9] compared the results of two simulations with different azimuthal grid resolutions ($N_\varphi = 14$ and $N_\varphi = 22$) for a liquid bridge of aspect ratio $\Gamma = 1$ and $\mathrm{Re} \approx 1.5\mathrm{Re}_c$. To be more precise, he compared the amplitudes of all harmonics at a certain position. He found a relative discrepancy of $1\,\%$ for the fundamental mode and large relative errors for all higher harmonics due to aliasing. However, the amplitudes of the higher harmonics are small compared to the amplitude of the fundamental mode and therefore the absolute error is still in the range of $1\,\%$.

The extensive relative errors caused by aliasing due to an undersized azimuthal grid resolution limits quantitative statements for higher harmonics. Nevertheless, the small absolute error shows that the character of the flow is not influenced essentially by aliasing. For the subsequent reduction of the aliasing effect, a post filtering procedure is applied to the velocity field as discussed in section 5.2.1.

5.2 MTrace

The trajectory solver MTrace is highly dominated by the implementation of several MATLAB built-in functions. The mentioned functions are `fft` for the filtering procedure of the flow field (see 5.2.1), the 3D-interpolation function `interp3` together with the piecewise cubic Hermite interpolation function `pchip` for the interpolation procedure of the flow field (see 5.2.4) and the ODE-solver itself, whereby `ode15s` was selected (see 5.2.2).

5.2.1 Mode filter

As already depicted in section 5.1.2 Poseidon's pseudo-spectral method is subject to the aliasing effect. For the present case one knows that a pure travelling wave is of the form (3.16), composed by the HTW's fundamental mode and its harmonics only. With an adequate azimuthal grid resolution the contributions due to aliasing are only small and the post-filtering procedure results in a pure hydrothermal wave composed by its (major) harmonics only. Even if the filtering procedure eliminates all non-harmonics, the contributions due to aliasing to the HTW's harmonics are not removable subsequently. Again, for a proper azimuthal grid resolution, these fractions are only small. Figures 5.2 and 5.3 show a representative result of a Fourier transform, here of the radial velocity component u_r, as an example for the magnitudes of all Fourier components.

The filtering procedure is carried out as follows for all field variables $(u_r, u_\varphi, u_z, T, p)$:

- Start at the first field variable of Poseidon's original flow data, like u_r.

- Transform the selected flow variable to Fourier space by passing the azimuthal data set of every single $(r, z)-$tuple to MATLAB's built-in function `fft`.
- Apply inverse Fourier transform back to position space again according to equation (B.70) but only by using user-selected wave numbers, for instance $n = \{0, 3, 6, 9\}$.

5.2.2 Integration

Generally a Runge–Kutta based ODE-solver is in most cases a good guess for a first try. Also MATLAB recommends to start with `ode45`, a one-step solver based on an explicit Runge–Kutta formula, the Dormand–Prince pair, which works best for non-stiff systems [15]. In case of stiff systems, MATLAB recommends `ode15s`, a multistep solver based on the numerical differentiation formulas (NDF) or optionally working with the backward differentiation formulas (BDF), also referred to as Gear's method [15].

The dominating Stokes term in the equation of motion is a strong indication for a stiff system. A comparison of the integration times of `ode45` and `ode15s` shows in fact an advantage by using `ode15s`. The results are qualitatively identical, but integration is much faster and therefore all calculations in this work are done with `ode15s`. A good description of this solver including a mathematical discussion of its algorithm can be found in Haidinger [16].

Based on a comparison with a high accuracy reference calculation, where both tolerances were set to 10^{-12}, the ODE-solver's standard tolerances are chosen as

$$\mathrm{RelTol} = 10^{-4} \qquad \text{and} \qquad \mathrm{AbsTol} = 10^{-6} \tag{5.2}$$

which yield qualitatively identical results compared to the high accuracy integration.

As already mentioned in section 4.4 the particle's domain of definition is limited by the contact boundaries $R^\dagger$ and $z^\dagger$. For the detection of any particle–boundary interaction, MATLAB's built-in ODE-subroutine `events` is used, a very easy but powerful tool and essential for post processing as well. This subroutine calls after every successful integration step a user-defined function and proves all conditions of this function to be either true or false. If any condition is true, an so-called event is detected, for instance a particle–boundary interaction. In any case this event will be documented by writing the recent state vector to `yeout` and an integer to `ieout`, which stands for a simple code to identify the respective event. After that, the ODE-solver checks whether the event results in the truncation of integration (and reinitialization) or if the event is designated for documentation purposes only and integration continues as usual.

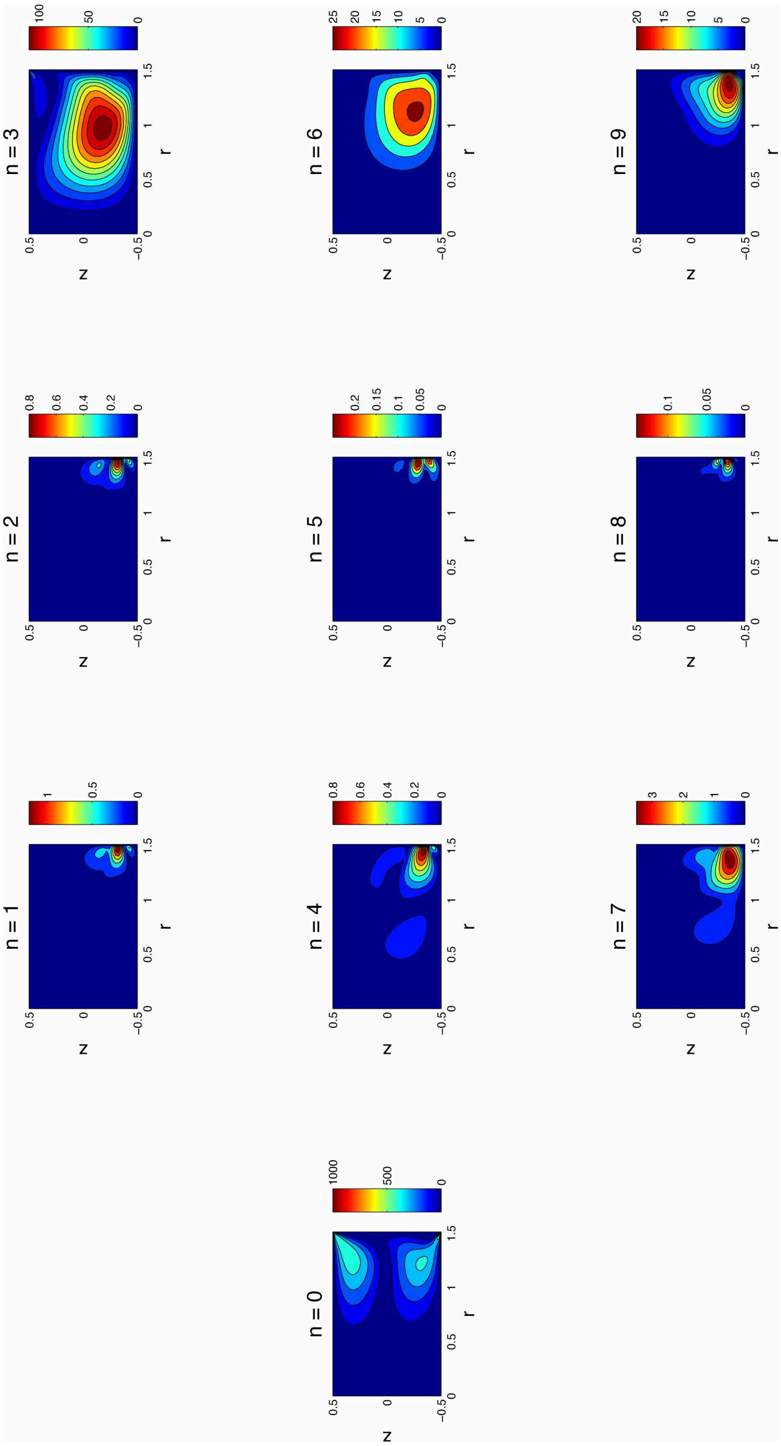

Figure 5.2: Fourier amplitudes $|\tilde{a}_n|$ for wave numbers $n = \{0 \ldots 9\}$ of the radial velocity u_r of a flow determined by $\Gamma = 0.66$, $\mathrm{Pr} = 4$, $\mathrm{Re} = 1800$, $\mathrm{Gr} = \mathrm{Bi} = 0$. Fundamental wave number of the HTW is $m = 3$ and azimuthal resolution is $N_\varphi = 22$.

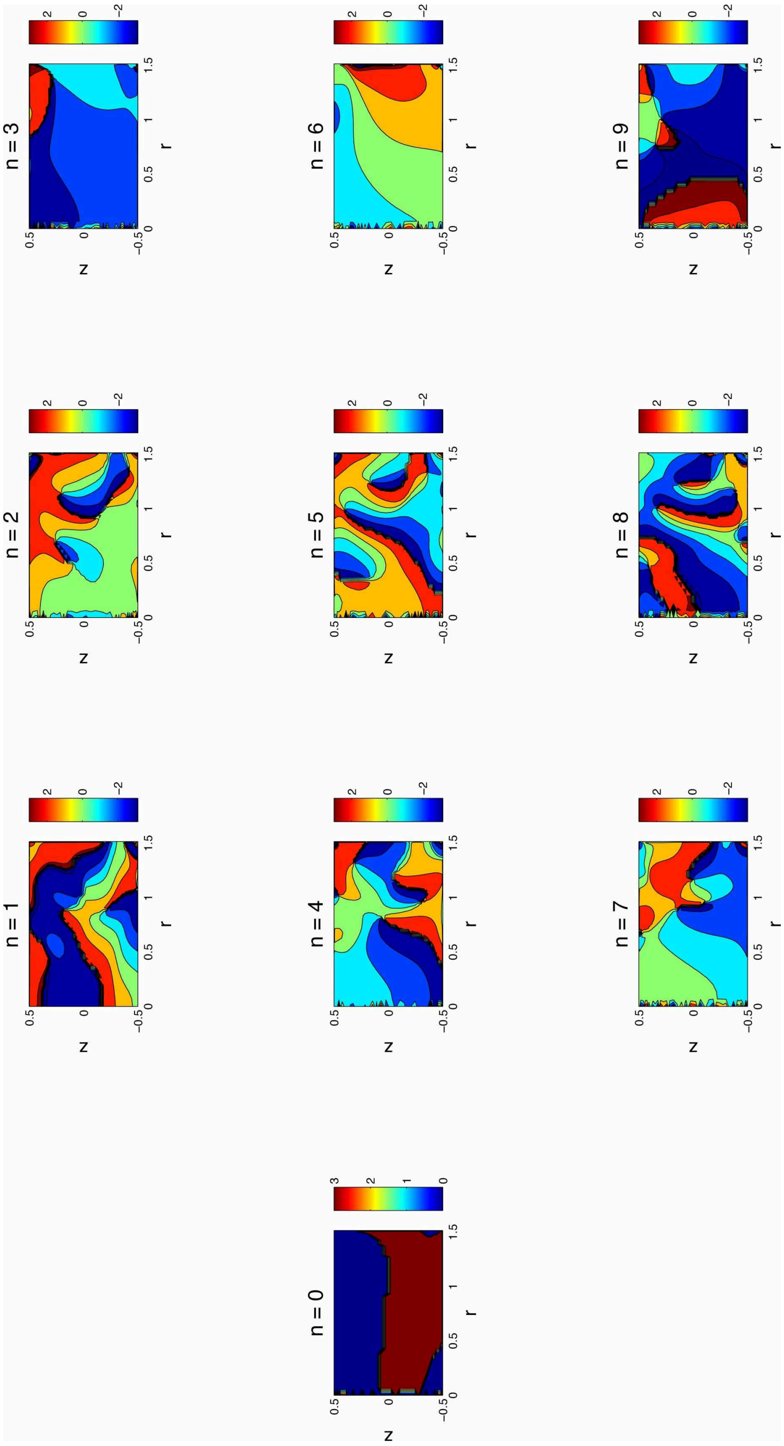

Figure 5.3: Fourier phases φ_n for wave numbers $n = \{0 \dots 9\}$ of the radial velocity u_r of a flow determined by $\Gamma = 0.66$, $\mathrm{Pr} = 4$, $\mathrm{Re} = 1800$, $\mathrm{Gr} = \mathrm{Bi} = 0$. Fundamental wave number of the HTW is $m = 3$ and azimuthal resolution is $N_\varphi = 22$.

5.2.3 Particle–boundary interaction model

The particle–boundary interaction, especially the interaction with the liquid free surface, is a complicated process. Realistic models of particle–free surface interactions must take into account the wetting properties (contact angle) and surface deflections as presented in Vassileva et al. [17] or Do-Quang et al. [18].

The numerical effort for the implementation of these models is very high. Therefore, one shall implement a simple but practical approach which allows to explicitly compute trajectories of many different particles, like it was already done by Domesi [14]. Simple particle–boundary interaction models has also been used by Melnikov [19] and Kawamura [20].

It turns out that the simple interaction models implemented in MTrace, both discussed in more detail below, lead to results that compare very well with experiments. Both models assume the limit case of perfect particle–fluid wettability, corresponding to the contact angle $\theta = 0$.

Fully elastic reflection model

Probably the simplest and most obvious model for a particle–surface interaction is the **fully elastic reflection model** (FER-model). In this model the respective velocity component gets inverted ($\dot{y}_\xi \to -\dot{y}_\xi$) as the particle hits any surface in $\xi-$direction. The particle momentum is fully conserved and the resulting movement of the particle corresponds to that of a bouncing ball.

Within the FER-model and exemplarily for the vertical boundary interaction at $\pm z^\dagger$ one has:

1. If $|z| = z^\dagger \Longrightarrow$ terminate ODE–solver.
2. Reinitialization of the particle state by taking the last value of the solution and overwrite the vertical velocity by $\dot{z} = -\dot{z}$.
3. Restart ODE–solver with new initial state vector.

Even if the free surface is considered as non deformable, the PER-model seems to be far from a realistic description because the movement of a small particle ($\mathrm{St} \ll 1$) in a fluid is highly dissipative due to the Stokes drag ($\propto \mathrm{St}^{-1}$). The relaxation of the assumption of a conserved radial momentum leads to the partially elastic reflection model.

Partially elastic reflection model

With the **partially elastic reflection model** (PER-model) the radial momentum is no longer conserved. It yields results in excellent agreement to the FER-model but its numerics is more efficient. If a particle hits any boundary in $\xi-$direction, the respective velocity component is set to zero ($\dot{y}_\xi \to 0$) and additionally the respective acceleration component is forced to zero ($\ddot{y}_\xi \to 0$) as long as the particle acceleration points into the outward direction of the liquid bridge. Within the PER-model the particle momentum is not fully conserved, because the $\xi-$component gets annihilated.

Within the PER-model and exemplarily for the radial boundary interaction at $R^\dagger$ one has:

1. If $r = R^\dagger \implies$ terminate ODE–solver.
2. Reinitialization of the particle state by taking the last value of the solution and overwrite the radial velocity by $\dot{r} = 0$.
3. Restart ODE–solver with new initial state vector.
4. Calculation of $\ddot{r}$
5. If $\ddot{r} > 0 \quad \implies \quad \ddot{r} = 0$

Comparison of both models

Both considered boundary interaction models are numerically very efficient and the results are close to experimental evidence. Figure 5.4 shows the projection of a representative particle trajectory derived in both models. In view of the dimensionless particle radius of only $a/d = 0.02$ and the radial scale, one can easily see that the results of both models are qualitatively the same.

The upper images of figure 5.5 show again the trajectories of figure 5.4 including all surface collision and release points. The lower images are close-ups of the upper (left) and lower (right) interaction regions where the characteristic movement of the particle is illustrated for both models. Due to the annihilation of the radial momentum in the PER-model it is clear that the final surface release point has to be different in general.

In consideration of the negligible discrepancy of the results of both models, the decisive point for the final choice of the boundary interaction model is the numerical efficiency, where finally the PER-model is to favour. Furthermore the assumption of the PER-model seems to be more physical than the assumed conserved radial momentum of the FER-model.

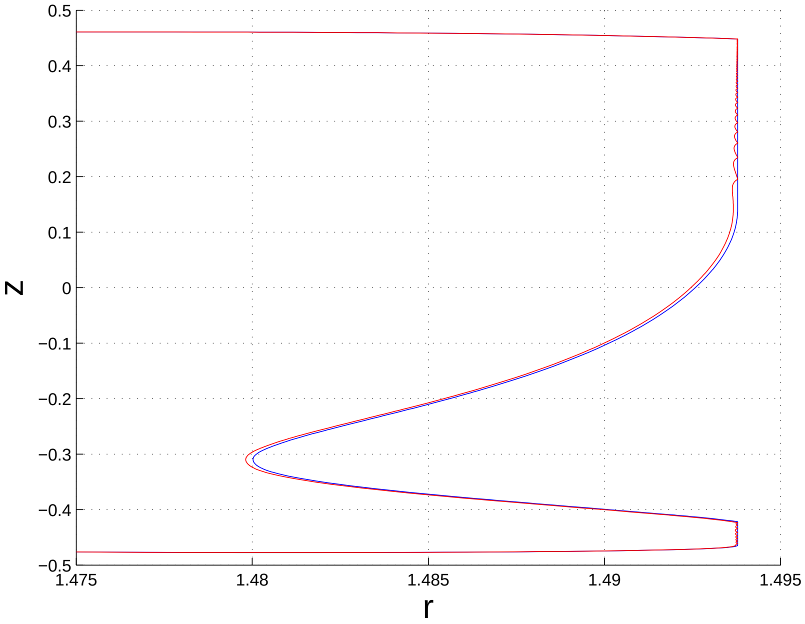

Figure 5.4: Projections of a representative trajectory into the $r-z-$plane, derived with the FER-model (red) and the PER-model (blue). Calculations are done in a liquid bridge of $\Gamma = 0.66$, $\mathrm{Re} = 1800$, $\mathrm{Pr} = 4$, $\mathrm{Gr} = \mathrm{Bi} = 0$ with a density-matched ($\varrho = 1$) particle of $\mathrm{St} = 10^{-4}$.

5.2.4 Interpolation

For the integration of the equations of motion the ODE-solver firstly needs the velocity components and secondly all components of the velocity gradient (Jacobian) for any arbitrary point in the liquid bridge. These data can only be obtained by interpolation and the adequate built-in function for this task is MATLAB's 3D-interpolation routine `interp3` providing linear and spline interpolation. The choice of the interpolation strategy is a compromise between accuracy and computing time.

The fastest method is the linear interpolation which can be performed locally, i.e. only the values of the immediate grid neighbours are needed. This is high efficient but one has still to carry out an additional procedure for the evaluation of the Jacobian. The best results for the velocity components are found by a global spline interpolation, where the data of the entire flow is taken into account. The global spline interpolation yields good

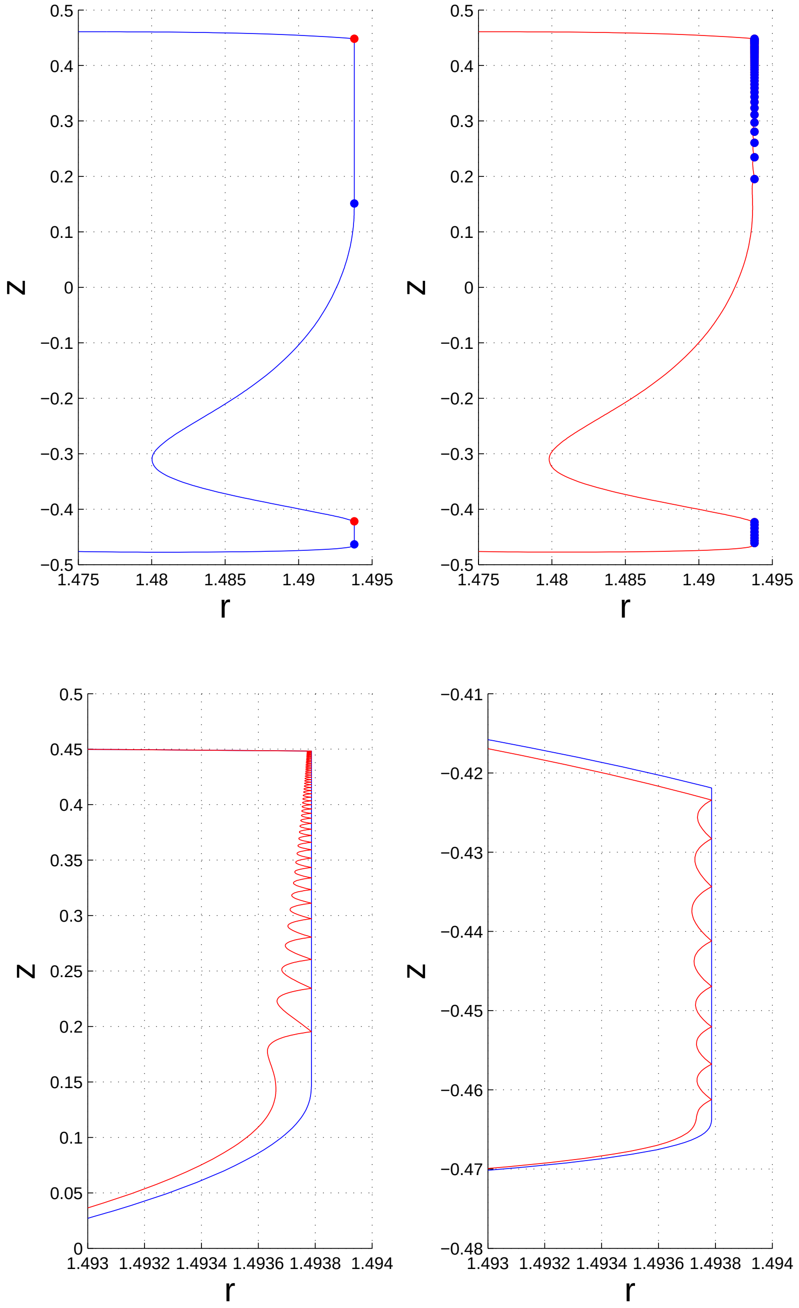

Figure 5.5: Upper images: Projections of a representative trajectory into the $r-z-$plane, calculated with the PER-model (left) and the FER-model (right). Red dots indicate collision points of the particle with the liquid free surface and blue dots indicate surface release points. Lower images: Close-up of the upper and lower particle–liquid free surface interaction regions. Blue trajectory is determined within the PER-model and red one within the FER-model.

results but is enormously time consuming. The (local) linear interpolation for all velocity components is approximately 50-times faster than the global spline interpolation.

A reduction of the numerical effort can be achieved by a reduction of the grid that is taken into account for the interpolation corresponding to a **local interpolation**. In case of a spline interpolation, the reduced grid results in a reduced number of interpolation points, hence the spline of a local interpolation will in general not agree to the spline of the more accurate global interpolation. To shield the interpolation result from the tendency to overshoot, the spline interpolation is replaced by a Hermite spline interpolation and the final implemented interpolation procedure is a combination of a (linear) pre-interpolation with `interp3` followed by a local piecewise cubic hermite spline interpolation with `pchip`. Another advantage of `pchip` is the high efficient evaluation of the Jacobian by the usage of the underlying analytical interpolation function. The interpolation procedure consists of three steps: grid trimming, pre-interpolation and local Hermite interpolation, all discussed in detail below.

Grid trimming

To reduce the numerical effort, the interpolation procedure doesn't take the entire flow field data into account. The intention is to find a reduced grid segment that represents the flow locally. Due to the staggered grid, this reduced grid is to carry out for every field variable separately. Since the interpolation point is far from any (quasi)-boundaries, which are

- **radial:** $r = 0$ and $r = R^\dagger$
- **azimuthal:** $\varphi = 0/2\pi$
- **vertical:** $z = \pm z^\dagger$,

the reduced grid is found quite simply by taking the two immediate grid neighbours on every side in each spatial direction. The final segment is then of size $4 \times 4 \times 4$ grid points plus the single point $\boldsymbol{y}$ for the interpolation, representing the current particle position. A one-dimensional illustration of the grid point arrangement of the reduced grid is

$$[\quad x_{\text{pos-1}} \quad , \quad x_{\text{pos}} \quad , \quad y_i \quad , \quad x_{\text{pos+1}} \quad , \quad x_{\text{pos+2}} \quad] \tag{5.3}$$

with the intermediate point y_i and his two grid neighbours on every side. The grid point x_{pos} is defined as the first point on the respective grid axis, which is smaller, or in case of the vertical axis larger, than y_i. In case the particle and the interpolation point $\boldsymbol{y}$ respectively is close to any (quasi)-boundary the trimming procedure is slightly adapted.

A simple linear interpolation requires only one neighbouring grid point on each side in every direction, but a higher accuracy interpolation like the followed Hermite interpolation requires at least more than only one grid neighbour.

Even if the reduced segment represents a cylinder segment it is effectively treated as a cuboid. Figure 5.6 illustrates a reduced grid segment. All thin black lines represent the grid boundaries where the field variables are given on selected points. Due to the staggered grid method these points are not simply the grid boundary intersection points. The red circle represents the particle position $\boldsymbol{y}$ where the velocity field has to be evaluated. All green lines are the boundaries of the cross sectional planes, discussed in more detail below.

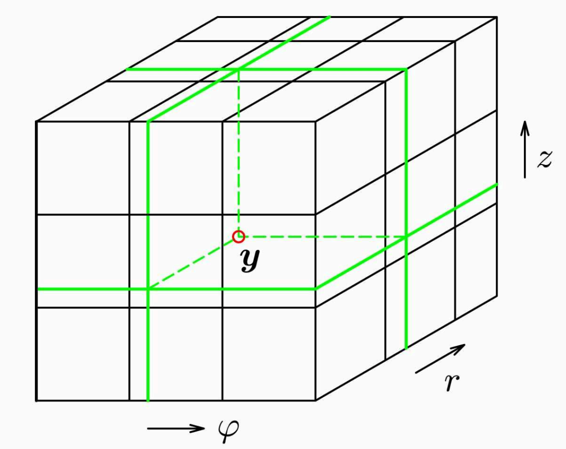

Figure 5.6: Reduced grid segment with interpolation point $\boldsymbol{y}$.

Pre-interpolation

Once the point is located and the grid is trimmed for every field variable one can think of three distinguished planes, which are the cross sectional planes through $\boldsymbol{y}$ as shown in figure 5.7 (indicated in green in figure 5.6).

In general not a single value of any field variable is known on the cross sectional planes through $\boldsymbol{y}$. In the next step all surrounding grid points of the cube (fig. 5.6) are projected on these planes. The subsequent allocation of these projected grid points with field variables is then called pre-interpolation and is done with MATLAB's 3D-interpolation routine `interp3`. Up to this point the field variables of $\boldsymbol{y}$ are still unknown but all grid points on the cross sectional planes are allocated with interpolated data. These allo-

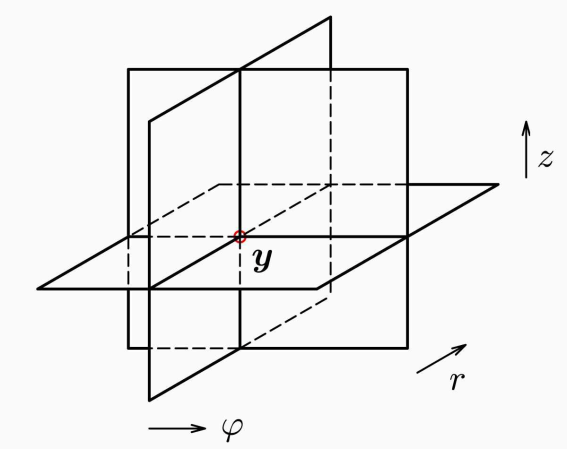

Figure 5.7: Cross sectional planes of the reduced grid with interpolation point $\boldsymbol{y}$.

cated grid points represent the basis for the final one-dimensional piecewise Hermite cubic spline interpolations (`pchip`) which is done once for every cross sectional plane. With the three interpolants (one for every plane) the velocities and all first spatial derivatives (with MATLAB's built-in function `fnder`) at $\boldsymbol{y}$ are evaluated.

Hermite interpolation

Compared to the ordinary polynomial spline, which guarantees continuity of first and second derivative at all grid points, a piecewise Hermite spline works without continuity of the second derivate. By relaxing the condition of continuity of the second derivative a degree of freedom is generated, which is then used to construct an interpolation function which is monotonous. The resulting interpolant shows no short-wavelength oscillations or overshoots.

6 Theory

Before the numerical results are discussed, a recapitulation of the previous chapters gives an overview on the system one is dealing with and acknowledges the approximations made.

6.1 Size of the system

The particle motion in the liquid bridge is modelled in form of a system of three coupled non-linear ordinary differential equations of second order. The ingredients for this ODE-system are on the one hand some dimensionless parameters defining flow and particle and on the other hand the initial conditions of the particle.

The parameter space of the flow was identified as five-dimensional, spanned by the aspect ratio Γ, Re, Pr, Gr and Bi numbers. In case of zero gravity and adiabatic boundary condition for the liquid free surface, the Grashof and Biot numbers vanish and the parameter space is reduced to an effective three-dimensional one.
The parameter space of the particle is three-dimensional, spanned by the density ratio ϱ, St and Fr numbers. Furthermore, zero gravity means that the Froude number does not play any role as well.
Hence, the dimension of the parameter space of the flow-particle-system is 8 or 5 in case of zero gravity and adiabatic boundary conditions.

In addition, all possible initial states of the particle are in general represented by the six-dimensional phase space, whereas flow–particle velocity-matching at the initial particle position reduces the initial phase space to an effective three-dimensional one, corresponding to the position space which is again represented by the geometry of the liquid bridge with its finite volume.

With all the mentioned simplifications, zero gravity, adiabatic boundary conditions and initial flow–particle velocity-matching, one deals for the initial conditions with a five-dimensional parameter space coupled to the three-dimensional finite size phase space of the particles initial state.

6.2 Assumptions of the model

Below one finds a summary of all approximations made, which are either of numerical or systematic nature.

- **Flow: Oberbeck–Boussinesq approximation**
  - Neglect the free surface deformation
  - Consideration of small temperature variations only
  - Use of Newton's heat transfer law
- **Flow: Numerics**
  - Discretization errors, mainly caused by aliasing (error due to truncation of Fourier-series) and the subsequent flow field filtering procedure
  - Flow field interpolation
- **Particle: Maxey–Riley equation**
  - Consideration of perfect spherical particles
  - Neglect finite size particle effects
  - Neglect terms in the equation of Maxey & Riley (e.g. Faxén corrections)
  - Particles are monodisperse, i.e. of same Stokes number
  - Numerical errors, especially of the ODE-solver
- **Particle: Interactions**
  - Consideration of one-way coupling only
  - Use of simple particle–boundary interaction model
  - Neglect particle–particle interactions

In addition, the non-linearity of the ODE-system indicates chaotic behaviour. Some regions of the liquid bridge are in fact very sensitive on small deviations of the particles initial state or on variations of any model variable. Even the choice of the computers operating system leads for selected trajectories to different results.

On the other hand PAS turns out to be an extremely robust phenomenon. Chapter 11 will show PAS formation even for ideal passive tracers by using the FER-model as particle–boundary interaction model.

7 Subcritical analysis: Re $= 1000$

The subcritical case is of special interest for the present work, because the basic ideas on the PAS-mechanism are formed here. In a next step these ideas will be transferred to the supercritical flow. Additionally this section is used for the introduction of some recurring visualization strategies.

The present chapter will focus onto the zero gravity flow

$$\mathrm{Pr} = 4 \quad , \quad \Gamma = 0.66 \quad , \quad \mathrm{Gr} = 0 \quad , \quad \mathrm{Bi} = 0\,. \tag{7.1}$$

With the given parameters one can estimate the critical Reynolds number from figure 7.1 as $\mathrm{Re_c} \approx 1080$, whereas the slightly subcritical value $\mathrm{Re} = 1000$ is chosen for the present investigation.

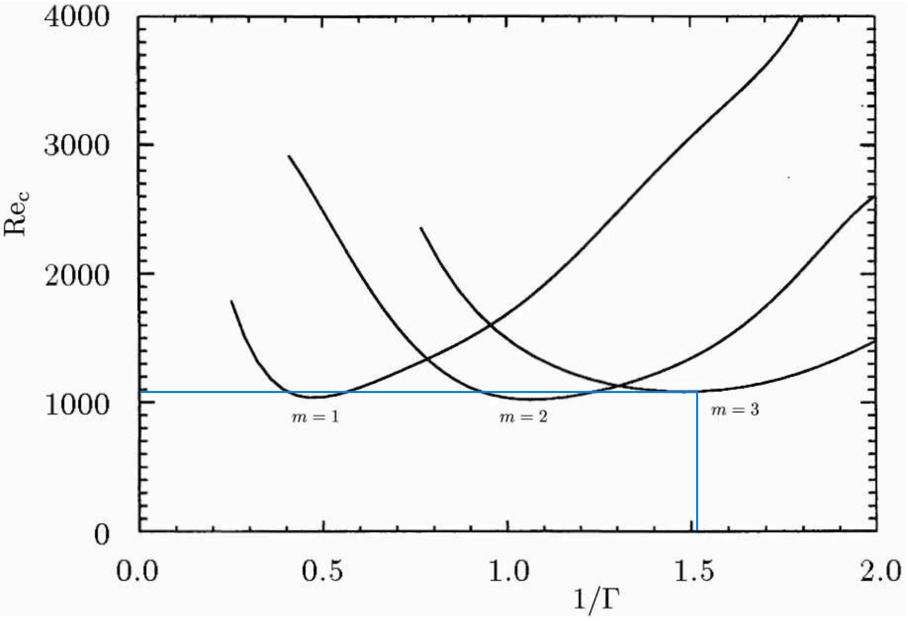

Figure 7.1: Neutral curves of the thermocapillary flow in a liquid bridge for $\mathrm{Pr} = 4$, $\mathrm{Gr} = 0$ and $\mathrm{Bi} = 0$. Taken from Kuhlmann [21].

7.1 Simulation with Poseidon

The grid resolution is chosen as $N_r \times N_z \times N_\varphi = 50 \times 40 \times 14$. For a higher resolution of the boundary layers, the grid is not uniformly spaced and subject to a geometric grid compression in radial and axial direction. The compression factors are $f_r = 0.96$ in radial and $f_z = -0.93$ in axial direction with reference points $z = 0$ and $r = R = 1.515$. The azimuthal division is homogeneous.

The simulation reached the stable 2D-state within a dimensionless time period of $t = 2$, i.e. within two time units of the momentum diffusion time.

Figure 8.3 shows velocity and temperature fields in an arbitrary vertical cross section (top image) and a representative horizontal cross section at $z = 0$ (bottom image) of the liquid bridge. The absence of any azimuthal velocity component in the horizontal cross section illustrates the clear two-dimensional flow structure. In addition the vertical cross section demonstrates the toroidal vortex nature.
The white areas around the cylinder axis and around the outer radial boundary, which is the liquid free surface, indicate regions without data. This is due to the staggered grid, which does not provide temperature T and axial velocity u_z at the radial boundaries. The outermost radial coordinate, where the velocity field is known completely, corresponds to the radial coordinate of the outermost cell-center $r_{\text{out}} = r_{\text{center}}(N_r)$ (see appendix C.2). The distance between r_{out} and the liquid free surface at $r = R$ defines a narrow dataless gap $\delta = R - r_{\text{out}}$ which implies a minimum particle size and a minimum Stokes number St_{min} respectively, deduced from

$$\text{St} = \frac{2a^2}{9d^2} \qquad \Longrightarrow \qquad \text{St}_{\text{min}} = \frac{2}{9}\delta^2 \,. \tag{7.2}$$

For the present liquid bridge one finds $\delta = R - r_{\text{out}} = 1.5150 - 1.5103 = 4.7 \cdot 10^{-3}$, which corresponds to $\text{St}_{\text{min}} \approx 5 \cdot 10^{-6}$. Due to numerical reasons a practicable minimum particle size lies slightly above the theoretical minimum value.

For demonstration purposes only, a size corresponding to $\text{St} = 5 \cdot 10^{-5}$ is chosen for now. From this Stokes number one can easily follow the contact radius $R^\dagger = 1.5$.

A liquid bridge of radius $R = 3$ mm, like it was used in Schwabe et al. [2], and a particle size equivalent to $\text{St} = 5 \cdot 10^{-5}$ result in the dimensional particle radius

$$\Gamma = \frac{d}{R} = 0.66 \approx \frac{2}{3} \quad \longrightarrow \quad d \approx 2\,\text{mm} \quad \longrightarrow \quad a = d\sqrt{4.5\,\text{St}} \approx 30\,\mu\text{m}\,. \tag{7.3}$$

Hence the particle diameter $d_{\text{p}} \approx 60\,\mu\text{m}$ ranges in the upper region of the investigations of Schwabe et al. [2].

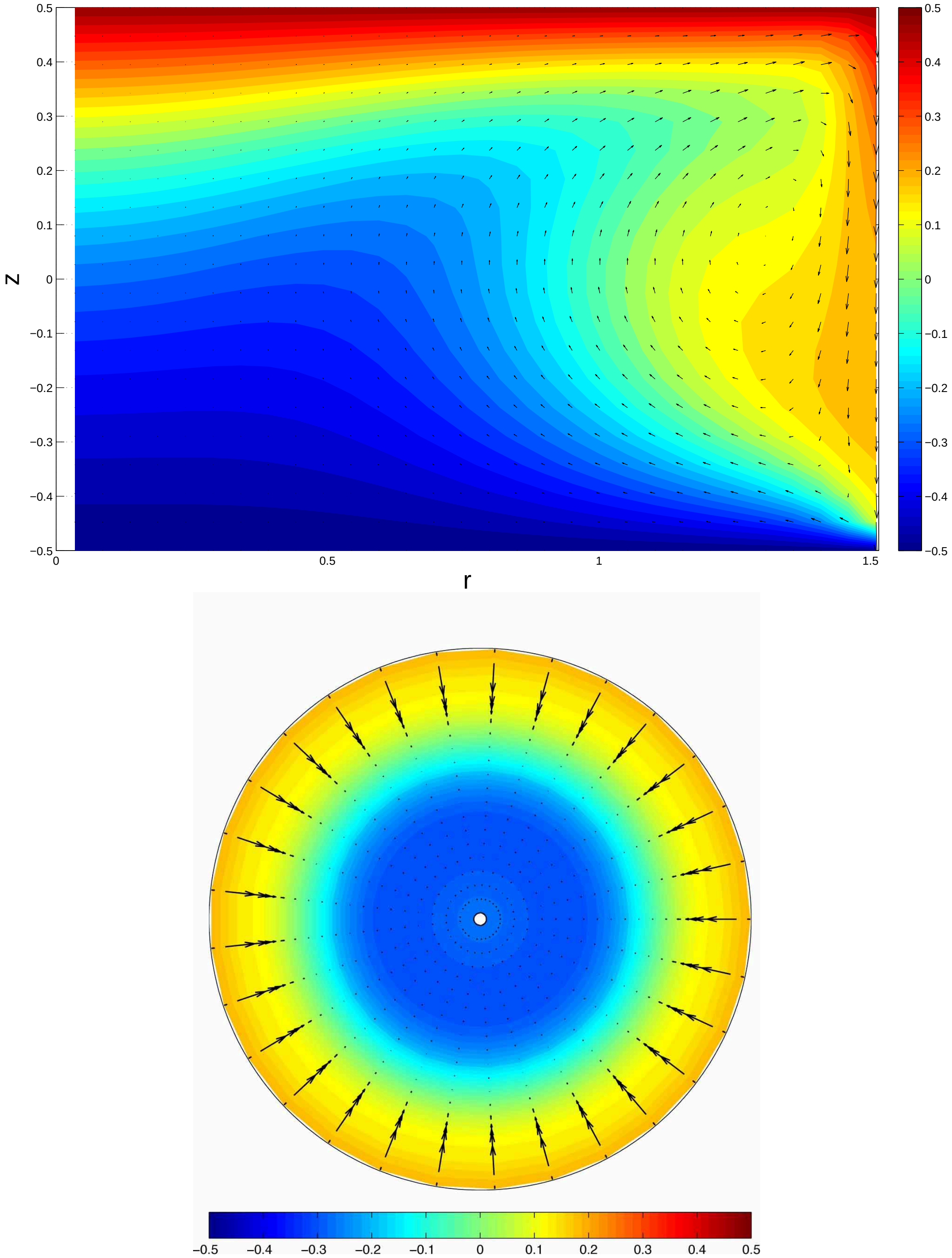

Figure 7.2: Vertical cross section (top) and horizontal cross section at $z = 0$ (bottom) of the liquid bridge to show representative temperature field and velocity field $\boldsymbol{u}(\boldsymbol{x})$.

7.2 PAS-mechanism

The following section will clarify the PAS-mechanism for the subcritical flow in a step by step manner.

Streamlines and pathlines

Another common method for the visualization of a flow field is the usage of streamlines instead of the velocity field. Streamlines $\boldsymbol{x}(s, t_0)$ are parameterized with the arc length s and are given for a certain time t_0 as curves tangent to the velocity field vectors. With a well-known flow field $\boldsymbol{u}(\boldsymbol{x}, t_0)$, a streamline is determined by fulfilling the equation

$$\frac{\mathrm{d}}{\mathrm{d}s}\,\boldsymbol{x}(s, t_0) = \frac{\boldsymbol{u}(\boldsymbol{x}, t_0)}{|\boldsymbol{u}(\boldsymbol{x}, t_0)|}\,. \tag{7.4}$$

In a general unsteady flow, streamlines are to distinguish from pathlines, which are simply trajectories of individual fluid elements. From a given flow field $\boldsymbol{u}(\boldsymbol{x}, t)$ a single pathline $\boldsymbol{x}(t)$ is determined by

$$\frac{\mathrm{d}}{\mathrm{d}t}\,\boldsymbol{x}(t) = \boldsymbol{u}(\boldsymbol{x}, t)\,. \tag{7.5}$$

Pathlines can be interpreted as trajectories of massless point particles. In steady flows, streamlines and pathlines are identical.

Figure 7.3 shows the streamlines of the steady subcritical flow corresponding to the flow field given in the upper image of figure 7.2. Due to numerical reasons the presented streamlines are not exactly closed.

Equation of motion for the subcritical flow

The equation of motion for a small spherical particle is given by (4.35) and reduces for the subcritical flow ($\Omega = 0$) in zero gravity ($\mathrm{Fr} \to \infty$) to

$$\ddot{\boldsymbol{y}} = \frac{1}{\varrho + \frac{1}{2}}\left[-\frac{1}{\mathrm{St}}(\dot{\boldsymbol{y}} - \boldsymbol{u}) + \frac{3}{2}\,\boldsymbol{u}\cdot\nabla\boldsymbol{u}\right]\,. \tag{7.6}$$

Obviously the particle properties size ($\propto \mathrm{St}$) and inertia ($\propto \varrho$) are responsible for a deviation of the particle trajectory from the pathline. Below, these particle properties will get suppressed step by step for a clear assignment of the PAS-mechanism.

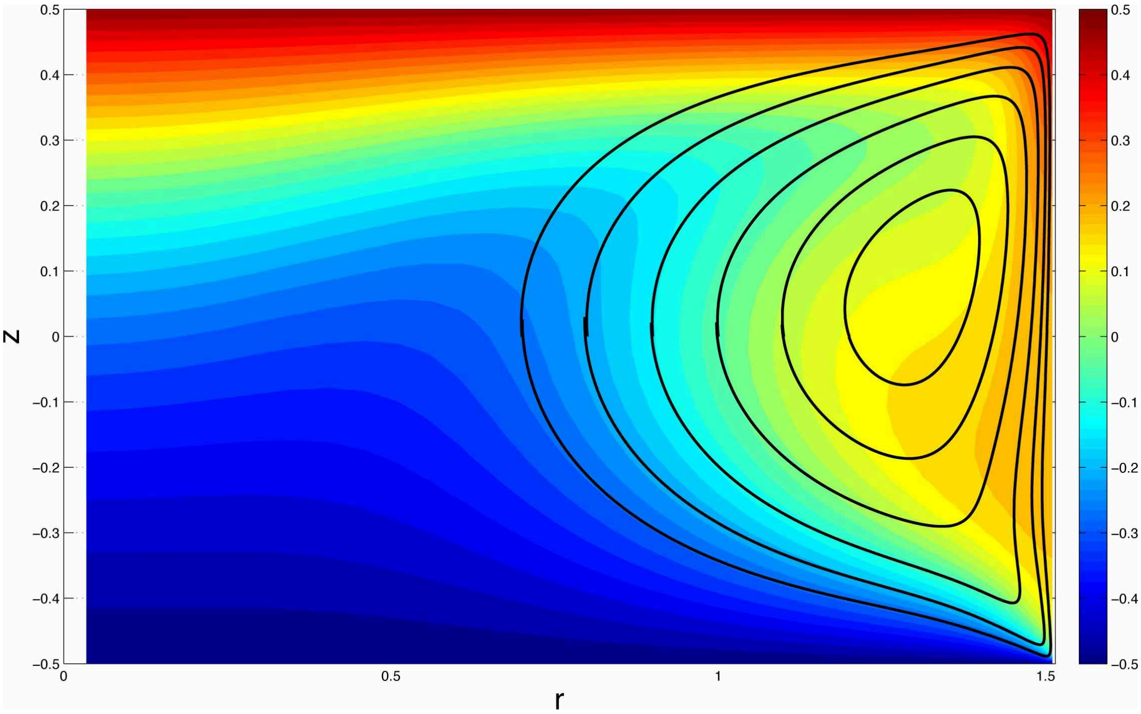

Figure 7.3: Streamlines of the subcritical flow in the vertical cross section.

Model of a density-matched tracer of infinitesimal size

The most easiest thinkable model is dealing with ideal passive particles - **density-matched** tracers of **infinitesimal size**. Firstly, density-matching means $\varrho = 1$ and reduces (7.6) to

$$\ddot{\boldsymbol{y}} = -\frac{2}{3\,\mathrm{St}}(\dot{\boldsymbol{y}} - \boldsymbol{u}) + \boldsymbol{u}\cdot\nabla\boldsymbol{u}\,. \tag{7.7}$$

Secondly, an infinitesimal size corresponds to a vanishing Stokes number ($\mathrm{St} \to 0$) which simplifies (7.7) again to

$$\ddot{\boldsymbol{y}} = \boldsymbol{u}\cdot\nabla\boldsymbol{u} \quad \Longrightarrow \quad \dot{\boldsymbol{y}} = \boldsymbol{u}\,. \tag{7.8}$$

In the limit of $\mathrm{St} \to 0$, the Stokes drag, which acts on the velocity mismatch of particle and fluid with the reciprocal value of St, balances particle velocity and local fluid velocity instantaneously. Thus the particle trajectories correspond exactly to the pathlines and in case of a steady flow to the streamlines. Hence uniformly distributed particles would follow the pathlines and streamlines respectively corresponding to their initial positions. Particle segregation would be then contradictory to continuity, hence PAS can't get realized and therefore this model is oversimplified and not the appropriate approach for the present problem. For that reason one has to take a step further.

Model of a density-matched tracer of quasi-finite size

Again, a density-matched tracer is considered, but now of **quasi-finite size**. The term quasi-finite size stands for a tracer of radius a according to a given Stokes number $\mathrm{St} \ll 1$ but it is assumed that this sufficiently small particle still follows the pathline in excellent approximation. This assumption corresponds to the negligence of the Stokes drag, even if the particle is of finite size, and the particle trajectory is still determined by (7.8). The additional attribute of a particle of quasi-finite size was already introduced in section 4.4. Hence, a spherical tracer of radius a is not able to follow pathlines lying between the contact radius $R^\dagger$ and the liquid free surface.

Figure 7.4 shows again the streamlines of figure 7.3 in a close up. The vertical red line indicates the contact radius $R^\dagger$ as the maximum reachable radial position for the particle's center of mass. One will easily notice three distinguished streamlines (blue and green) which are tangent to the contact radius. The corresponding tangent points are indicated as blue dots. These tangent points are simply found by searching after a vanishing radial velocity component at the contact radius $R^\dagger$.

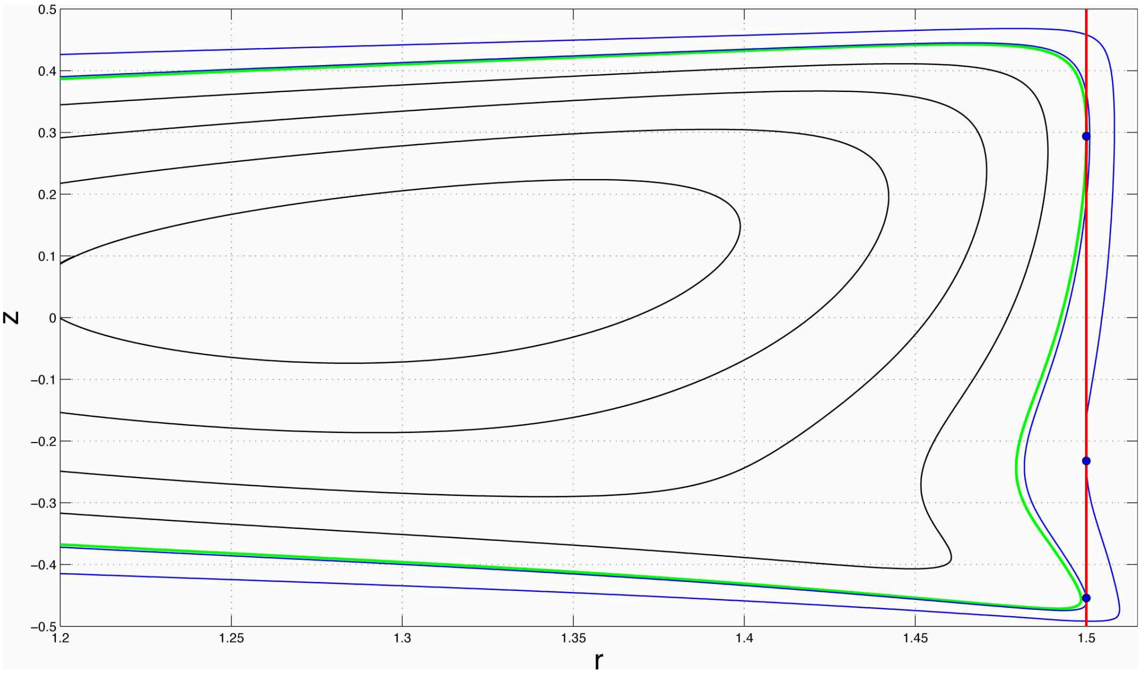

Figure 7.4: Close up of vertical cross section of subcritical flow with contact radius $R^\dagger$ (red), tangent streamlines plus tangent points (blue) and the PAS-streamline (green).

The tangent points of the vertical cross section appear on the unrolled cylinder surface of the contact radius as closed graphs, shown in the upper image of figure 7.5. These graphs are called from now on the **release lines**. The shortcuts for the release lines and tangent points respectively are from top to bottom $L_1 - L_3$. In case of the present subcritical 2D-flow, the release lines are simply circles, illustrated in figure 7.6. The most important streamline of the system, also referred to as **PAS-streamline**, corresponds in this case to the uppermost release line (L_1), green-coloured in figure 7.4. The streamline corresponding to the release line L_2 is of no relevance.

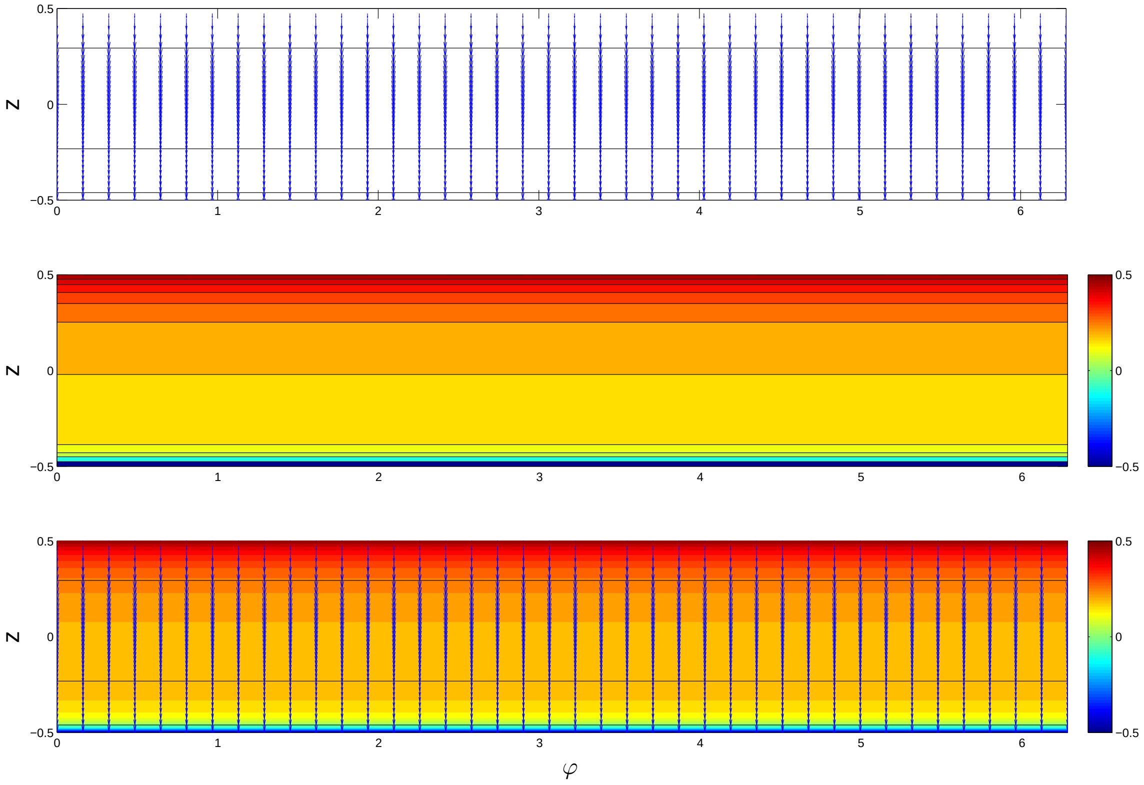

Figure 7.5: Unrolled cylinder surface at $R^\dagger$ showing velocity field $\boldsymbol{u}(\boldsymbol{x})$ and release lines $L_1 - L_3$ in the upper image, temperature field in the central image and altogether in the lowermost image.

The PAS-streamline is the result of the **finite-particle-radius effect**, the first and most important PAS-mechanism. For the explanation of the finite-particle-radius effect one has to make use of the PER-model, introduced in section 5.2.3. Basically one can distinguish between streamlines enclosed by the PAS-streamline and streamlines crossing the contact radius, whereas the PAS-streamline separates the enclosed streamlines from those crossing the contact radius.

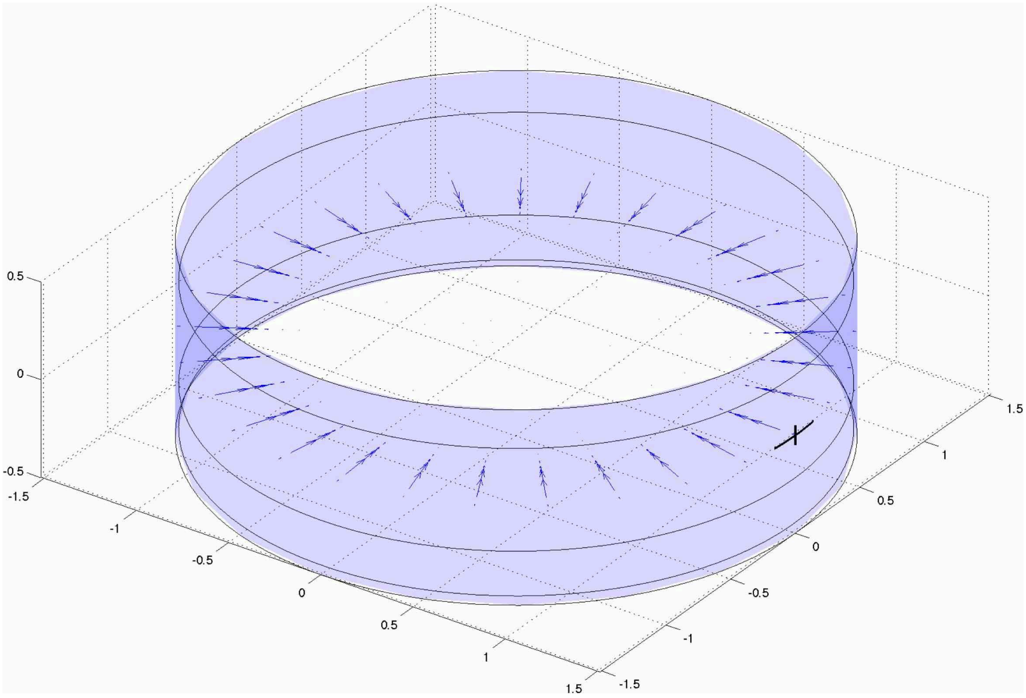

Figure 7.6: Bird's eye view of the liquid bridge with flow field $\boldsymbol{u}(\boldsymbol{x})$ at $z = 0$. The black marker at the surface indicates the point $\boldsymbol{x} = \{r = R, \varphi = 0, z = 0\}$ and serves for orientation only. The release lines $L_1 - L_3$ at $R^\dagger$ are shown as black circles.

All particles with an initial position **outside the PAS-streamline** will travel along their corresponding streamlines until they reach the liquid free surface and the contact radius respectively. The particle's center of mass will then slide along the contact radius as long as the radial velocity component of the flow faces outwards. The points at which the radial velocity component changes sign and turns inwards again, represent the **release points** for the particle. These points are firstly L_1, transferring the particle directly onto the PAS-streamline and secondly L_3, transferring the particle after another revolution onto the PAS-streamline.

All particles with an initial position inside the PAS-streamline will orbit on the corresponding (closed) streamline and are therefore not able to reach the liquid free surface. Due to that reason, all particles inside the PAS-streamline remain there and do not segregate.

Summarized, the finite-particle-radius effect is identified as the first PAS-mechanism, which brings all particles initially located outside the PAS-streamline onto the PAS-streamline. In the discussed model all particles initially located inside the PAS-streamline, also referred to as **core particles**, will remain on their corresponding streamlines forever.

From figure 7.7 one can clearly see the result of the finite particle radius effect, which has transferred the majority of all particles initially located outside the PAS-streamline onto the PAS-streamline within a time period of $t = 1$.

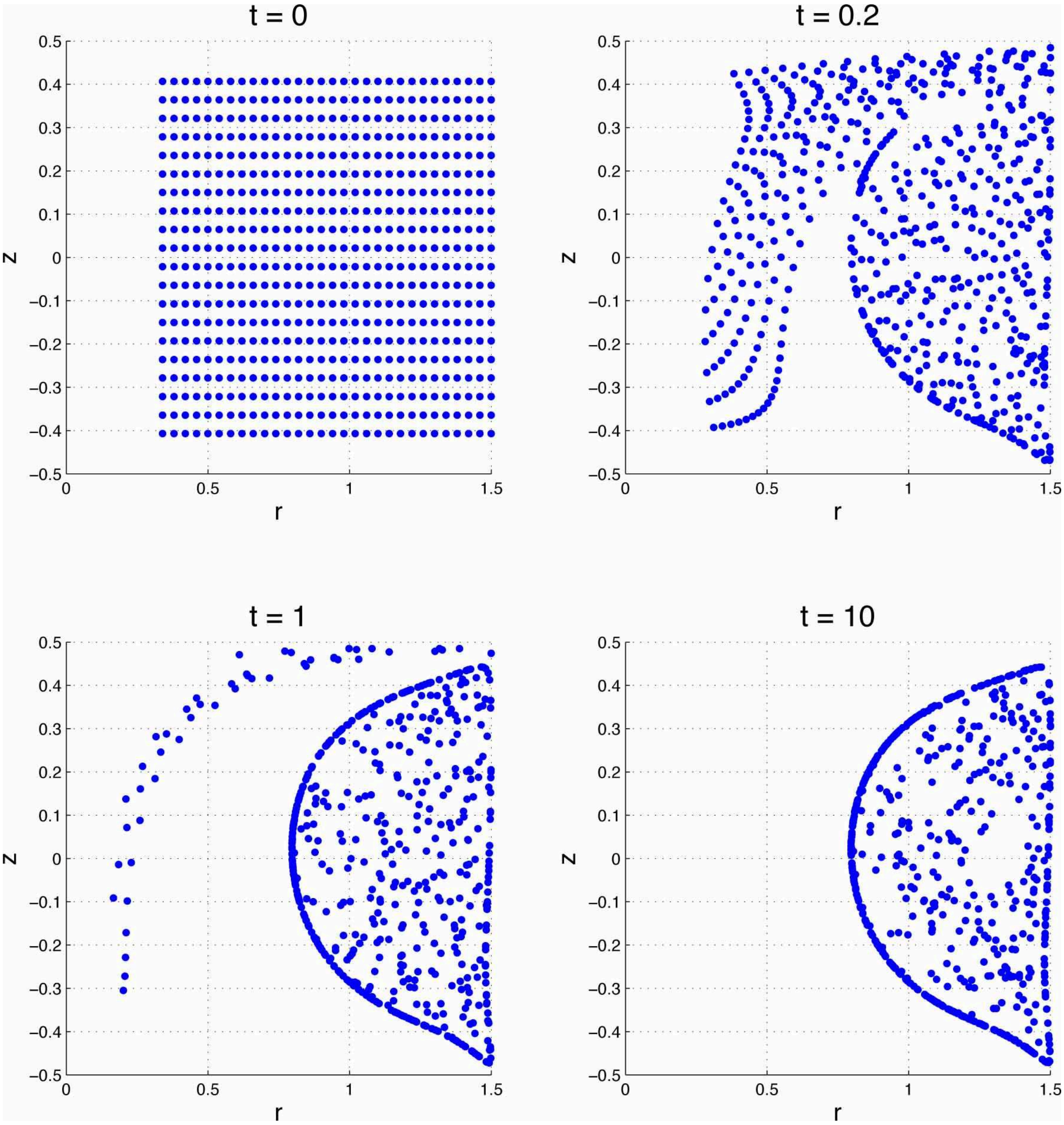

Figure 7.7: Particle distribution for density-matched tracers of quasi-finite size after $t = 0$, $t = 0.2$, $t = 1$, $t = 10$. Flow and particle parameters as introduced.

Model of a density-matched tracer of finite size

Within this model the particle size is taken fully into account, the trajectory is now determined by (7.7) and will deviate from the streamline due to the Stokes drag. For a considered particle size corresponding to $\mathrm{St} = \mathcal{O}(10^{-5})$ the effect of the Stokes drag is only very small and is of the order of the numerical uncertainties. For the mentioned particle sizes a clear statement regarding the action of the Stokes drag is therefore not possible.

Model of a general tracer of finite size

In the general case, within the present model, its dynamics is firstly determined by equation (7.6) and secondly by the finite-particle-radius effect. For particles of $\varrho > 1$ an effective centrifugal force can lead to another PAS-mechanism. If the effective centrifugal force is sufficiently larger all core particles will be continual transferred onto outer orbits until they collide with the surface and get transferred onto the PAS-streamline as well. This is called from now on the **centrifugal effect**.

In three dimensions the PAS-streamline of the vertical cross section is a toroidal surface. This means that all initially randomly distributed particles, which occupied the entire available phase space, are transferred to a subspace. Hence, the finite-particle-radius effect in combination with the centrifugal effect reduces the occupied phase space by one dimension.

For the subcritical and zero gravity case, the PAS-mechanism can be summarized to:

If a particle hits the liquid free surface anywhere, it will be transferred without fail onto the PAS-stream surface at least within one single revolution. In the end, all particles of $\varrho \geq 1$ will reach the surface due to the centrifugal effect.

8 Supercritical analysis: Re $= 1800$

The PAS-mechanisms seems to be clear for the subcritical case, as shown in the last chapter. Now it will be tried to apply the found mechanisms to a three-dimensional supercritical flow. At the same time PAS is no longer a two-dimensional surface but appears in the supercritical flow as a one-dimensional string.

8.1 Simulation parameters

Flow parameters

This section considers the same parameters as before, merely the Reynolds number is increased, i.e.

$$\mathrm{Pr} = 4 \quad , \quad \Gamma = 0.66 \quad , \quad \mathrm{Re} = 1800 \quad , \quad \mathrm{Gr} = 0 \quad , \quad \mathrm{Bi} = 0\,. \tag{8.1}$$

For these parameters, the fundamental wave number of the HTW is $m = 3$ with angular velocity $\Omega = -10.145$.

The grid resolution is $N_r \times N_z \times N_\varphi = 50 \times 40 \times 22$. It is stretched as in the subcritical case, with radial/vertical compression factors $f_r = 0.96/f_z = -0.93$ and corresponding reference points $z = 0$ and $r = R = 1.515$. The resulting dataless gap in this grid is again $\delta = 4.7 \cdot 10^{-3}$ with a theoretical minimum Stokes number of $\mathrm{St}_{\mathrm{min}} \approx 5 \cdot 10^{-6}$.

Particle parameters

The density-matched particles are moving in zero gravity and are chosen to be of same size as used in the subcritical flow. Hence the particle parameters are

$$\varrho = 1 \quad , \quad \mathrm{St} = 5 \cdot 10^{-5} \quad , \quad \mathrm{Fr} = \infty\,. \tag{8.2}$$

For the integration of the equations of motion (4.36) the following parameters are chosen: boundary interaction model is the PER-model in both cases, ODE-solvers tolerances are set to RelTol $= 10^{-4}$ and AbsTol $= 10^{-6}$ and the pre-interpolation method is chosen as linear. The flow field data is not used in the original form but Fourier filtered including the constant fraction ($n = 0$) and the first three harmonics of the HTW, i.e. $n = \{0, 3, 6, 9\}$.

Initial positions

As carried out for the subcritical case, the finite-particle-radius effect is assumed to be the major mechanism for PAS development. Therefore, one starts the investigation considering particles placed initially on the the contact radius $R^\dagger$, hence the initial position represents the first surface collision.

Trajectories of 360 particles are computed for the time period $t = [0, 6]$. All particles start velocity-matched at the contact radius $R^\dagger$, uniformly distributed on the unit circle. For the axial initial positions some height between the calculated release line L_1 and the upper disk is required. The choice of $z = 0.4$ guarantees an initial position above L_1 for every particle. Hence the initial positions are the one-dimensional set of points

$$\boldsymbol{Y}'_{\text{init}} = \{\boldsymbol{Y}' \in \mathbb{R}^6 \,|\, r' = R^\dagger \,,\, \varphi' = \frac{k\pi}{180} \,,\, z' = 0.4 \,,\, \dot{\boldsymbol{y}}' = \boldsymbol{u}'(\boldsymbol{x}')\} \quad , \quad k = 0, 1, \ldots, 359\,. \tag{8.3}$$

The integration time was chosen as $t = 6$, corresponding to $N_\Omega \approx 9.7$ HTW revolutions, determined by

$$N_\Omega = \frac{t}{\tau} \qquad \text{with} \qquad \tau = \frac{2\pi}{\Omega}\,. \tag{8.4}$$

8.2 Supercritical flow

8.2.1 Poseidon procedure

Starting from the state of rest and the thermal conduction state, hence $\boldsymbol{u} = 0$ and $T = z$, the simulation reached the unstable 2D–state within a dimensionless time period of $t = 1.5$. After imposing a perturbation of the temperature field [22]

$$\Delta T(r, \varphi, z) = A_T \frac{r}{R} \sin \frac{\pi(z + d/2)}{d} \sin\left(m\varphi + \varphi_0\right) \tag{8.5}$$

with perturbation amplitude A_T, azimuthal wave number of perturbation m and azimuthal phase of perturbation φ_0

$$A_T = 0.1 \qquad , \qquad m = 3 \qquad , \qquad \varphi_0 = 0 \tag{8.6}$$

an unstable standing wave emanates, well developed after another time period of $t = 2$.

In the last step the velocity field of this standing wave is again perturbed with a perturbation for every velocity component [22]

$$\Delta u_i(r, \varphi, z) = A_i \frac{r}{R} \sin \frac{\pi(z + d/2)}{d} \sin(m\varphi + \varphi_0) \qquad , \qquad i = r, \varphi, z \tag{8.7}$$

all with $m = 3$, $\varphi_0 = 0$ and perturbation amplitudes

$$A_r = -10 \qquad , \qquad A_\varphi = 6 \qquad , \qquad A_z = 3\,. \tag{8.8}$$

Both perturbations (8.5 - 8.7) can be simply imposed by defining A_i, m and φ_0 in Poseidon's input file.

The simulation is truncated if the Nusselt numbers have converged sufficiently to their constant values, hence if the weighted amplitudes of all Nusselt numbers are below 0.01%. Figure 8.1 shows the temporal development of all three Nusselt numbers and their tendency to converge if the simulation reaches the pure travelling wave solution.

At the end of simulation $t_0 = 8$, a well formed travelling wave solution is found, where $t = 0$ stands for the velocity perturbation onset.

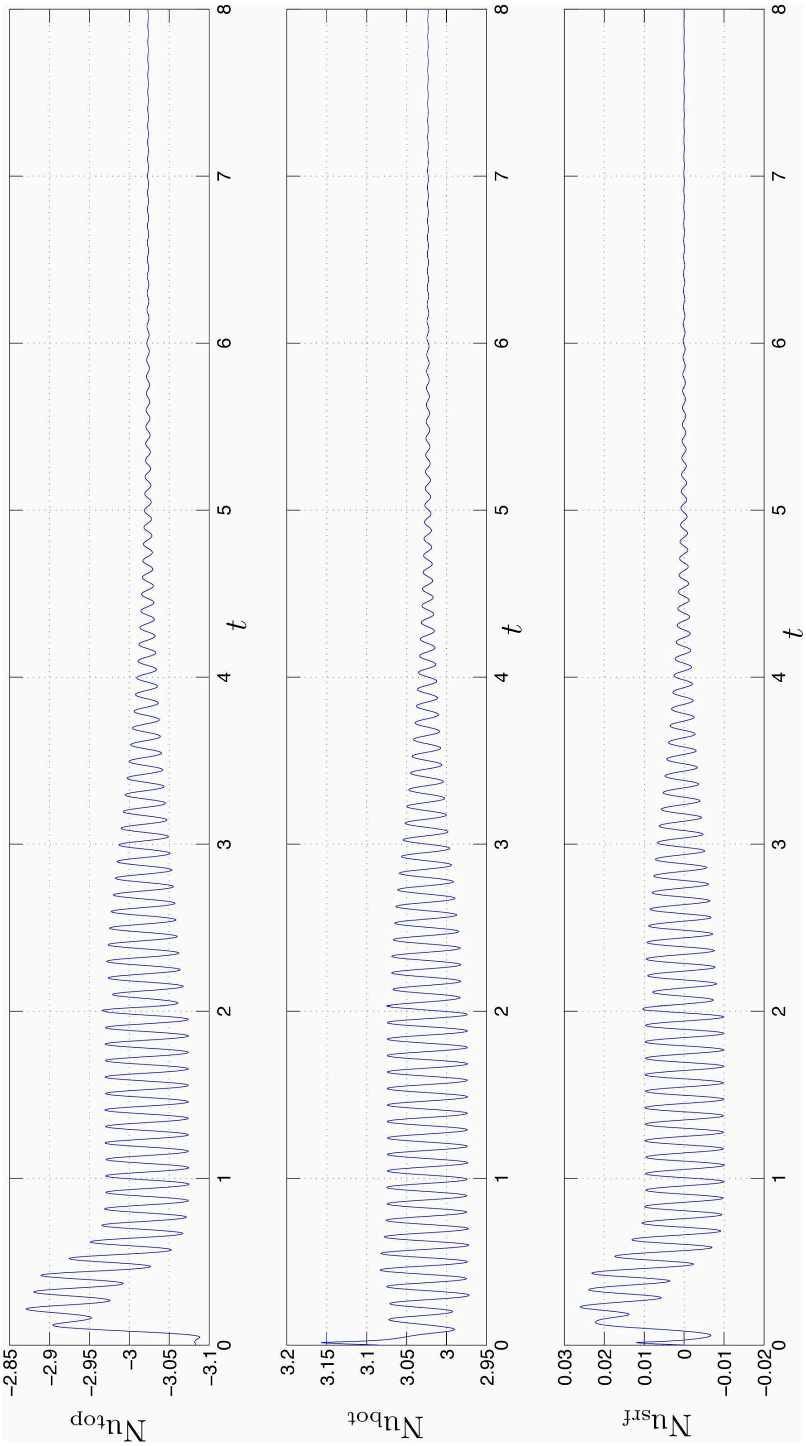

Figure 8.1: Temporal development of Nusselt numbers: uppermost image $\mathrm{Nu}_{\mathrm{top}}$ for top disk, central image $\mathrm{Nu}_{\mathrm{bot}}$ for bottom disk and lowermost image $\mathrm{Nu}_{\mathrm{srf}}$ for the liquid free surface. At $t = 0$ the perturbation of the temperature field (8.5) is imposed and at $t = 2$ the perturbation of the velocity field (8.7).

8.2.2 Solution

Representative temperature and velocity fields are shown in figure 8.3. Even if the flow is three-dimensional, the vertical cross section is qualitatively the same as in the subcritical case and shows in principle a basic flow. The horizontal cross section shows a flow field $\boldsymbol{u}(\boldsymbol{x}, t_0)$ which rotates like a rigid body in the indicated direction. The flow of figure 8.4 corresponds to $\boldsymbol{u}'(\boldsymbol{x}')$, i.e. the flow is observed from the rotating frame of reference. The release lines $L_1 - L_3$ are shown as well. They are no longer simple circles as for the subcritical case. In figure 8.5 one can see the release lines on the unrolled cylindrical surface of the contact radius $R^{\dagger}$.

From figure 8.2 one can easily understand the definition of the azimuthal point of reference, i.e. $\varphi' = 0$. It is defined at the maximum surface temperature of the fundamental perturbation wave (here $m = 3$) in the mid-plane of the liquid bridge, i.e. at $z = 0$.

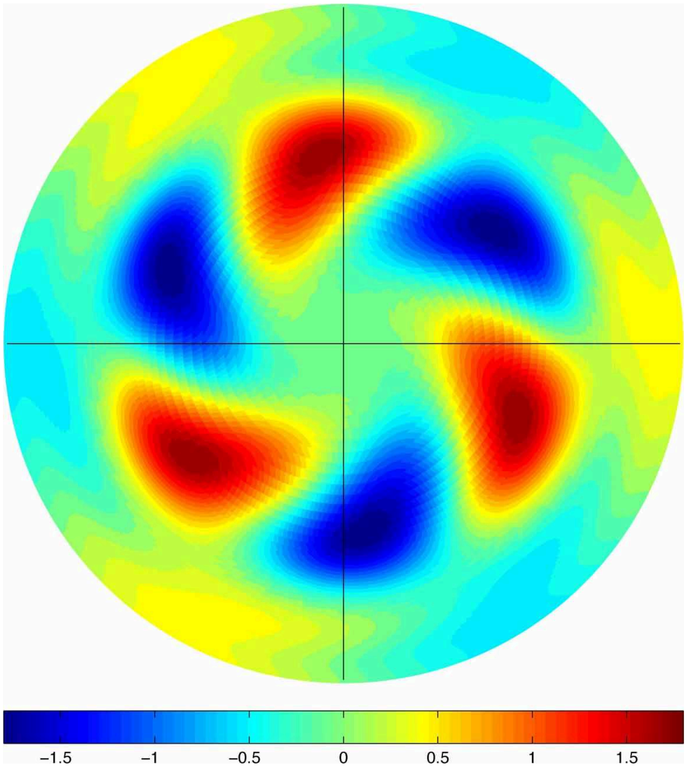

Figure 8.2: Temperature field $T(\boldsymbol{x}')$ of the fundamental perturbation wave $m = 3$ at $z = 0$.

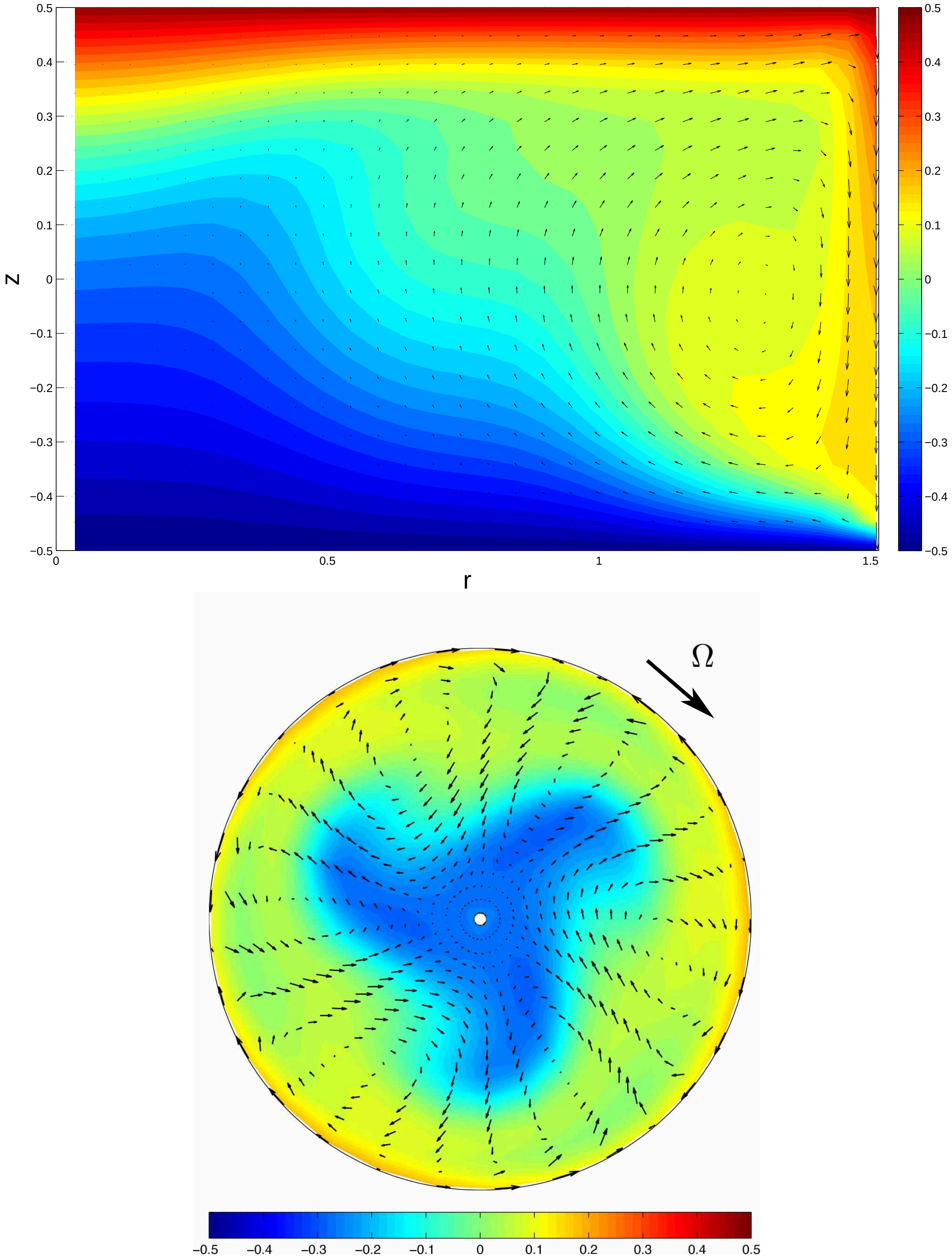

Figure 8.3: Vertical cross section (top) and horizontal cross section at $z = 0$ (bottom) of the liquid bridge to show representative (total) temperature field $T(\boldsymbol{x}, t_0)$ and velocity field $\boldsymbol{u}(\boldsymbol{x}, t_0)$. The arrow indicates the rotational direction of the flow ($\Omega = -10.145$).

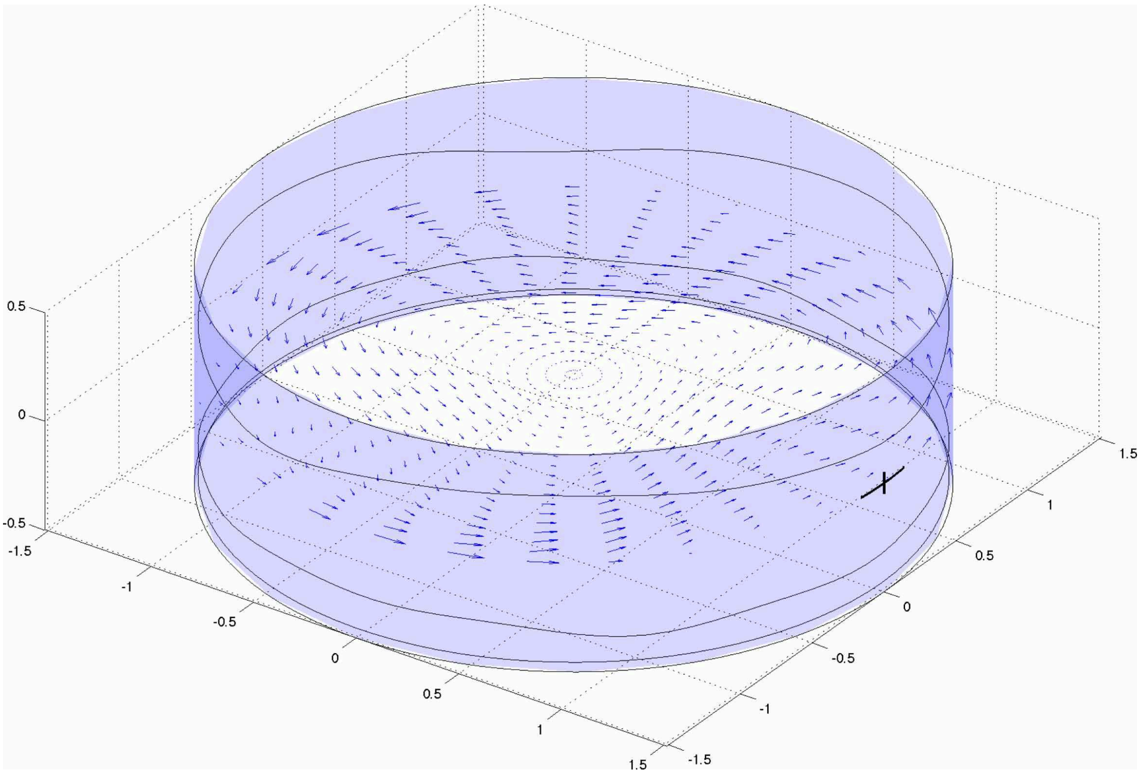

Figure 8.4: Bird's eye view of the liquid bridge with flow field $\boldsymbol{u}'(\boldsymbol{x}')$ (rotating frame of reference $\mathcal{K}'$) at $z = 0$. The black marker at the surface indicates the point $\boldsymbol{x}' = \{r' = R, \varphi' = 0, z' = 0\}$ and serves for orientation only. The release lines $L_1 - L_3$ at $R^\dagger$ are shown as black lines.

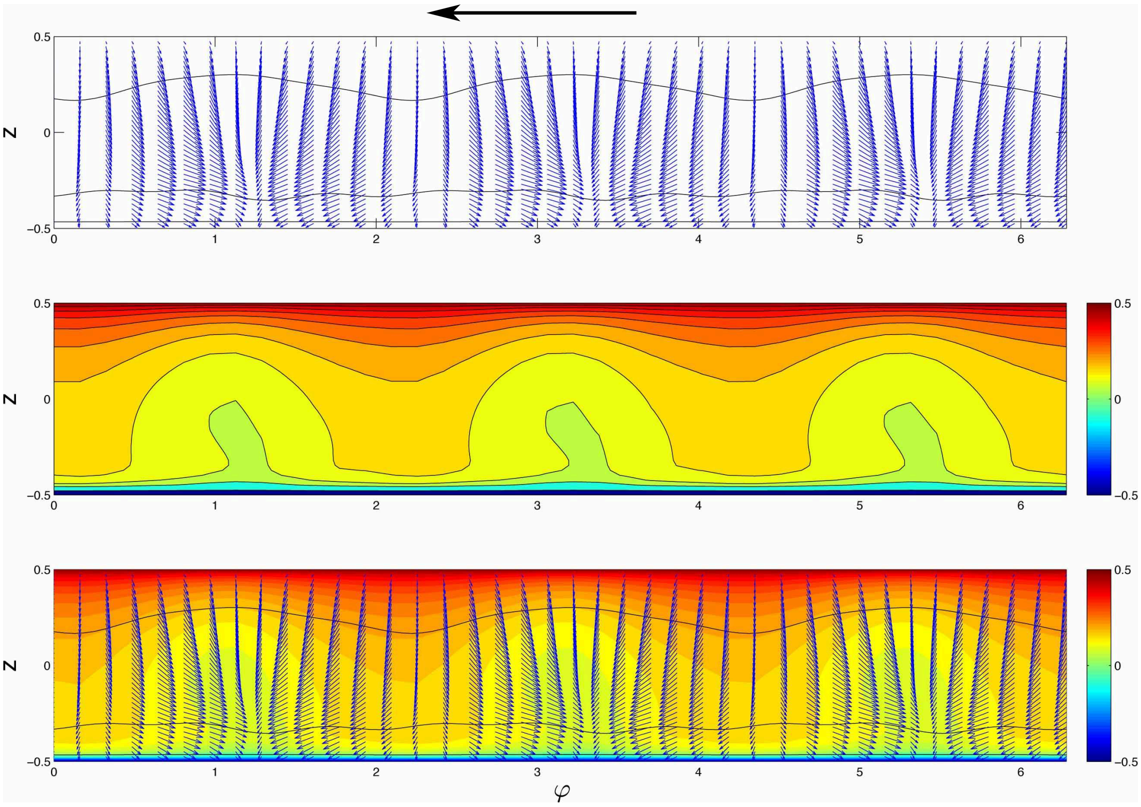

Figure 8.5: Unrolled cylinder surface at $R^{\dagger}$ showing velocity field $\boldsymbol{u}(\boldsymbol{x}, t_0)$ and release lines $L_1 - L_3$ in the uppermost image, temperature field $T(\boldsymbol{x}, t_0)$ in the central image and altogether in the lowermost image. The vertical velocity component u_z is scaled by 1/5 and the arrow indicates the travelling direction of the HTW.

8.3 PAS analysis

After the simulation period of $t = 6$, one finds the majority of all particles, i.e. 340 out of 360, in the primary SL-I-PAS, shown in figure 8.6. This agrees qualitatively excellent to experimental evidence, see Ueno et al. [5], Tanaka et al. [4] or Schwabe et al. [2] for instance.

The remaining 20 particles are in a noticeable regular structure, called from now on **secondary structure**, shown as blue trajectories in figure 8.7. Due to the doubled number of *wings*, i.e. number of windings around the mean primary vortex, one might tend to identify this structure as a SL-II-PAS on the first view.

Preliminary arguments against this speculation is firstly the documented shape of the SL-II-PAS by Tanaka et al. [4], from which the secondary structure deviates significantly and secondly the low Reynolds number ($\mathrm{Re} \approx 1.7\,\mathrm{Re_c}$) of the given simulation. Typical Reynolds numbers for the occurrence of SL-II-PAS are documented as $\mathrm{Re} \gtrsim 3\mathrm{Re_c}$. The secondary structure seems to be of different nature and is discussed in more detail below.

8.3.1 Classification of Trajectories

In the recent simulation, the hydrothermal wave is travelling clockwise[1] within the $\mathcal{K}-$frame with constant angular velocity $\Omega = -10.145$. In turn, **all** particles are travelling anticlockwise within the $\mathcal{K}'-$frame with an averaged angular velocity $\omega' = 2\pi/\tau'_\mathrm{p}$, where τ'_p is the length of period for a particle travelling around the $z-$axis within the rotating frame of reference $\mathcal{K}'$. The result for ω' vs. the particle's initial angles is shown in figure 8.8. The horizontal blue line in figure 8.8 shows the value of the hydrothermal wave's angular velocity Ω within the inertial frame of reference $\mathcal{K}$.

As it turns out, all SL-I-PAS forming particles are moving in good approximation with the same averaged angular velocity $\omega'_\mathrm{PAS} \approx 14.5 > \Omega$. The averaged angular velocity within the inertial frame of reference $\omega = \omega' + \Omega$ yields an anticlockwise net movement, wherefrom one can follow that PAS-particles run into the opposite direction as the HTW does. The experimental report onto this behaviour can be found in Ueno et al. [5].

In turn the rotational velocities of all particles forming the secondary structure deviate significantly from ω'_PAS and furthermore their angular velocities are slightly below the value of Ω, which results in a clockwise net movement within the $\mathcal{K}-$frame.

---

[1] The observation is always from above.

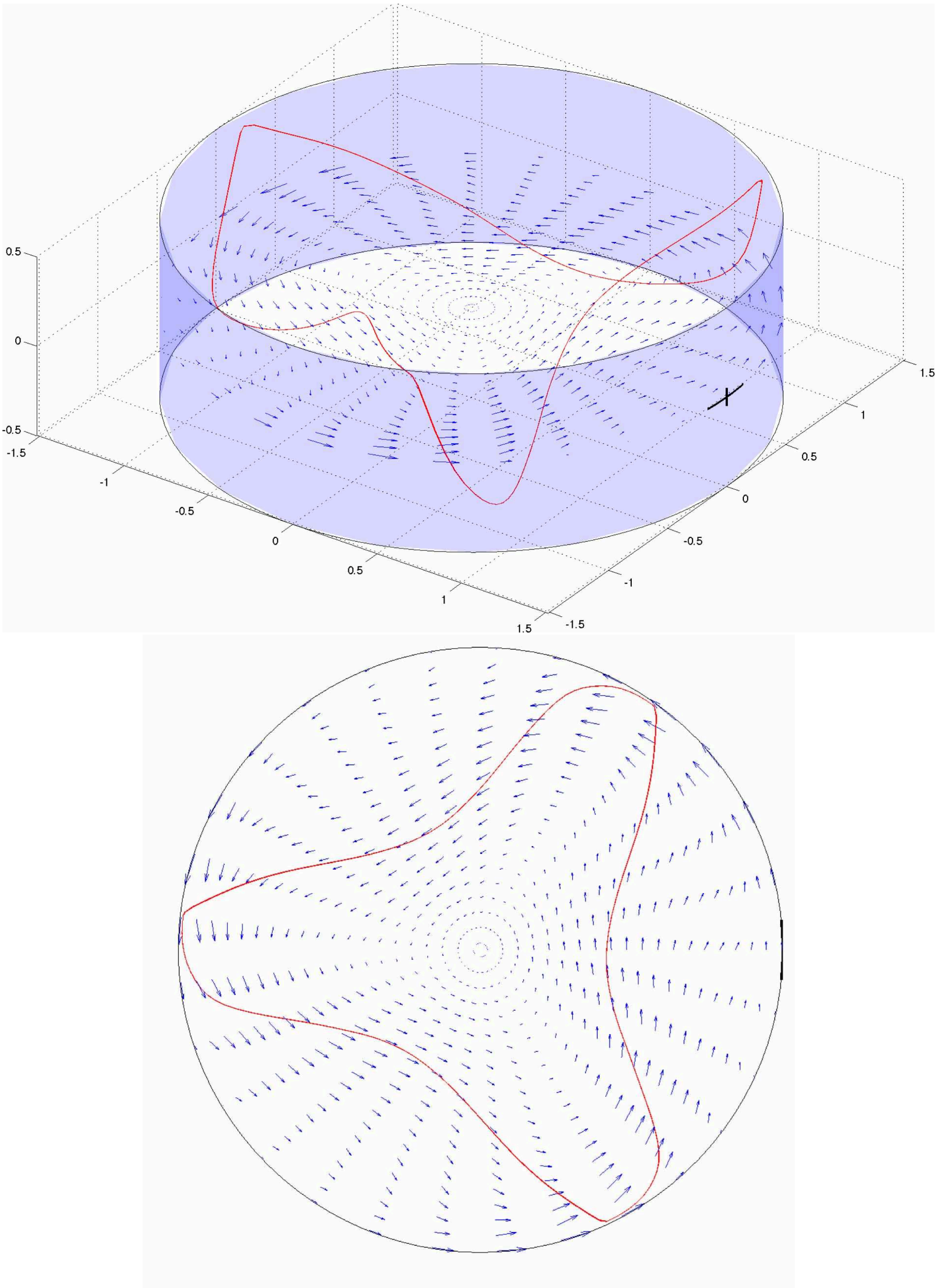

Figure 8.6: Selected particles forming a well developed SL-I-PAS from bird's eye view and from above in the $\mathcal{K}'$−frame for time period $t = [5, 6]$.

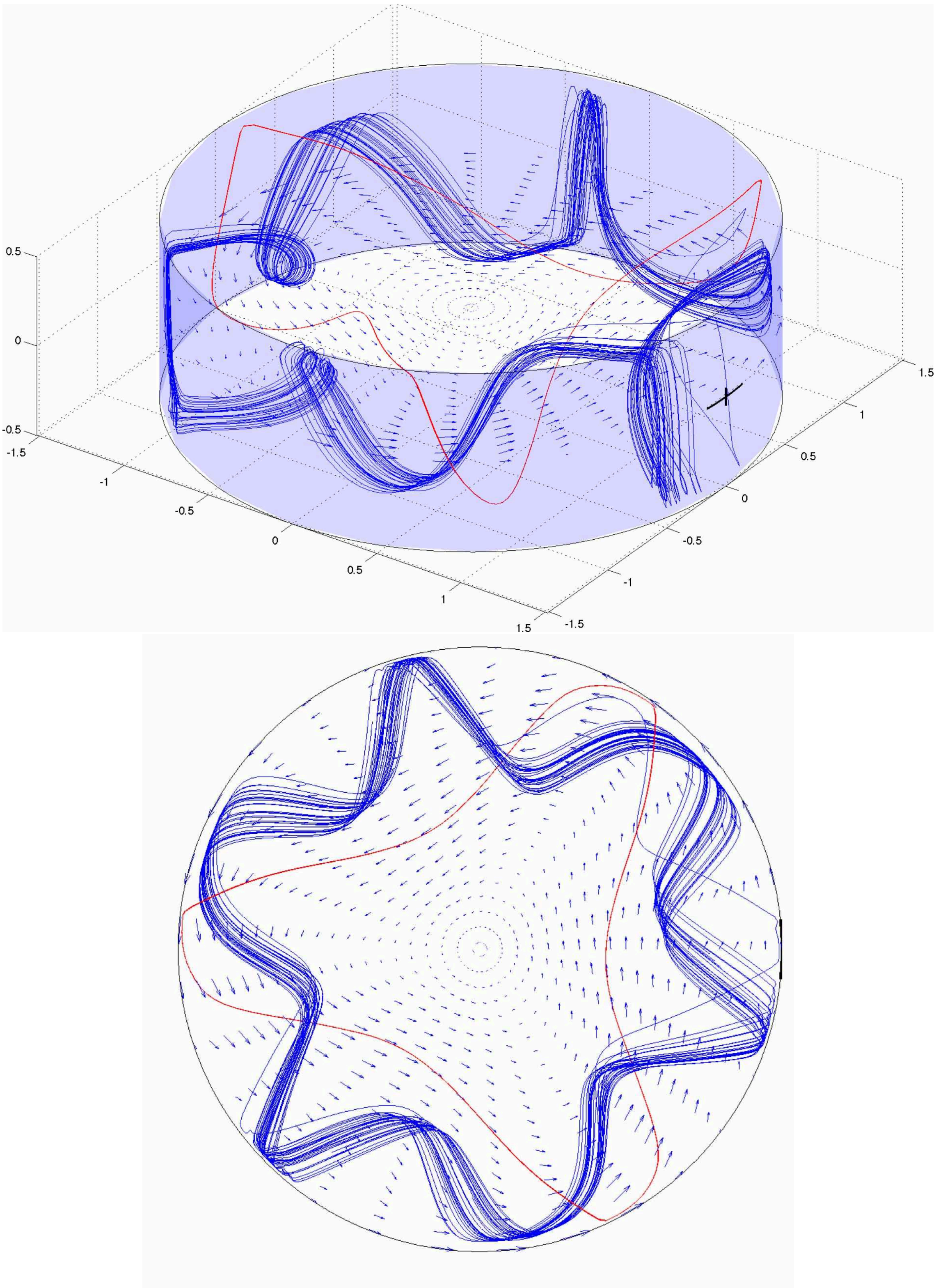

Figure 8.7: Beside the already introduced SL-I-PAS, some particles form a secondary structure from bird's eye view and from above $\mathcal{K}'$−frame for time period $t = [5, 6]$.

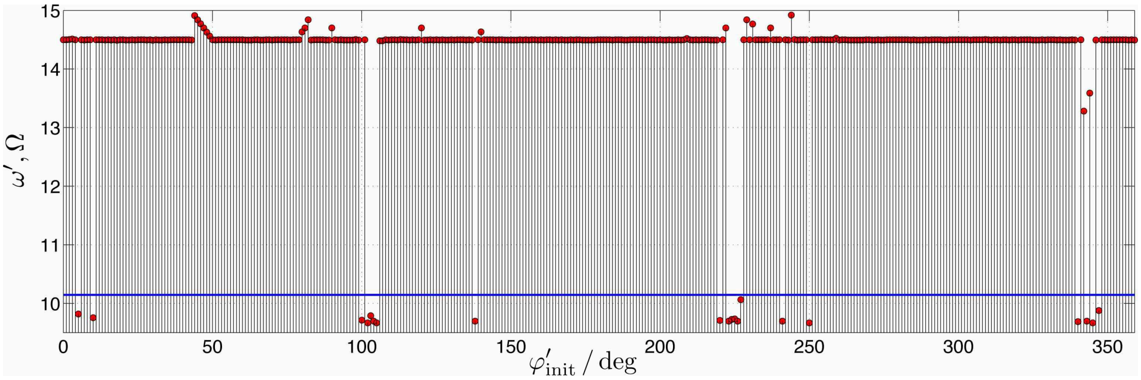

Figure 8.8: Averaged angular velocities ω' for all particles vs. their initial angles φ'_{init}. Value of the HTW's angular velocity Ω is shown as blue line.

Figure 8.9 shows the trajectory of a single PAS-particle ($\varphi'_{\text{init}} = 50°$) and figure 8.10 shows the trajectory of a secondary structure particle ($\varphi'_{\text{init}} = 100°$) observed from the rotating $\mathcal{K}'-$frame (upper images) and from the inertial $\mathcal{K}-$frame (lower images) for the time period $t = [4.76, 6]$ corresponding to 2 full HTW revolutions. The fields are plotted at $z = 0$ as they appear for the respective observer. The green dot indicates the particle's starting position, the red dot its final position and the blue dots indicate free surface collisions.

In figure 8.9 one can clearly notice the mentioned anticlockwise net movement in $\mathcal{K}$ and that the particle movement goes along with free surface interactions.

With the lower image of figure 8.10, showing a representative trajectory of the secondary structure from the inertial $\mathcal{K}-$frame, and with the experimental research of Ueno et al. [5], one can identify the secondary structure as a limit case of the core structure. Speaking of a limit case is motivated by the fact, that the shown trajectories are not free of surface interactions. In analogy to the subcritical case it is reasonable to define supercritical core particles as particles that are trapped in the central vortex flow. Additionally core particles do not get in contact with the liquid free surface. Therefore, the trajectories of the secondary structure do not represent core particles by the given definition.

Further integration until $t = 20$ yields for another 6 (out of 20) secondary structure particles attraction to SL-I-PAS. The changeover from the secondary structure to SL-I-PAS is shown in figure 8.11 observed from the rotating $\mathcal{K}'-$frame and in figure 8.12 observed from the inertial $\mathcal{K}-$frame. The upper images show the trajectory within the time period $t = [5, 8.6]$ where the particle is moving exclusively in the secondary structure. For a better view onto the particle movement, the trajectory is split-up and the final position of the

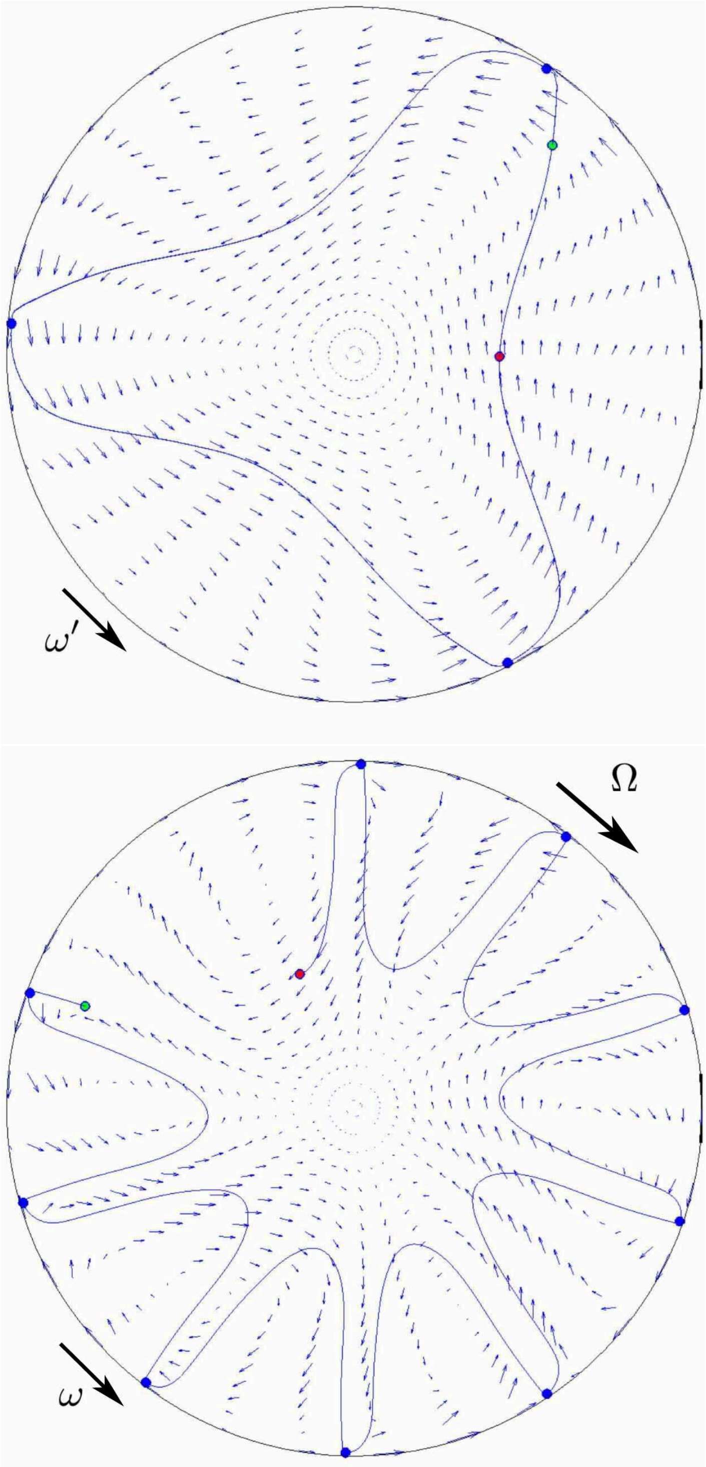

Figure 8.9: SL-I-PAS particle trajectory from above for the time period of 2 full HTW revolutions. Upper image: Observation from the rotating frame $\mathcal{K}'$. Lower image: Observation from the inertial frame $\mathcal{K}$. The green dot indicates the particle's starting position, the red dot its final position and the blue dots indicate free surface collisions.

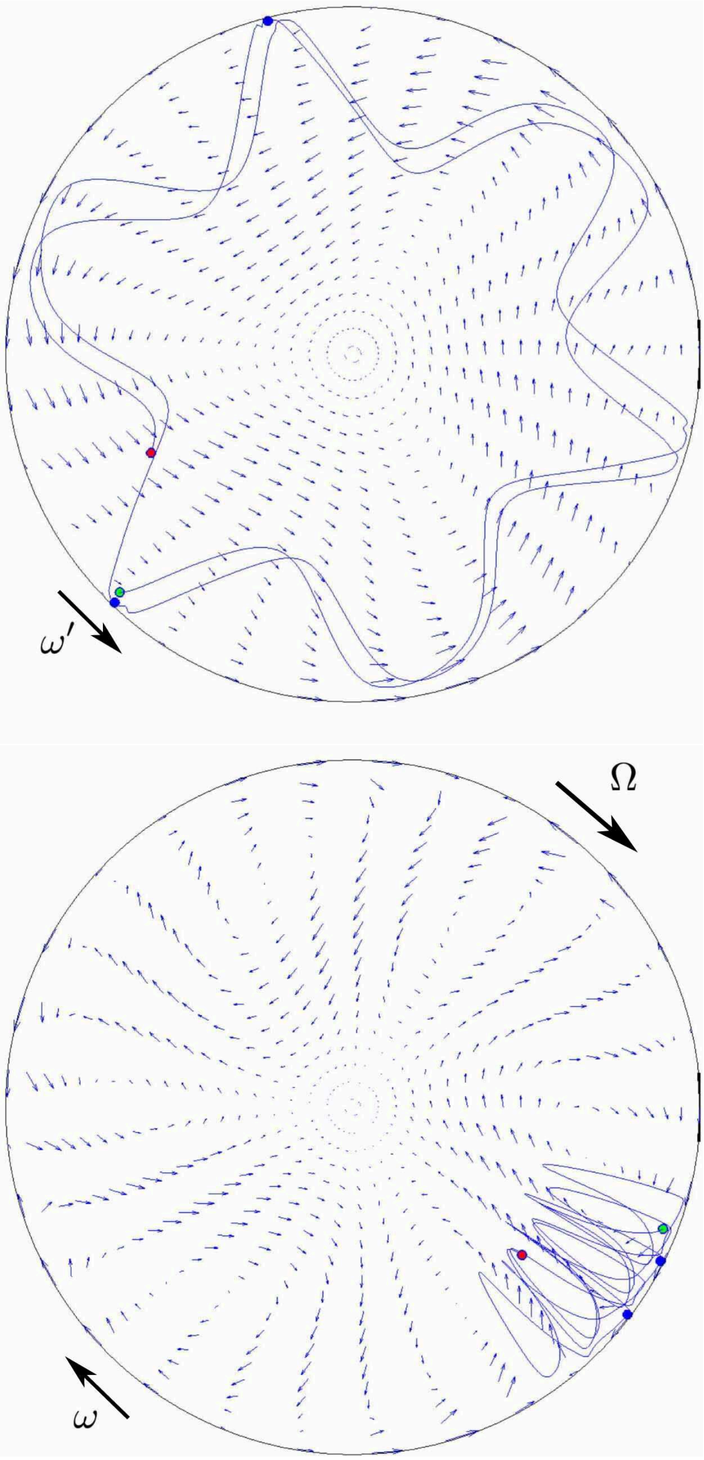

Figure 8.10: Trajectory of a secondary structure particle from above for the time period of 2 full HTW revolutions. Upper image: Observation from the rotating frame $\mathcal{K}'$. Lower image: Observation from the inertial frame $\mathcal{K}$. The green dot indicates the particle's starting position, the red dot its final position and the blue dots indicate free surface collisions.

upper image corresponds to the starting position of the lower image. This position is chosen slightly before the most peculiar change of the particle movement takes place, where the changeover to PAS is initiated. Due to the absence of surface interaction the changeover is initiated by the flow only, but it seems to be most likely that the following sequence of surface interactions is important to stabilize the trajectory to PAS. The possibility of a transfer to the stable SL-I-PAS identifies the secondary structure as a transient state.

8.3.2 Poincaré map

For the visualization of the particles chronological development a proper quantity is needed. The chosen quantity is the intersection point of a trajectory with the mid-plane $z = 0$. Furthermore, it is differentiated between top-down intersections (blue indicated) and bottom-up intersections (green indicated). This visualization corresponds to a basic Poincaré map and is shown for two selected trajectories on the left hand side of figure 8.13.

The right hand side of figure 8.13 shows another visualization strategy of the corresponding trajectories, called from now on DFT-fingerprint. The DFT-fingerprint is found by a Fourier transform of the azimuthal coordinates of the Poincaré intersection points $\varphi'_n|_{z=0}$ representing the set of all top down intersections of a single trajectory with the mid-plane $z = 0$. This set of real coordinates results in a set of complex Fourier coefficients $\tilde{a}_n$, whereas a DFT-fingerprint plot represents the normalized amplitudes $|\tilde{a}_n|$. Due to the fact that especially different types of trajectories realize a different number of intersections in the same time period, the abscissas are not equal and fingerprints are therefore only comparable qualitatively. However, the DFT-fingerprint is a very helpful tool for a quick classification of trajectories. The zero-component $|\tilde{a}_0|$ is suppressed in all DFT-fingerprint plots.

Figure 8.13 shows an example for both types of the introduced trajectories. As expected, the SL-I-PAS is represented by a single pair of Fourier coefficients and in turn the core trajectory is represented by a slightly diffuse Fourier spectrum around two distinct modes.

8.3.3 Domains of attraction

In reference to the subcritical case, the collision of particle and liquid free surface seems to be the major effect for PAS development. For the subcritical case it was established that any collision of a particle with the liquid free surface results in a (rapid) transfer to PAS.

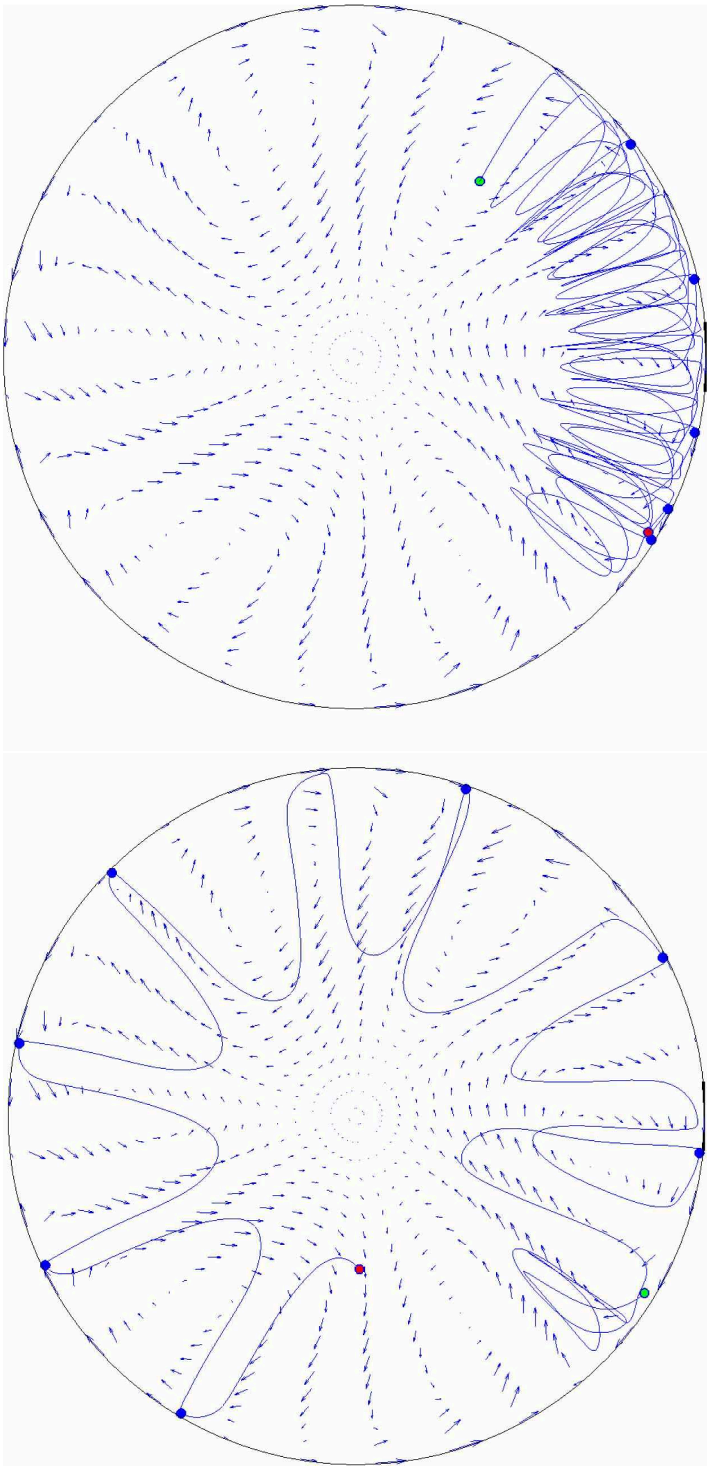

Figure 8.11: Changeover from the secondary structure to SL-I-PAS for $\varphi_{\text{init}} = 138°$ observed from the inertial $\mathcal{K}-$frame. Upper image: time interval $t = [5, 8.6]$. Lower image: time interval $t = [8.6, 10.5]$. The green dot indicates the particle's starting position, the red dot its final position and the blue dots indicate free surface collisions.

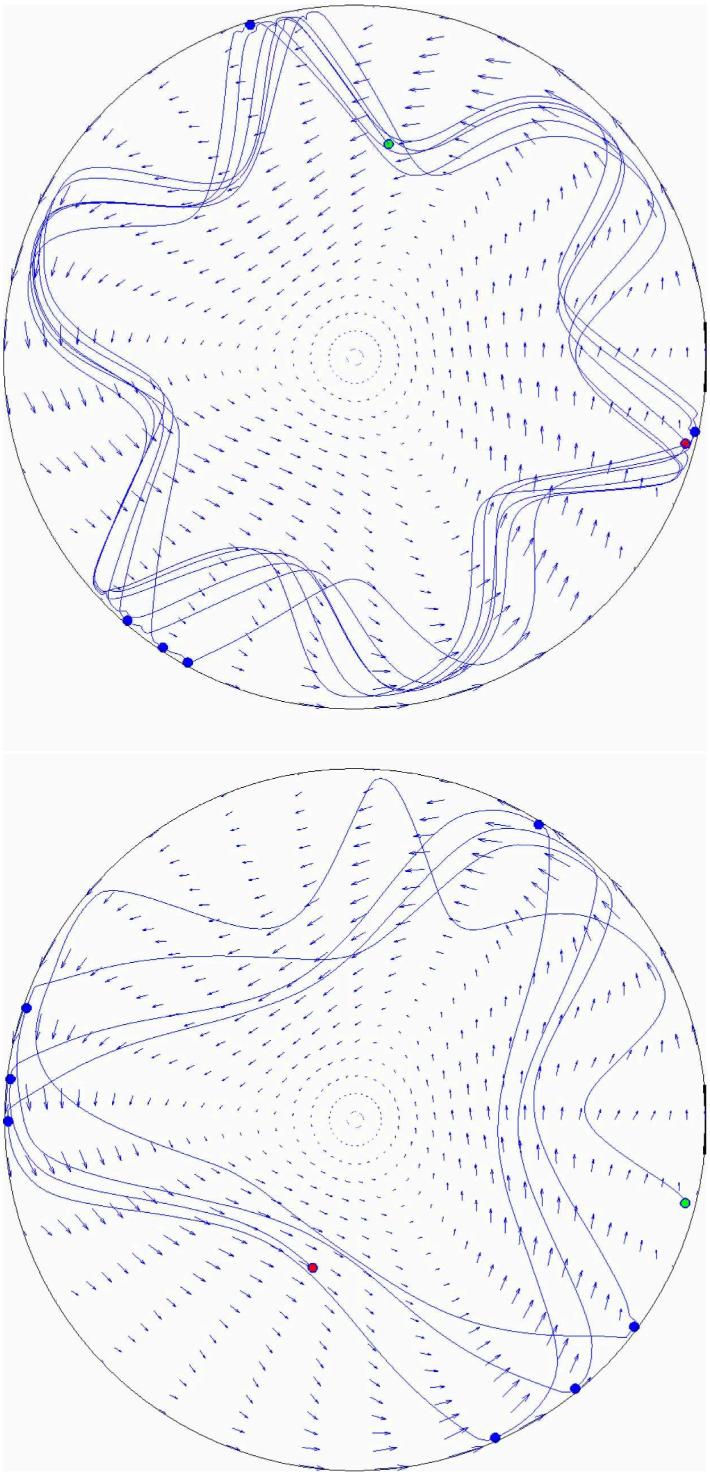

Figure 8.12: Changeover from the secondary structure to SL-I-PAS for $\varphi_{\text{init}} = 138^\circ$ observed from the rotating $\mathcal{K}'-$frame. Upper image: time interval $t = [5, 8.6]$. Lower image: time interval $t = [8.6, 10.5]$. The green dot indicates the particle's starting position, the red dot its final position and the blue dots indicate free surface collisions.

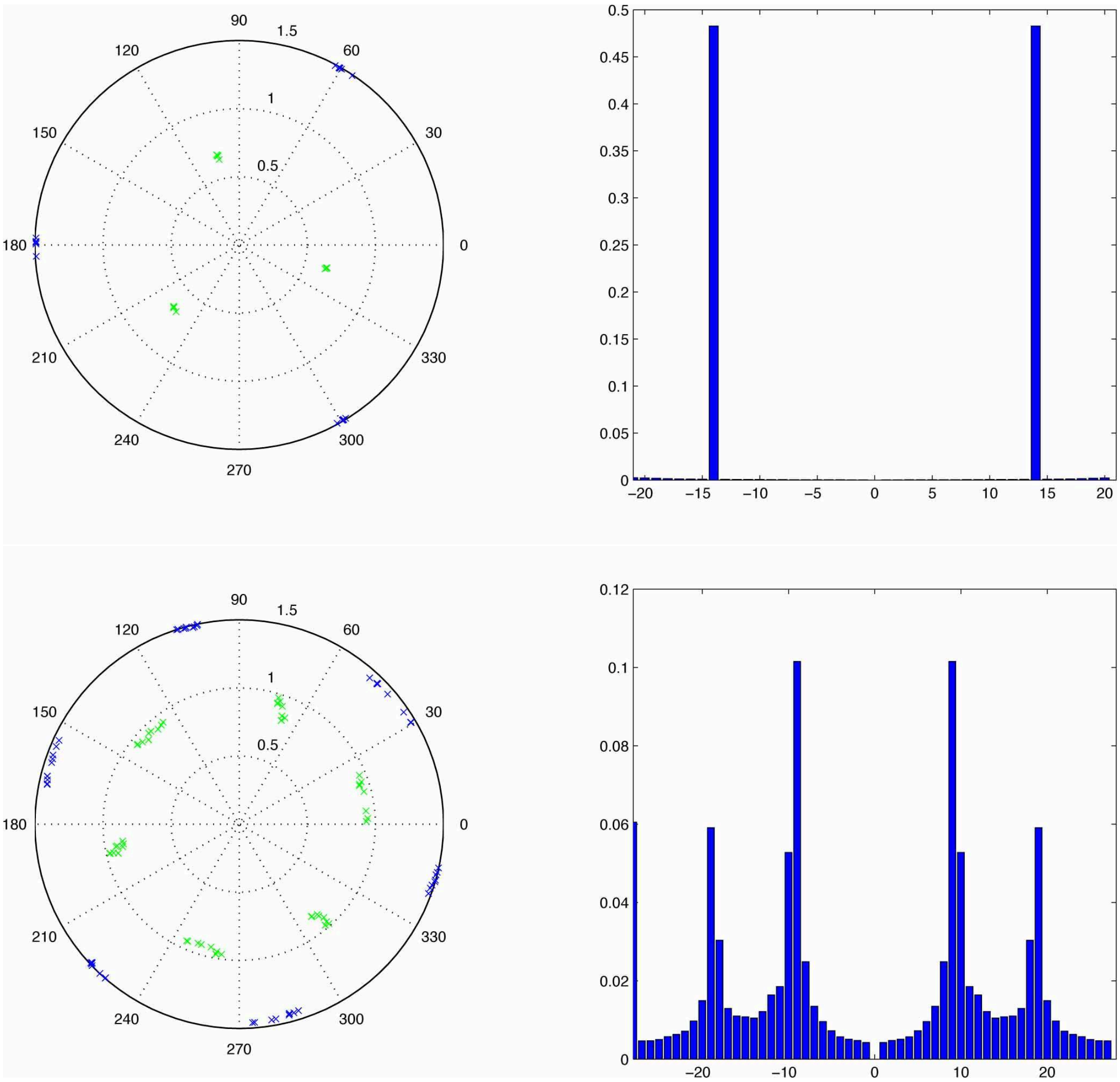

Figure 8.13: Upper images: SL-I-PAS trajectory ($\varphi'_{\text{init}} = 50°$), Lower images: core trajectory ($\varphi'_{\text{init}} = 100°$). Left column: Poincaré maps with plane $z = 0$ for $t = [0, 6]$. Blue markers indicate top-down movement, green markers indicate bottom-up movement. Right column: DFT-fingerprints of the respective trajectory.

All initial positions of the supercritical simulation already comply with the subcritical requirement of a surface collision. Hence, the direct translation of the found subcritical PAS condition to the supercritical case would mean rapid PAS development for all simulated particles due to the given surface collision. However, as demonstrated, some particles remain in long transient states and it is no longer true that PAS develops rapidly and therefore necessarily due to any surface collision. This observation has to result in a modification of the 2D PAS-condition for supercritical flows.

If PAS does not develop necessarily from every initial position, corresponding to a surface collision, one needs an estimate of the PAS domains of attraction. For that reason, the azimuthal coordinates of all Poincaré intersection points $\varphi'_n|_{z=0}$ are plotted altogether for all trajectories. This is done in figure 8.14, showing $\varphi'_n|_{z=0}$ of all trajectories on the ordinate vs. the trajectories' initial angles φ'_{init} for the total time period $t = [0, 6]$. Again, blue and green markers distinguish between ascending and descending movement.

Most peculiar is the nearly straight line from the bottom left to the top right corner, representing all first Poincaré intersection points, and two sets each with three horizontal significant lines, representing the Poincaré intersection points of particles forming PAS. Furthermore the image stands out due to alternating vertical segments of approximately same size.

For getting a better view on the introduced map, figure 8.15 shows the map again but with a reduced time period without transient phase, i.e. for $t = [2, 6]$. Additionally the initial angle φ'_{init} is now replaced by the initial surface release angle $\varphi'_1|_{L_1}$, a more representative value. The initial surface release angle is defined as the first azimuthal coordinate of the position where the tracer stops its exclusive sliding movement and releases from the surface to travel inwards again. For the present particle parameters all release points will accord in excellent approximation to L_1 and L_3 respectively. The already mentioned alternating segments are now bordered by vertical red lines with an exact spacing of $\Delta\varphi' = 60°$. The choice seems to be a good first guess in consideration of the HTW's fundamental wave number $m = 3$. The first border is defined at $\varphi'_1|_{L_1} = 28°$.

Figure 8.15 shows that PAS development is basically distributed over the entire unit circle but there are three significant segments confining PAS-forming trajectories only. These segments will be called from now on **A-segments**. Particles with a surface release angle within an A-segment are transferred to PAS rapidly. Therefore, the A-segments can be understood as a subspace (in position space) of the domain of attraction (in the phase space) for PAS. For the remaining segments, called from now on **R-segments**, a statement is not possible for now. A particle with a surface release angle within one of the R-segments

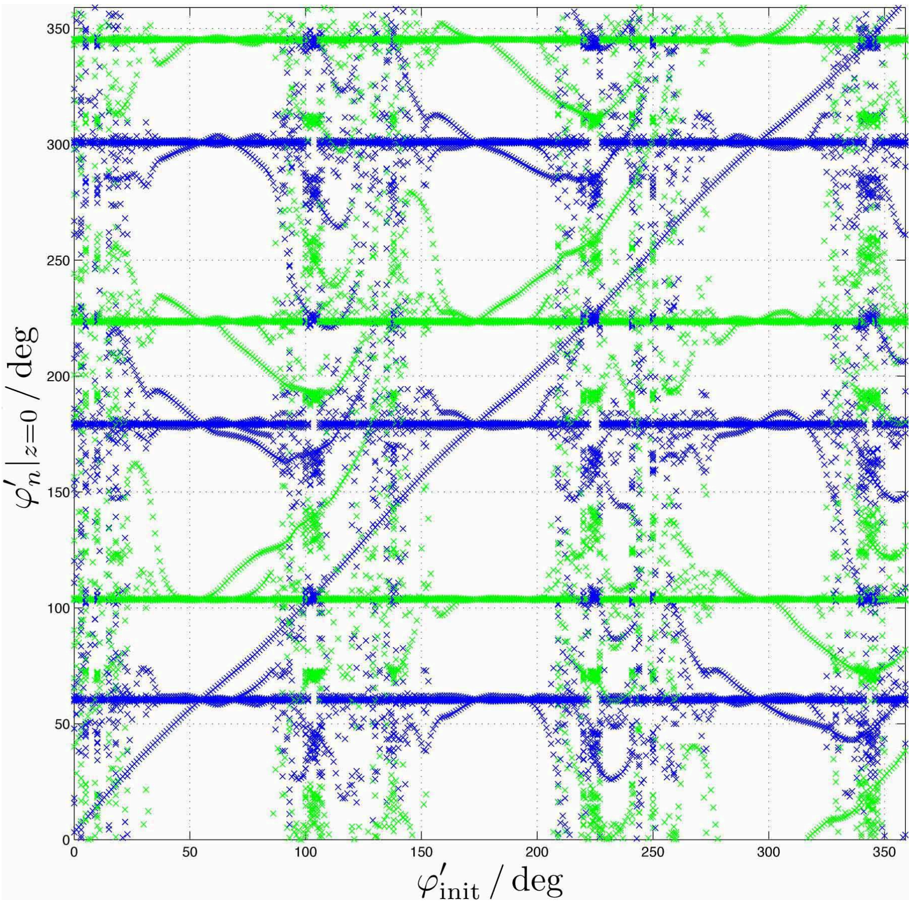

Figure 8.14: Azimuthal coordinate of all Poincaré intersection points $\varphi'_n|_{z=0}$ vs. particle initial angle φ'_{init} for total time period $t = [0, 6]$. Blue markers indicate top-down, green markers indicate bottom-up movement.

is, in contrast to a particle releasing in an A-segment, not determined whether it will form PAS or not.

8.3.4 Influence of surface collision

For subcritical flow it was shown that the interaction of particle and liquid free surface is a **necessary and sufficient** condition for PAS development. The recent simulation shows that this is no longer true for supercritical flows.

Figure 8.16 shows the projections of all computed trajectories on the unrolled cylinder surface at $R^\dagger$ for the short starting period $t = [0, 0.03]$. Red dots indicate particle-surface collision points, blue dots surface release points. Every particle starts at the same height

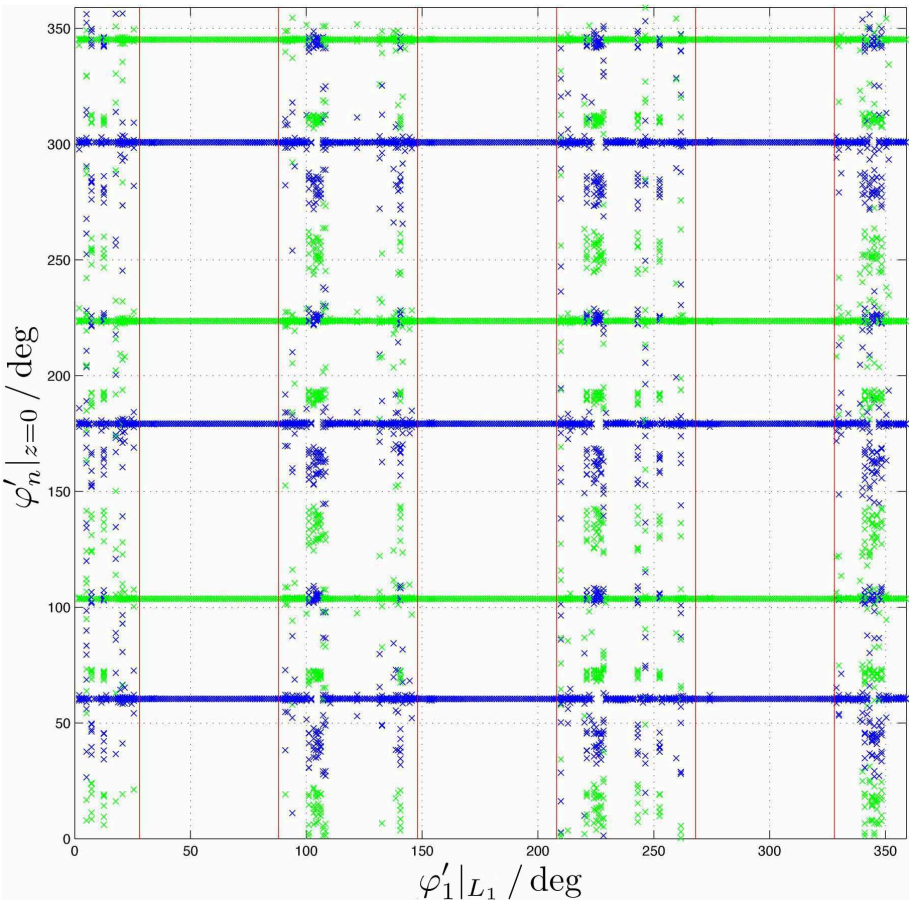

Figure 8.15: Azimuthal coordinate of all Poincaré intersection points $\varphi'_n|_{z=0}$ vs. initial surface release angle $\varphi'_1|_{L_1}$ for reduced time period $t = [2, 6]$. Blue markers indicate top-down, green markers indicate bottom-up movement. Vertical red lines confine segments of exactly $\Delta\varphi' = 60°$.

$z = 0.4$ with a surface collision, slides along the surface until it reaches the release line L_1, where it releases from the surface again.

In the top image all trajectories with a surface release angle within an A-segment are blue-coloured, all those with a surface release angle within a R-segment are red-coloured, as one can easily proof with the vertical red borders. Obviously all blue trajectories release at L_1 only, whereas the majority of all red trajectories release from L_3 as well. The bottom image illustrates whether a particle will reach PAS (blue coloured) or not (red coloured) within a time period of $t = [0, 6]$.

From the bottom image of figure 8.16 the behaviour of particles with a surface release from L_1 within an A-segment seems to be clear. It is most likely that all particles emerging

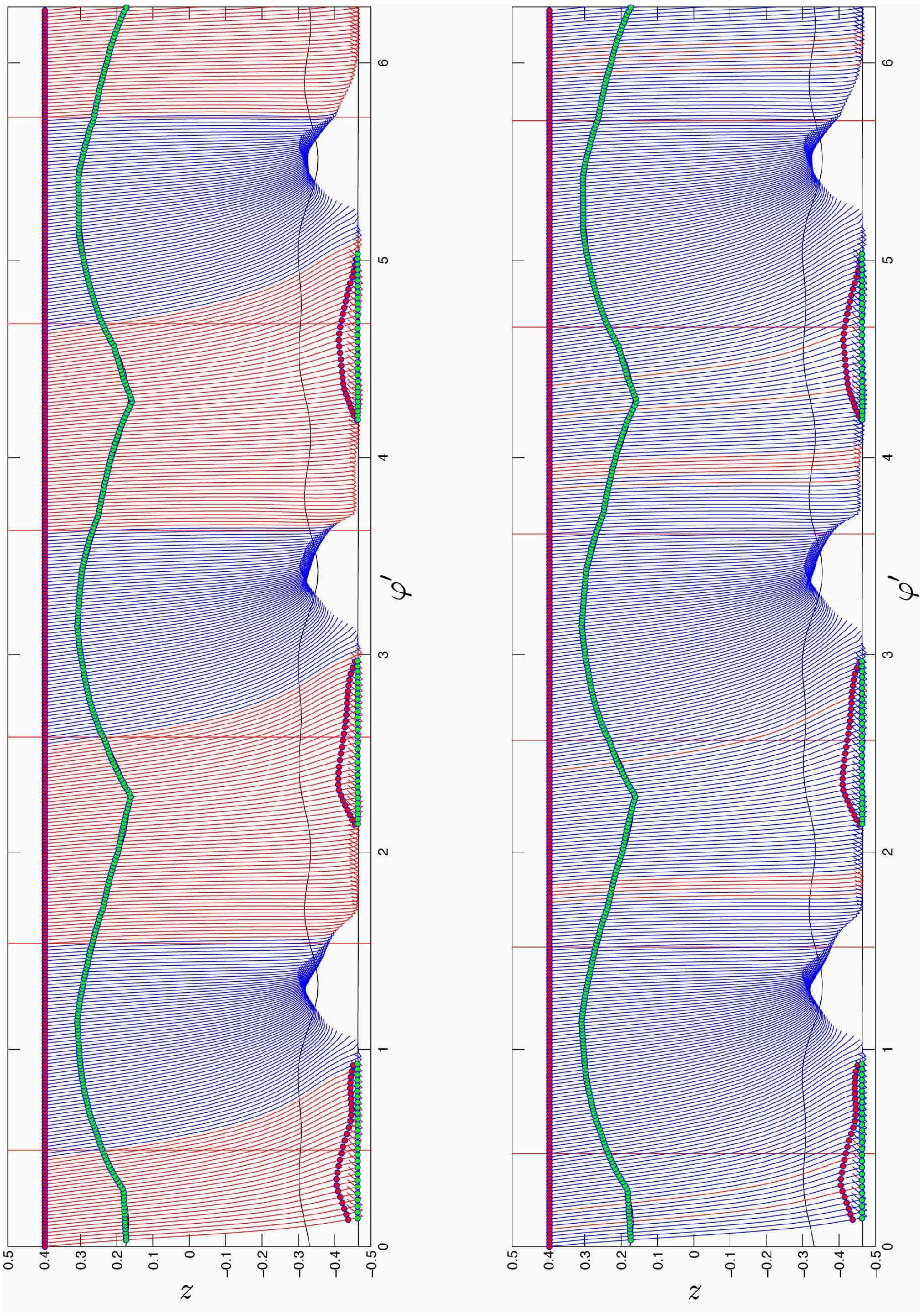

Figure 8.16: Unrolled cylinder surface at $R^\dagger$ with trajectory projections for the starting period $t = [0, 0.03]$. Red dots indicate collision points, blue dots release points. Top: Blue trajectories are of surface release angle within A-segments, red trajectories are within R-segments. Bottom: Blue trajectories indicate PAS-particles, red trajectories indicate no-PAS particles at $t = 6$.

from release line L_1 within an A-segment are transferred to PAS in a one-to-one analogy to the subcritical case. In turn a PAS-transfer for particles releasing from L_3 within an A-segment is not guaranteed.

The treatment of the R-segments is more delicate. From the bottom image of figure 8.16 one is not able to find a correlation between PAS development, initial positions and initial surface release angles respectively. Neither particles emerging from L_1 in one of the R-segments nor particles emerging from L_3, independently if the release point is in an A- or R-segment, show clear characteristics. The PAS development of particles starting in R-segments is therefore possibly not primarily dependent on the initial position and the initial surface release angle respectively, and has something to do with the temporal development of the trajectory.

For covering the temporal development of the trajectories with respect to the surface collisions, figure 8.17 shows in dependency of the initial surface release angle a frequency distribution of liquid free surface releases. The top image shows the total number of surface releases in all A-segments and the bottom image shows the total number of surface releases in all R-segments for every single particle. All red bars below the abscissa indicate no-PAS trajectories.

From figure 8.17 one can follow:

1. All particles with an initial surface release angle within an A-segment are free of R-segment collisions.
2. All tracers without a single A-segment surface release are no-PAS particles. $\Longrightarrow$ **The A-segment surface release is a necessary condition for PAS development.**
3. Not all tracers with A-segment surface releases are in PAS. $\Longrightarrow$ **The A-segment surface release is not a sufficient condition for PAS development**

To get a final PAS-condition holding for all particles, another frequency distribution, as already done in figure 8.17, is set up but now distinguishing between A-segment surface releases above $z = 0$, corresponding to L_1-releases, and below $z = 0$, corresponding to L_3-releases. The result is shown in figure 8.18.

The upper image of figure 8.18 shows that all particles without any upper A-segment surface release are no-PAS particles. As already carried out, the A-segment surface release is a necessary condition for PAS. Figure 8.18 shows that only particles with upper A-segment releases are forming PAS and all no-PAS particles are those with not a single upper A-segment surface release.

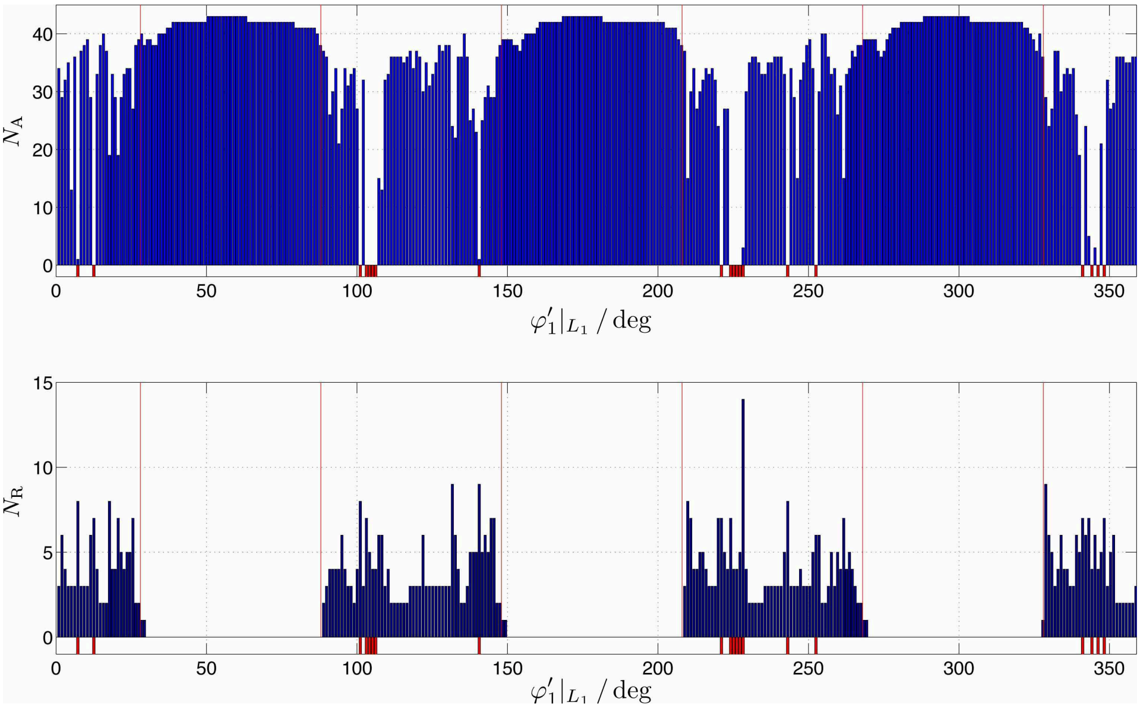

Figure 8.17: Number of surface releases N vs. initial surface release angle $\varphi'_1|_{L_1}$ for total time period $t = [0, 6]$. Top: Total number of surface releases in A-segments N_{A}. Bottom: Total number of surface releases in R-segments N_{R}. Vertical red lines border the segments from each other.

$\Longrightarrow$ **The upper A-segment surface release is the necessary and sufficient condition for supercritical, zero gravity PAS development.**

This means that only stream surfaces emerging from L_1 in certain regions enable PAS development. The stream surface emerging from L_3 does not bring forward PAS development. Even if it seems to be clear that the number of A-segments correlate to the fundamental mode of the HTW, the positions of the borders are still assumptions and for now not deducible from any underlying data.

The PAS forming process goes along with A-segment collisions/releases only, as can be seen from figure 8.17. It seems to be obvious that the constriction of all these trajectories to a 1-dimensional string is an effect of sequenced collisions/releases in A-segments.

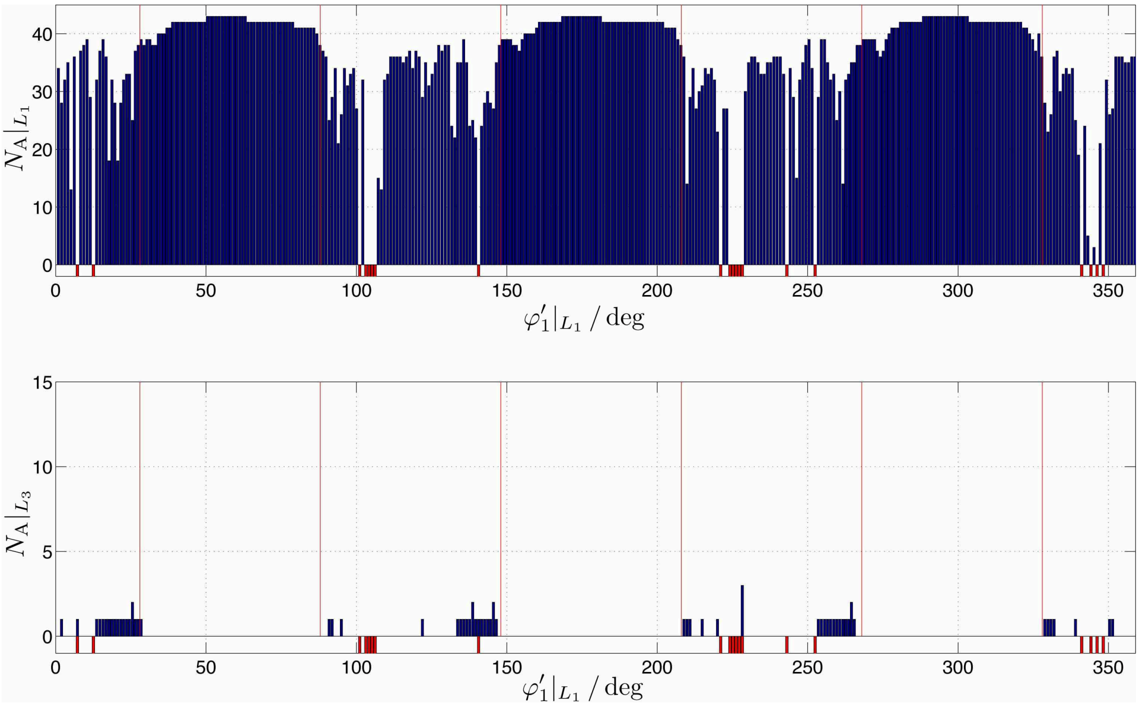

Figure 8.18: Number of A-segment surface releases N_A vs. initial surface release angle $\varphi'_1|_{L_1}$ for total time period $t = [0, 6]$. Top: Total number of upper A-segment surface releases $N_\mathrm{A}|_{L_1}$. Bottom: Total number of lower A-segment surface releases $N_\mathrm{A}|_{L_3}$.

8.3.5 Segment borders

For the present density-matched case, the equations of motion (4.35) reduce to

$$\ddot{\boldsymbol{y}}' = -\frac{2}{3\mathrm{St}}(\dot{\boldsymbol{y}}' - \boldsymbol{u}') + \boldsymbol{u}' \cdot \nabla' \boldsymbol{u}' - 2\boldsymbol{\Omega} \times \left(\dot{\boldsymbol{y}}' - \boldsymbol{u}'\right) . \tag{8.9}$$

Figure 8.19 gives an estimate of the relative velocity difference between particle velocity $\dot{y}_i$ and local fluid velocity u_i

$$\Delta v_i = \left| \frac{u_i - \dot{y}_i}{u_i} \right| \qquad , \qquad i = r, \varphi, z \tag{8.10}$$

for every velocity component. The arising peaks in figure 8.19 are mainly caused by surface interactions. For convenience, Δv_i are forced to zero for all time intervals the particle slides along the liquid free surface. Apart from some remaining peaks, one finds a vanishing particle–flow velocity-mismatch in good approximation, i.e. $\dot{\boldsymbol{y}}' - \boldsymbol{u}' \approx 0$. Together with (8.9) the remaining driving force for the particle equates to the convective derivative of the flow within the $\mathcal{K}'$−frame

$$\ddot{\boldsymbol{y}}' \approx \boldsymbol{u}' \cdot \nabla' \boldsymbol{u}' \tag{8.11}$$

and therefore the particle trajectories and the streamlines of the flow will agree in excellent approximation. This realization will lead to a more interesting conclusion in chapter 11.

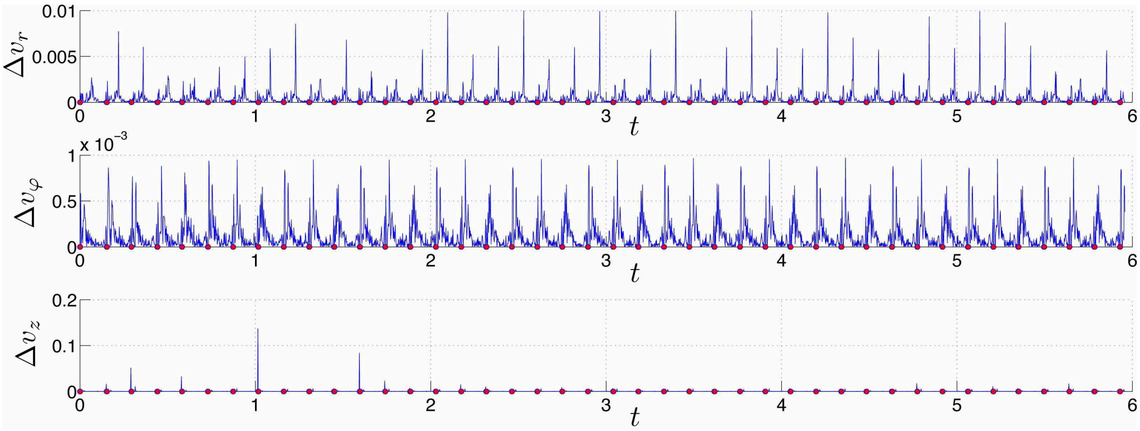

Figure 8.19: Relative velocity differences for a PAS-particle ($\varphi'_{\text{init}} = 50°$) for total time period $t = [0, 6]$. Red dots indicate surface collisions.

For particles sliding along the liquid free surface, the only driving force is the tangential component of the convective derivative, which reads as

$$\boldsymbol{a}'_{\|} = \boldsymbol{e}'_\varphi \left(\frac{u'_\varphi}{R^\dagger} \partial_{\varphi'} + u'_z \partial_{z'} \right) u'_\varphi + \boldsymbol{e}'_z \left(\frac{u'_\varphi}{R^\dagger} \partial_{\varphi'} + u'_z \partial_{z'} \right) u'_z \tag{8.12}$$

and is shown in the uppermost image of figure 8.20. The central image illustrates the azimuthal component of (8.12) only, hence

$$a'_\varphi = \frac{u'_\varphi}{R^\dagger} \partial_{\varphi'} u'_\varphi + u'_z \partial_{z'} u'_\varphi \tag{8.13}$$

and the lowermost image represents the normalized spatial derivative of the azimuthal component

$$\frac{\partial_{\varphi'} a'_\varphi}{\max |\partial_{\varphi'} a'_\varphi|} \tag{8.14}$$

together with the projection of the SL-I-PAS. All images show the upper release line L_1 as well. The expected perfect periodicity of $2\pi/3$ is missing due to the interpolation procedure. One has to keep in mind that not a single value of any field variable is given at $R^\dagger$.

The most important image of figure 8.20 is the central one, showing the azimuthal force acting on a particle that is sliding along the liquid free surface. The information of the lowermost image is in principle equivalent to that of the central image but the picture is more intuitive and interpretation is easier. The azimuthal derivative of the central image shows an acceptable correlation between the segment borders and the regions that are divergent and convergent respectively. **The A-segments appear as those regions where the azimuthal acceleration is convergent.**

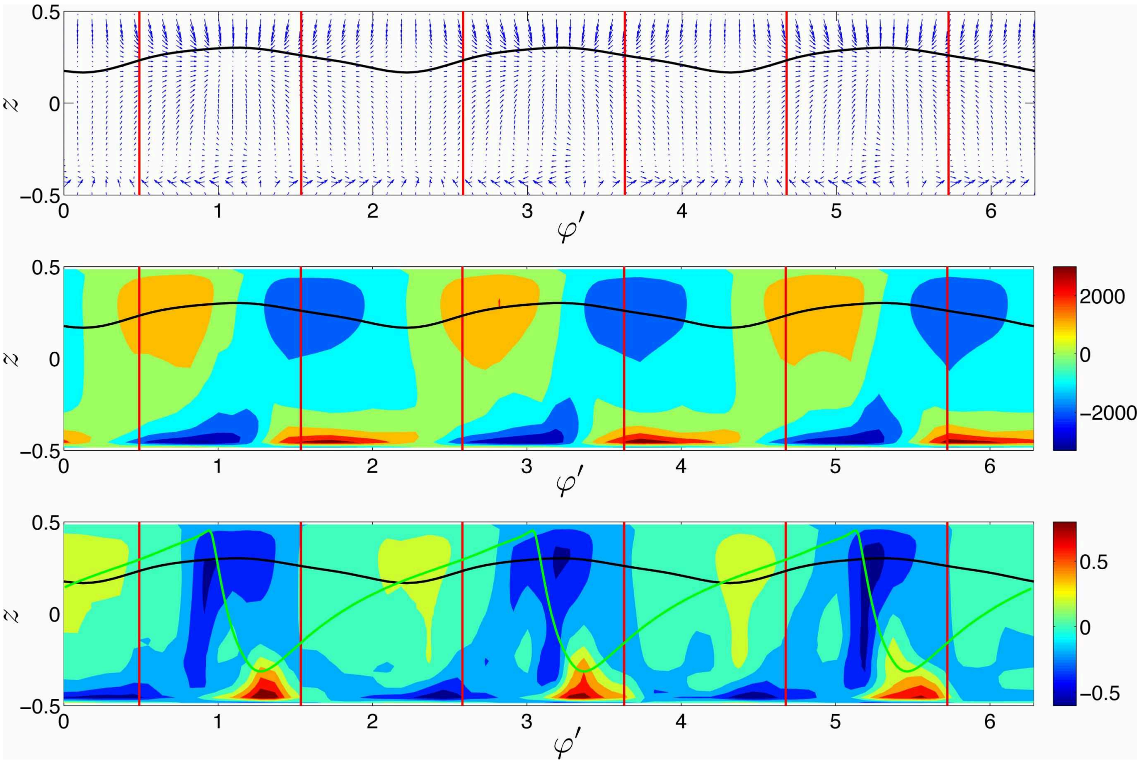

Figure 8.20: Topmost image: tangential acceleration (8.12) at $R^\dagger$. Central image: azimuthal acceleration (8.13) at $R^\dagger$. Lowermost image: normalized azimuthal derivative of the azimuthal acceleration (8.14).

8.3.6 Convergence to PAS

The last section has shown that only those particles are attracted to PAS that emerge from L_1 in certain regions. The present supercritical flow represents a nontrivial, incompressible, three-dimensional flow, where the closure of streamlines is no longer stringent as this is the case for the incompressible two-dimensional (subcritical) flow. Due to that reason streamlines emerging from L_1 are in general no longer tangent streamlines as in the subcritical flow. Hence, these streamlines will in general intersect the cylinder surface of the contact radius again. If the intersection of trajectory and cylinder surface takes place in an A-segment then the tangential acceleration will lead to a focussing behaviour and the final constriction of the trajectories to a single string.

Figure 8.21 shows the iterated map $\varphi'_n|_{z=0} \rightarrow \varphi'_{n+1}|_{z=0}$ where $\varphi'_n|_{z=0}$ stands for sequenced (top down) angles of the Poincaré intersection points φ_n of a single trajectory. The map illustrates only the development of trajectories with an initial surface release angle within the first A-segment. It shows that all particles, once released from the liquid free surface in the upper region of an A-segment, are attracted to a fixed point corresponding to the surface release point of PAS. This fixed point is the intersection point of the map with the diagonal.

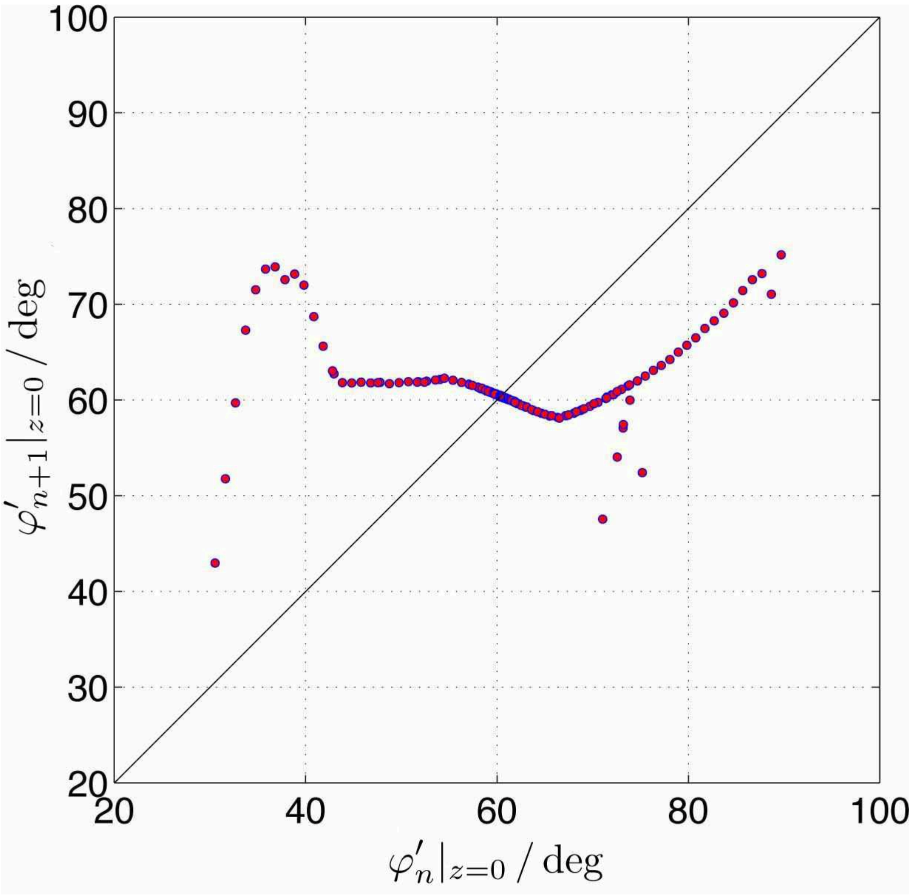

Figure 8.21: Iterated map $\varphi'_n|_{z=0} \rightarrow \varphi'_{n+1}|_{z=0}$.

9 Slightly supercritical: Re $= 1300$

This chapter will test the found PAS-condition for a slightly supercritical flow by varying the particle size as well.

9.1 Simulation parameters

Flow parameters

This slightly supercritical zero gravity flow is defined by

$$\mathrm{Pr} = 4 \quad , \quad \Gamma = 0.66 \quad , \quad \mathrm{Re} = 1300 \quad , \quad \mathrm{Gr} = 0 \quad , \quad \mathrm{Bi} = 0\,. \tag{9.1}$$

The fundamental wave number of the arising HTW is again $m = 3$. Some Fourier analysis of the temperature field's temporal development at certain checkpoints (given by Poseidon in separate output file) yields for the HTW's angular velocity

$$\Omega = -8.90\,. \tag{9.2}$$

The grid resolution is chosen as $N_r \times N_z \times N_\varphi = 50 \times 40 \times 14$. The grid compression factors are $f_r = 0.96$ in radial and $f_z = -0.93$ in axial direction with reference points $z = 0$ and $r = R = 1.515$.

The procedure to find the travelling wave solution is equivalent to section 8.2.1. The simulation is started with $\boldsymbol{u} = 0$ and $T = z$ and reaches the unstable 2D–state within a dimensionless time period of $t = 2$. The parameters of the temperature field perturbation are $A_T = 0.1$, $m = 3$ and $\varphi_0 = 0$. The emanating unstable standing wave is shown in figure 9.1 for $t_1 = 2$ and $t_2 = 4$ where $t = 0$ stands for the instant at which the temperature perturbation field is imposed.

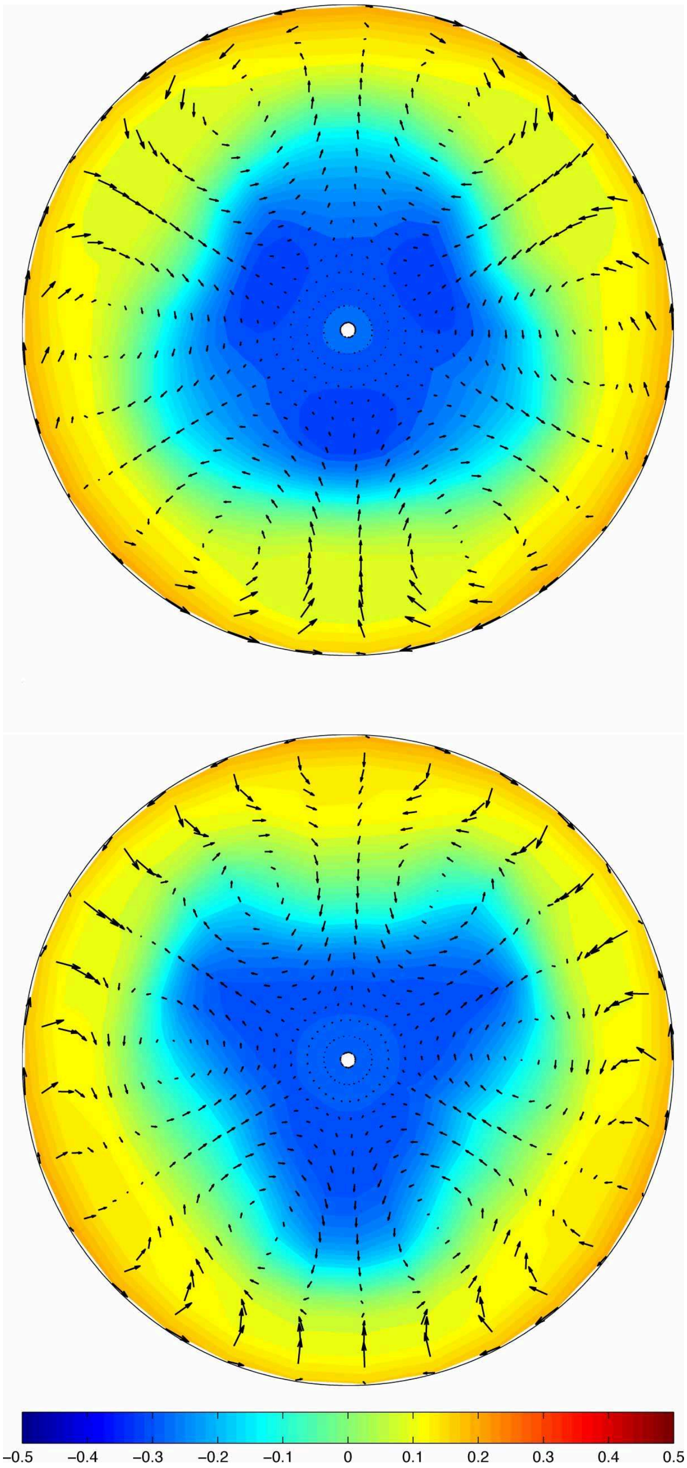

Figure 9.1: Standing wave development after $t_1 = 2$ (top) and $t_2 = 4$ (bottom) with $t = 0$ as temperature perturbation onset. The images show the velocity field $\boldsymbol{u}(\boldsymbol{x}, t_i)$ and the temperature field $T(\boldsymbol{x}, t_i)$ in the mid-plane $z = 0$ from the inertial frame of reference $\mathcal{K}$.

The parameters for the perturbation of the velocity field are $A_r = -10$, $A_\varphi = 6$ and $A_z = 3$ all with $m = 3$ and $\varphi_0 = 100°$. The well formed travelling wave solution is found at $t_0 = 10$, where $t = 0$ stands for the velocity field perturbation onset. The horizontal cross section of the liquid bridge is shown in figure 9.2.

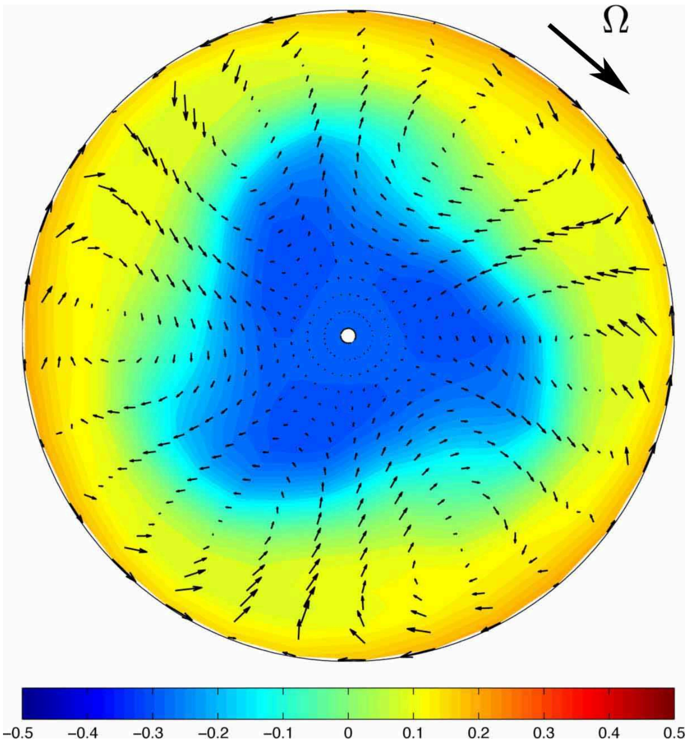

Figure 9.2: Travelling wave solution at $t_0 = 10$ developed from the standing wave after the velocity perturbation onset at $t = 0$. The image shows the velocity field $\boldsymbol{u}(\boldsymbol{x}, t_0)$ and the temperature field $T(\boldsymbol{x}, t_0)$ in the mid-plane $z = 0$ from the inertial frame of reference $\mathcal{K}$.

Particle parameters

The variation of the particle size concentrates onto ”small particles” and ”large particles”. From a given Stokes number and an assumed liquid bridge of radius $R \approx 3\,\mathrm{mm}$, the dimensional particle diameters d_p follow from $d_\mathrm{p} = 2\Gamma R\sqrt{4.5\,\mathrm{St}}$ and are for the chosen parameters

$$\begin{aligned} \mathrm{St} = 6 \cdot 10^{-6} \quad &\longrightarrow \quad d_\mathrm{p} \approx 21\,\mu\mathrm{m}\,, \\ \mathrm{St} = 5 \cdot 10^{-5} \quad &\longrightarrow \quad d_\mathrm{p} \approx 60\,\mu\mathrm{m}\,. \end{aligned} \tag{9.3}$$

The remaining particle parameters are

$$\varrho = 1 \quad , \quad \mathrm{Fr} = \infty \, . \tag{9.4}$$

Initial positions

The initial positions are again chosen at the contact radius $R^\dagger$, in vertical direction at $z = 0.4$ and azimuthally in the reduced segment $\varphi = [0°, 120°]$ spaced by $\Delta\varphi = 2°$, i.e.

$$\boldsymbol{Y}'_{\text{init}} = \{\boldsymbol{Y}' \in \mathbb{R}^6 \,|\, r' = R^\dagger \, , \, \varphi' = \frac{k\pi}{180} \, , \, z' = 0.4 \, , \, \dot{\boldsymbol{y}}' = \boldsymbol{u}'(\boldsymbol{x}')\} \quad , \quad k = 0, 2, 4, \ldots, 120 \, . \tag{9.5}$$

To reduce numerical effort and due to the periodicity of the flow, the reduced segment should give a representative result. The integration time was chosen as $t = 6$, corresponding to $N_\Omega \approx 8.5$ HTW revolutions, determined by (8.4).

9.2 Results

Figure 10.2 shows the already introduced map (collection of all Poincaré maps) for the reduced time period $t = [3, 6]$ for small and large particles.

The result for the small particles seem to be clear and PAS does not occur for the considered time period. Chapter 11 will show that PAS development is most likely impossible for this case and the time period is not essential.

In turn the large particles form PAS that develops only faintly. Most peculiar for this case is the fact that surface collisions are in general rare events and vanish soon completely. Particles starting from an A-segment ($\varphi' \approx [100°, 120°]$) reach the unfinished PAS by some surface interactions but after PAS has developed partly, surface collisions stop. From this point string constriction stops as well, in accordance to section 8.3.6, and the particles remain in the unfinished PAS as show in figure 9.4.

The final understanding of PAS will be worked out in the following chapters, where one will see that the given results of the large particles in the slightly supercritical flow are partly numerical generated as well.

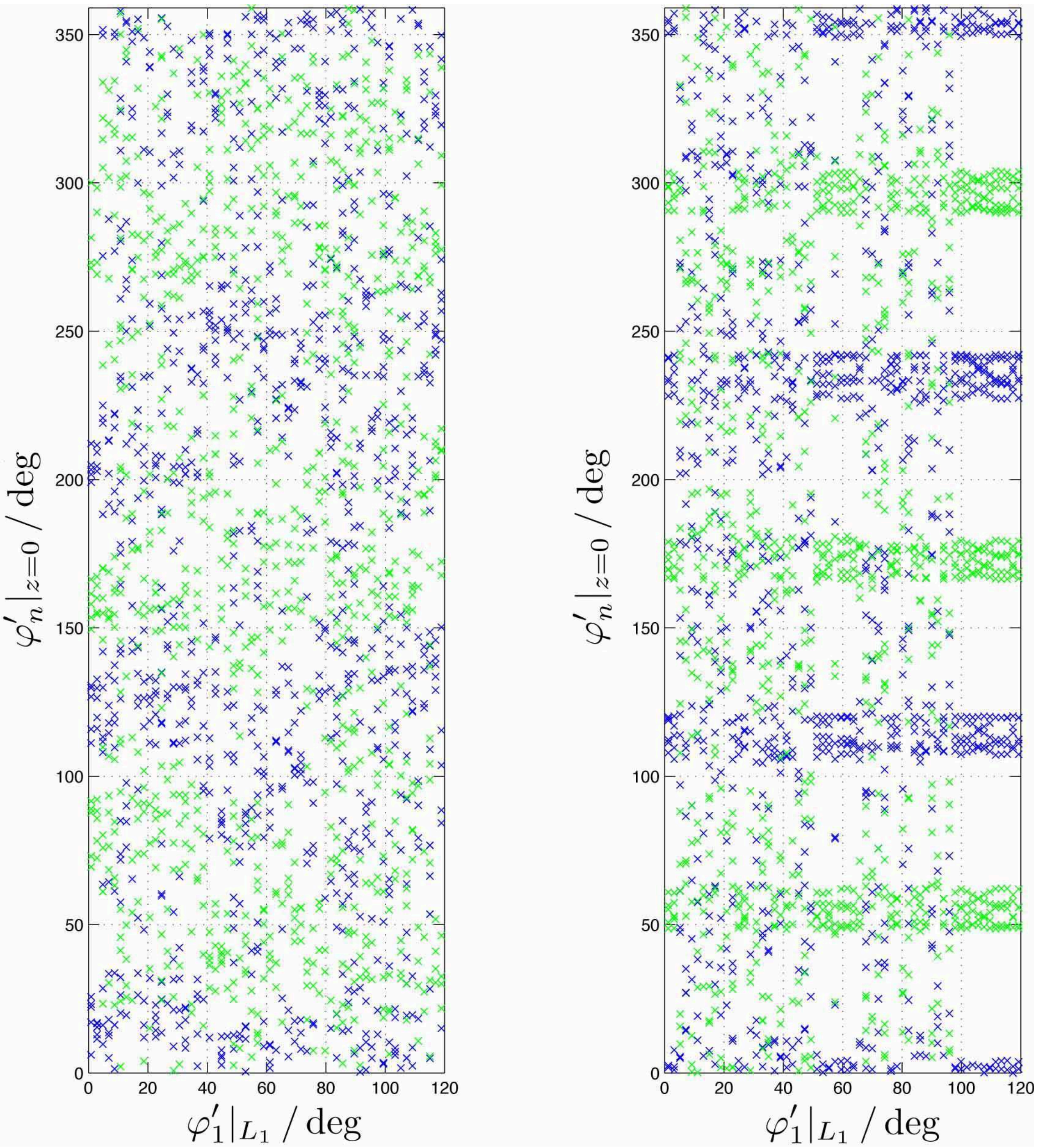

Figure 9.3: Azimuthal coordinate of all Poincaré intersection points $\varphi'_n|_{z=0}$ vs. initial surface release angle $\varphi'_1|_{L_1}$ for reduced time period $t = [3, 6]$. Left image: small particle ($\mathrm{St} = 6 \cdot 10^{-6}$). Right image: large particle ($\mathrm{St} = 5 \cdot 10^{-5}$). Blue markers indicate top-down, green markers indicate bottom-up movement.

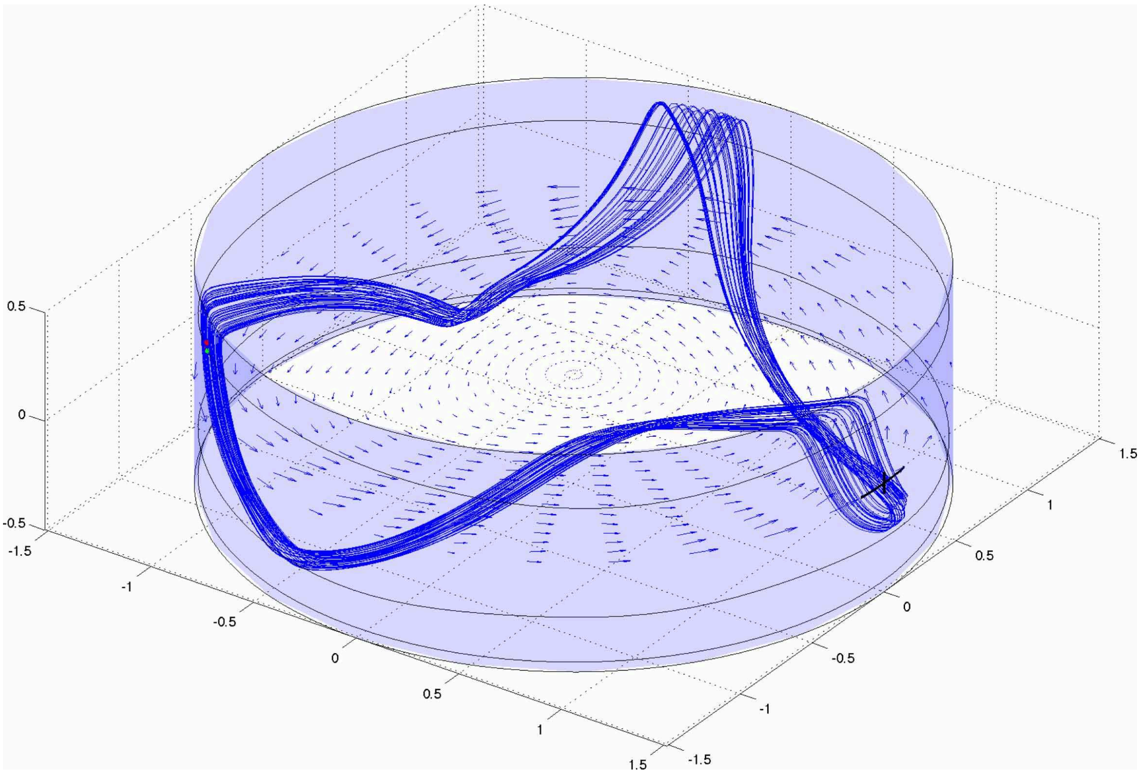

Figure 9.4: PAS development for large particles ($\mathrm{St} = 5 \cdot 10^{-5}$) after surface collisions have stopped for $t = [3, 6]$ and $\varphi'_{\mathrm{init}} = [100°, 120°]$.

10 Supercritical: Re $= 2600$

This chapter focus on another supercritical flow and the results will give rise to a more detailed analysis of the flow topology, discussed in the next chapter.

10.1 Simulation parameters

This supercritical zero gravity flow is defined by

$$\mathrm{Pr} = 4 \quad , \quad \Gamma = 0.66 \quad , \quad \mathrm{Re} = 2600 \quad , \quad \mathrm{Gr} = 0 \quad , \quad \mathrm{Bi} = 0\,. \tag{10.1}$$

The fundamental mode of the arising HTW is again $m = 3$ and the Fourier checkpoint analysis yields for the HTW's angular velocity

$$\Omega = -12.3\,. \tag{10.2}$$

The grid resolution is chosen as $N_r \times N_z \times N_\varphi = 50 \times 40 \times 14$. The grid compression factors are $f_r = 0.96$ in radial and $f_z = -0.93$ in axial direction with reference points $z = 0$ and $r = R = 1.515$.

The procedure to find the travelling wave solution is equivalent to section 8.2.1. Starting from $\boldsymbol{u} = 0$ and $T = z$, the simulation reaches the unstable 2D–state within a dimensionless time period of $t = 0.5$. The parameters of the velocity field perturbation are $A_r = -10$, $A_\varphi = 6$ and $A_z = 3$ all with $m = 3$ and $\varphi_0 = 0$.
The well formed travelling wave solution is found at $t_0 = 5$ where $t = 0$ stands for the velocity perturbation onset. The horizontal cross section of the liquid bridge is shown in figure 10.1.

All particle parameters and initial positions are chosen as in the slightly supercritical case, see (9.3 - 9.5). The integration time was chosen as $t = 8$, corresponding to $N_\Omega \approx 15.7$ HTW revolutions.

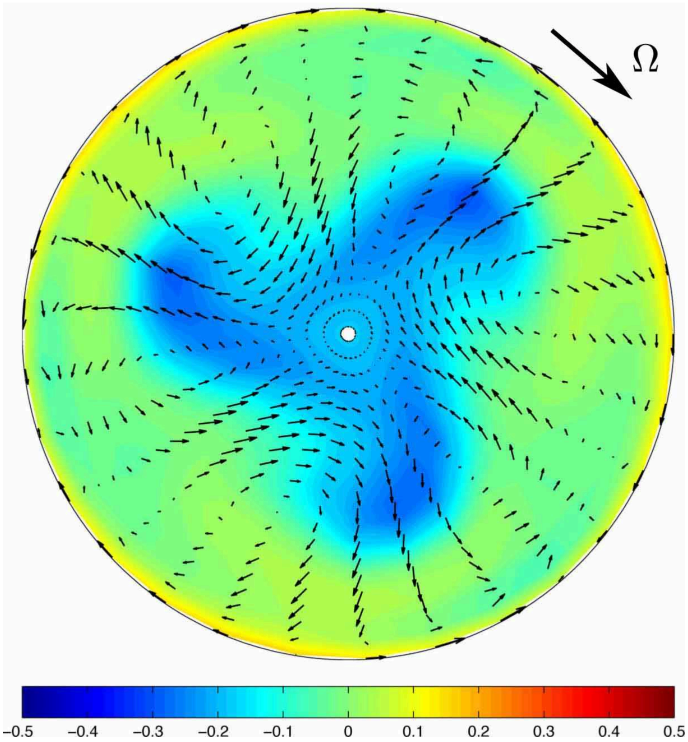

Figure 10.1: Travelling wave solution at $t_0 = 5$ developed from the 2D–state after the velocity perturbation onset at $t = 0$. The image shows the velocity field $\boldsymbol{u}(\boldsymbol{x}, t_0)$ and the temperature field $T(\boldsymbol{x}, t_0)$ in the mid-plane $z = 0$ from the inertial frame of reference $\mathcal{K}$.

10.2 Results

Figure 10.2 shows again the already introduced map for the reduced time period $t = [1, 8]$ for small and large particles. One can easily see that the large particles (right image) are running into PAS rapidly, where in turn the small particles (left image) run into PAS as well but need more time for PAS-development.

The rapid PAS-forming process of the large particles can be estimated from figure 10.3 showing selected trajectories for the time periods $t = [0, 0.35]$, $t = [0.35, 0.7]$ and $t = [1, 1.35]$ where $t = 0.35$ accords approximately to one revolution of a tracer around the $z-$axis.

The lowermost image of figure 10.3 contains qualitatively the same result as found for large particles in the slightly supercritical case (Re = 1300). After PAS is *sufficiently* developed, no more surface collisions occur. Some further analysis of the small particles shows that they form SL-I-PAS in the same manner than the large particles, starting with a short sequence of surface collisions and doing finally without surface collisions. The SL-I-PAS of both considered particle sizes are identical, hence the shape of PAS seems to be independent from the Stokes number. With the already checked assumption that particle and flow velocity agree at any space-time point for sufficiently small, density-matched tracers one can conclude (for now) that PAS represents exactly a closed streamline of the flow. This would mean that PAS is primarily a phenomenon of the hydrothermal wave's topology in combination with the particle–surface interaction model. Hence, PAS formation due to inertial effects caused by the particle size and the density ratio would get second-ranked.

Figure 10.4 shows the projection of PAS and the contact radius for both considered particle sizes in the $r-z-$plane. One can clearly see that $R^{\dagger}$ of the large particle (blue) is nearly tangent (by chance) to PAS where the observed rapid PAS development probably has its origin. In turn the contact radius $R^{\dagger}$ of the small particle (red) is relatively far from PAS and this could be the reason that PAS develops only faintly.

From this observation one can estimate a criterion for a minimum particle size and a minimum Stokes number respectively: If the particle radius is smaller than the minimum distance between the closed streamline and the liquid free surface, a particle transfer to the closed streamline and PAS respectively is not possible. On the other hand figure 10.4 shows that even those particles are attracted to PAS which are actually too small in terms of the given assumption. The attraction of a particle, corresponding in its dynamics to that of an ideal passive tracer, in an incompressible flow without surface interactions is unphysical and most likely caused by a numerical effect. To get a final understanding of the transfer process some more analysis is needed, which is contents of the next chapter.

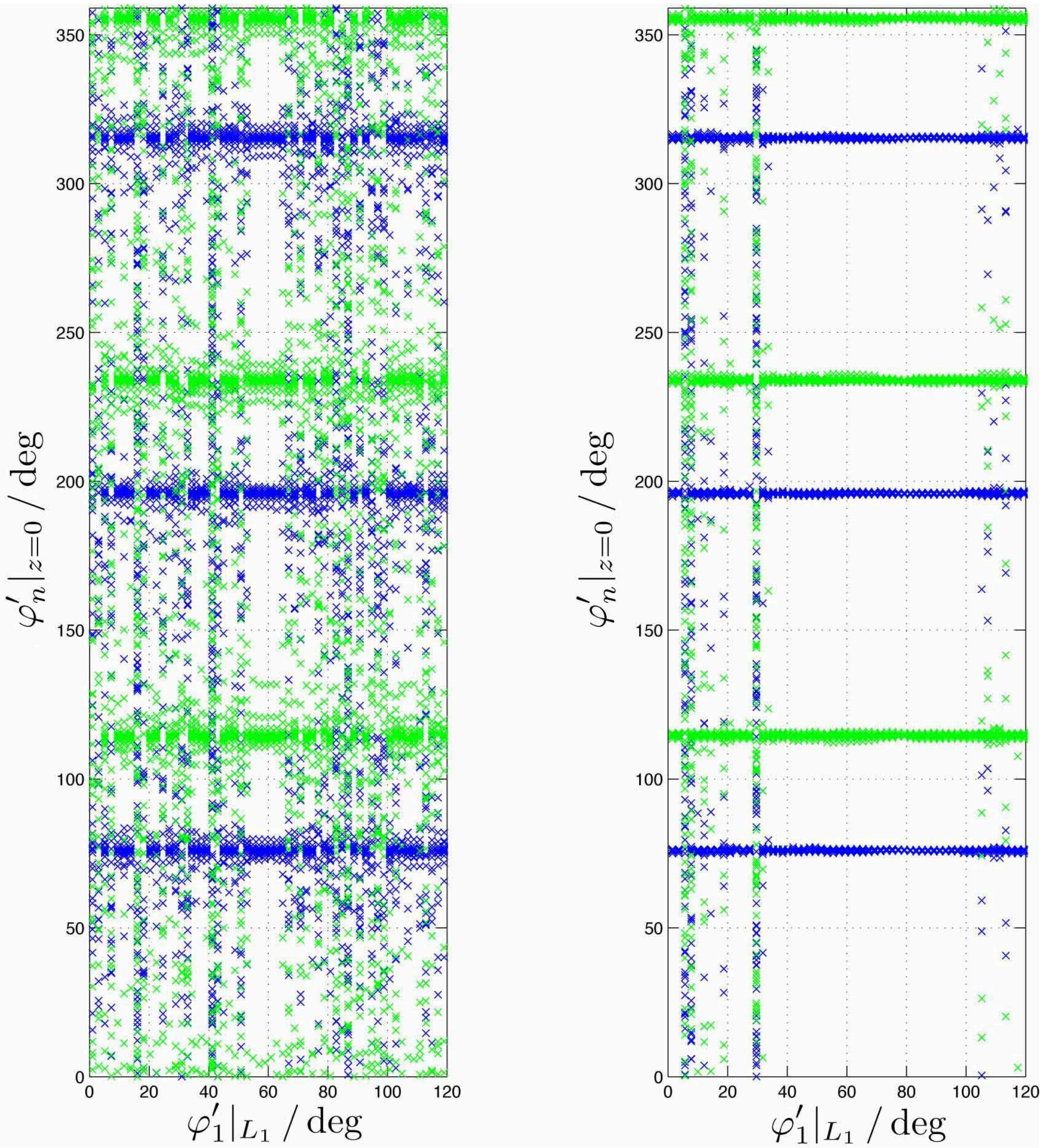

Figure 10.2: Azimuthal coordinate of all Poincaré intersection points $\varphi'_n|_{z=0}$ vs. initial surface release angle $\varphi'_1|_{L_1}$ for reduced time period $t = [1,8]$. Left image: small particle ($\mathrm{St} = 6\cdot 10^{-6}$). Right image: large particle ($\mathrm{St} = 5\cdot 10^{-5}$). Blue markers indicate top-down, green markers indicate bottom-up movement.

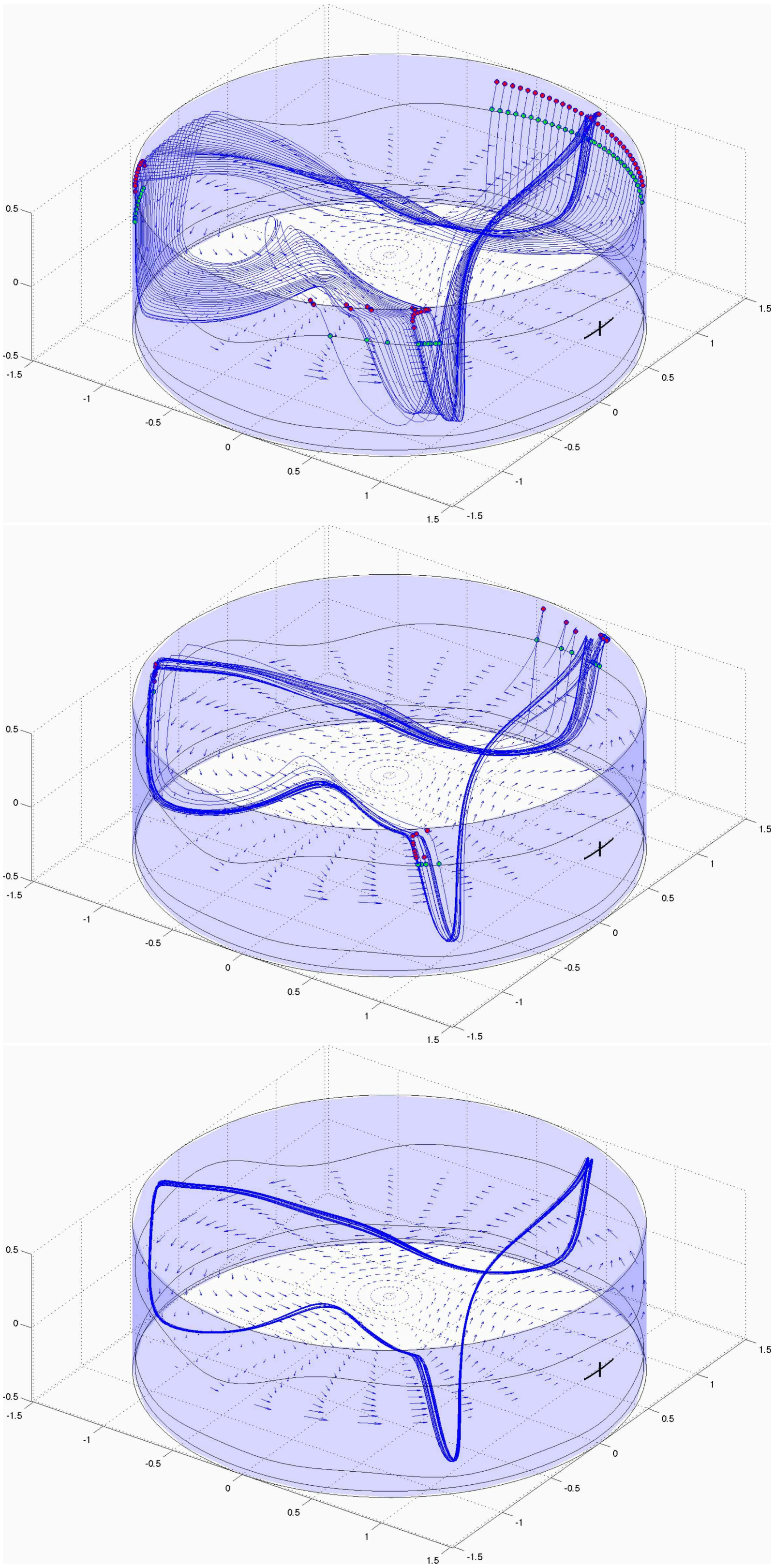

Figure 10.3: PAS development for large particles ($\mathrm{St} = 5 \cdot 10^{-5}$). Uppermost image: $t = [0, 0.35]$. Central image: $t = [0.35, 0.7]$. Lowermost image: $t = [1, 1.35]$.

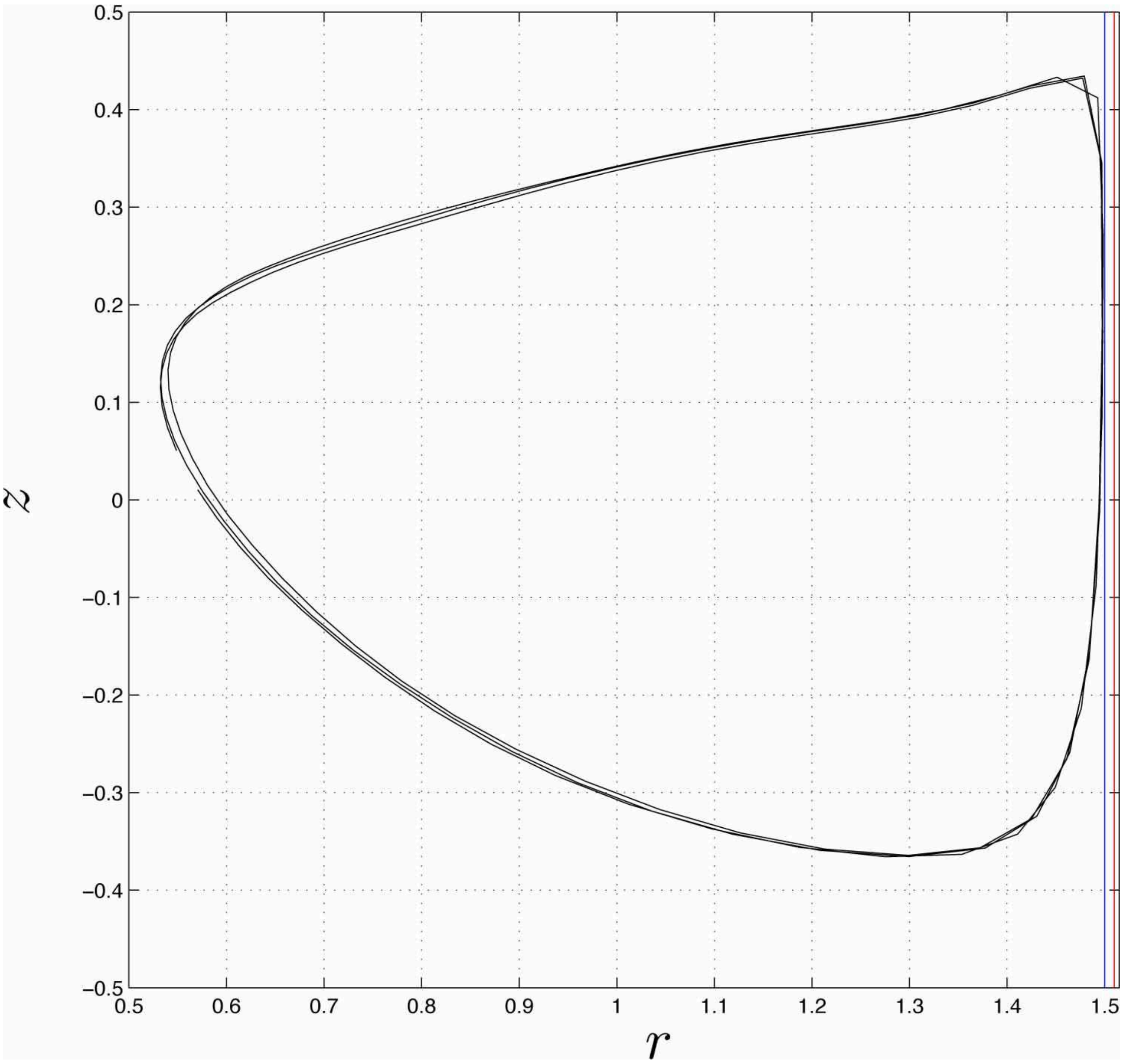

Figure 10.4: PAS-projection of the supercritical flow Re = 2600 into the $r - z-$plane. Vertical red line indicates $R^{\dagger}$ of small particle (St $= 6 \cdot 10^{-6}$), vertical blue line indicates $R^{\dagger}$ of large particle (St $= 5 \cdot 10^{-5}$).

11 Flow topology

From the previous chapters it is obvious that PAS is close to a closed streamline and that the latter is related to PAS formation. Therefore, it seems useful to search for closed streamlines of the flow in the rotating frame of reference.

11.1 Closed streamlines

To find closed streamlines, a vertical cross section of the supercritical flow introduced in chapter 8 (Re = 1800) is considered and the ODE-system

$$\dot{r}' = u'_r \quad , \quad \dot{\varphi}' = \frac{u'_\varphi}{r'} \quad , \quad \dot{z}' = u'_z \tag{11.1}$$

is solved for initial positions that cover the vertical plane sufficiently dense. The integration will be terminated if the streamline has finished the first revolution around the $z-$axis, i.e. integration is considered for $\varphi' = [0, 2\pi]$. From the initial position $x'_{\text{init}} = \{r'_0, \varphi'_0 = 0, z'_0\}$ and the final position $x'_{\text{final}} = \{r'_1, \varphi'_1 = 2\pi, z'_1\}$ the radial and axial offsets of every streamline are recorded, hence

$$\Delta r = r'_1 - r'_0 \quad , \quad \Delta z = z'_1 - z'_0 \,. \tag{11.2}$$

Closed streamlines are then found at x' where both offsets vanish simultaneously.

Figure 11.1 shows the result for the radial offset Δr (above) and the axial offset Δz (below) on a calculated mesh of 0.01×0.01. White squares indicate positions without data.[1] These positions correspond to rejected streamlines where the integration failed due to stability problems of the ODE-solver at the immediate vicinity of the liquid free surface. A subsequent spline-interpolation of both data sets closes the data gaps and determines a smoother result for the isolines where the offsets are zero. These isolines are shown in figure 11.2, black for $\Delta r = 0$ and red for $\Delta z = 0$. The underlying coloured function is the absolute value of the offset

$$\Delta = \sqrt{\Delta r^2 + \Delta z^2} \,. \tag{11.3}$$

---

[1] Numerics treats these data as NaN.

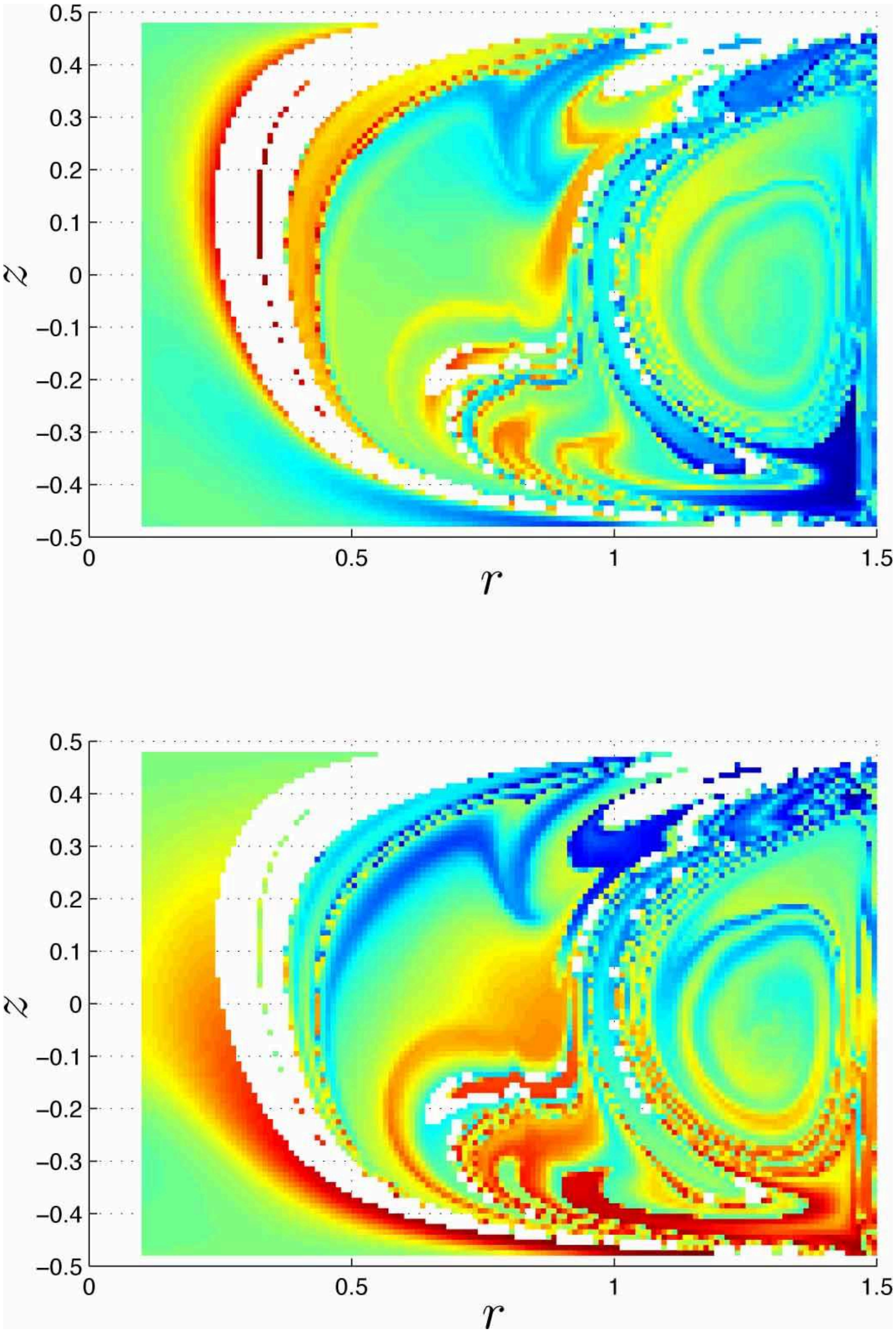

Figure 11.1: Original data of Δr (above) and Δz (below).

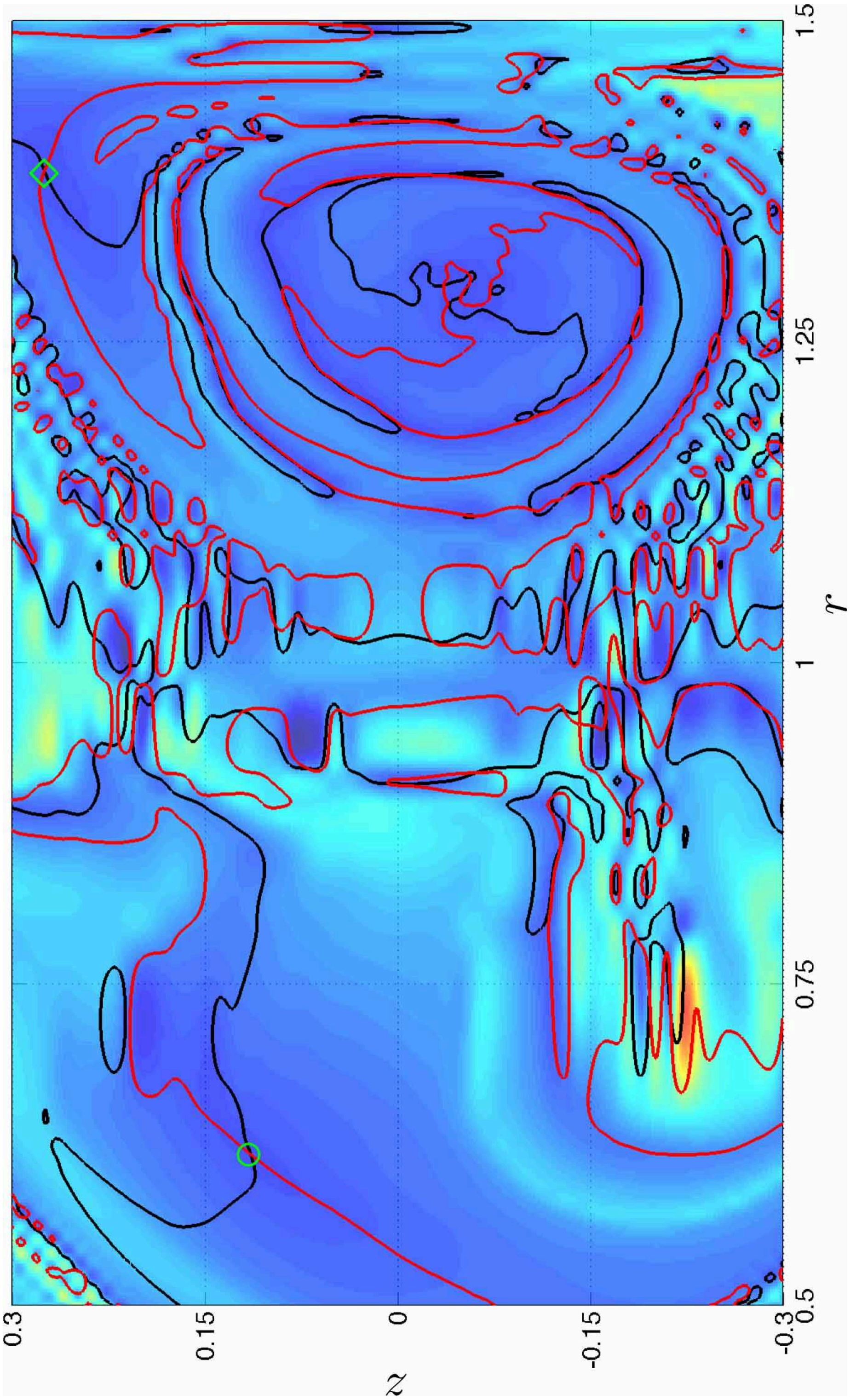

Figure 11.2: Map of interpolated data with isolines of Δr (black) and Δz (red). Coloured background is the absolute value of the offset Δ. Open green symbols indicate closed and robust streamlines within the $\mathcal{K}'-$frame. Wave numbers of the streamlines found are $m = 3$ ($\circ$) and $m = 9$ ($\diamond$).

At any intersection both offsets vanish simultaneously and indicate numerically closed streamlines. Basically the number of intersections and closed streamlines respectively seems to be enormous. The majority of all intersections lies in a noticeable *central band* and most of all points out of this band are not reproducible as closed streamlines.[2] This is caused by the rapid change of Δ in the vicinity of the intersection points. It is not clear if these pretended closed streamlines are either a result of numerically generated overshoots of the interpolation procedure or if these streamlines are very sensitive on the variation of the initial conditions.

Apart from the center band, some isolated intersection points are found and indicated in figure 11.2 by open green symbols. In contrast to the center band, these closed streamlines are robust and easy to reproduce. The robustness can be estimated from the underlying function of the absolute value Δ, which varies in its neighbourhood only linearly. The two mentioned closed and robust streamlines are shown in figure 11.3.

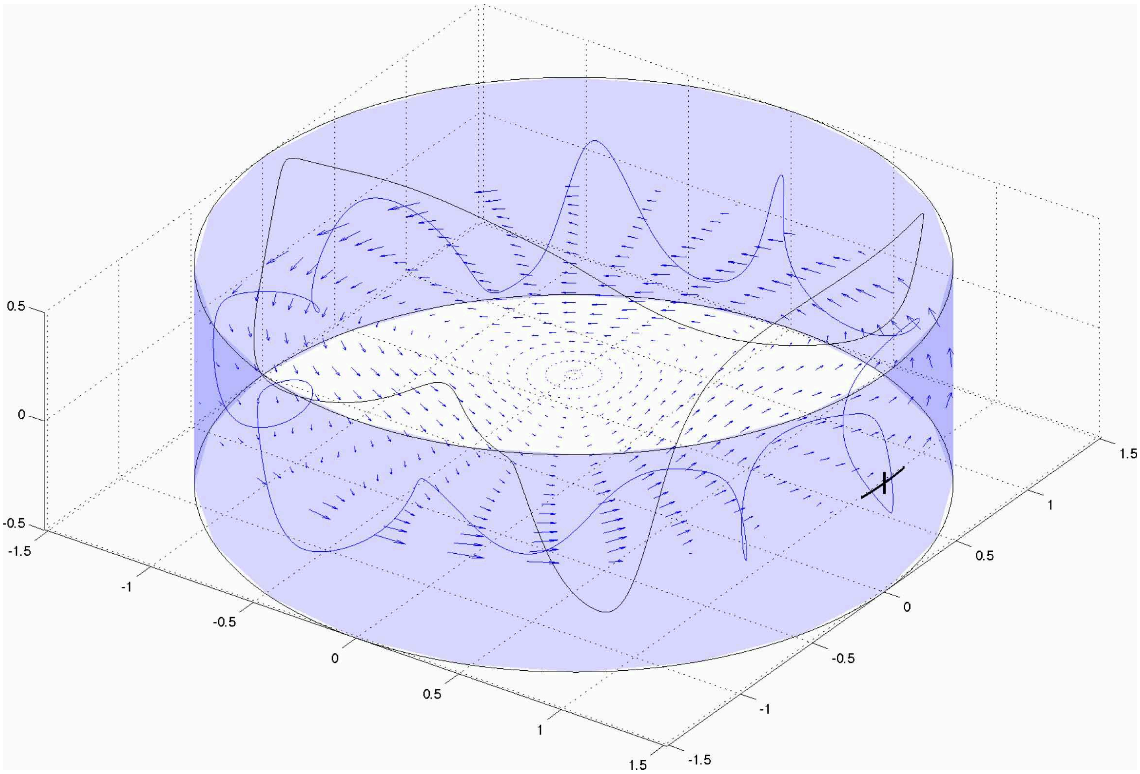

Figure 11.3: Closed and robust streamlines found as indicated in figure 11.2, SL-I-PAS with $m = 3$ (black, $\circ$); $m = 9$ (blue, $\diamond$).

---

[2] This conclusion is found by the evaluation of some sample points, not all intersections are checked.

11.2 Transfer mechanism

It is already shown that a sufficiently small, density-matched particle follows the streamline of the flow in excellent approximation. If a tracer is not initially located on the closed streamline, a transfer to this closed streamline would mean an intersection of the streamline corresponding to the initial position of the tracer and the closed streamline. Due to the steadiness (in the rotating frame) and uniqueness of the flow field, streamline intersections are impossible. Hence, a mechanism is required that allow particles to swap to other streamlines and finally to a stable trajectory which is equivalent to PAS. One candidate for a transfer process of particles from one streamline to another is the introduced finite-particle-radius effect. Therewith all particles slide along $R^\dagger$ and swap continuously from one streamline to another and obviously reach a stable configuration, namely PAS corresponding to one out of a certain number of closed streamlines.

At this point one ends up at a one-to-one analogy of PAS in subcritical and supercritical flows: PAS is the result of the interaction between finite sized particles and liquid free surface, where all particles are transferred by their sliding movement on $R^\dagger$ from one streamline to another until they reach a closed streamline. The only difference between the two cases is the number of closed streamlines. In subcritical, incompressible flows all streamlines are closed and in principle suitable for PAS. In supercritical, incompressible flows, streamlines are in general not closed (after one revolution around the $z-$axis) and only a certain number of closed and robust streamlines exist. Furthermore, if these mentioned streamlines should be relevant for PAS, they have to get very close to the liquid free surface.

The only remaining question is about the details of the transfer process, discussed below by distinguishing three cases. For this upcoming proposal onto the PAS forming mechanism one assumes that the closed streamline, called from now on C_0, is surrounded in its vicinity by an infinite number of nested closed stream tubes. The streamlines on any such closed stream tube wind around C_0 on a toroidal tube in an incommensurate fashion. This assumption is motivated by the found robustness of the closed streamlines. Unfortunately, due to numerical uncertainties, it is not possible to show these stream tubes because C_0 appears as attractor for all streamlines in its vicinity. Due to incompressibility of the fluid a real streamline attraction is forbidden and the arising effect is numerically generated only.

A closed streamline C_0 that is getting very close to the liquid free surface is considered, hence the minimum distance between C_0 and R is in the range of the particle radius a, wherefrom three cases are to distinguish as discussed below.

Tangential closed streamline

The ideal case is considered first. Hence, in full analogy to the subcritical flow, the closed streamline C_0 is exactly tangent to the contact radius $R^\dagger$. Therefrom one can follow that PAS and C_0 have to be identical. In supercritical flows this case is only possible for one single particle size.

Figure 11.4 shows a cross section through the closed streamline's tangent point Q_0. The plane is perpendicular to $\boldsymbol{u}(Q_0)$. The grey shaded area between R and $R^\dagger$ indicates the tracer's inaccessible region of the liquid bridge. The circles around Q_0 illustrate the cross sections of closed stream tubes. For simplicity the stream tubes are considered as tori. As already introduced in the foregoing chapters, PAS-particles release after their phase of sliding from the contact radius $R^\dagger$ at the release line L_1. This release point is from now on specified as P_0. Due to the identity of PAS and C_0 in the present case, the release point P_0 and the closed streamline's center Q_0 are identical.

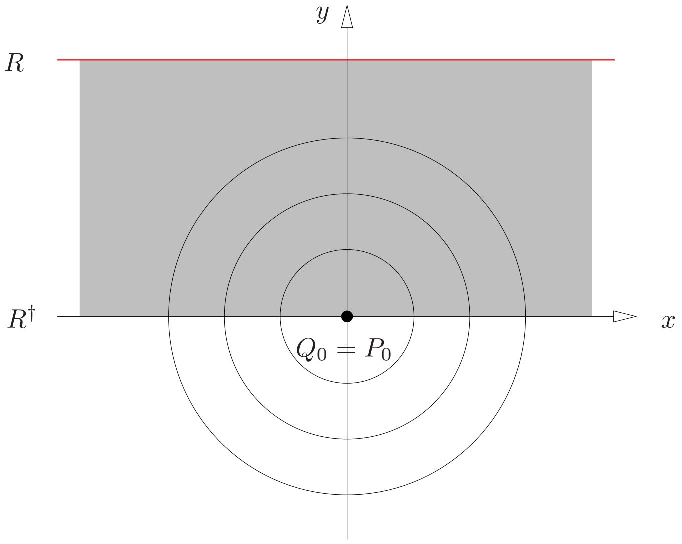

Figure 11.4: Schematic visualization of small stream tubes around the closed streamline with center Q_0. The depicted plane is a cross section through Q_0 perpendicular to $\boldsymbol{u}(Q_0)$. The release point of PAS P_0 is in this case identical to Q_0.

To understand the transfer process one assumes that all streamlines in the vicinity of the closed streamline C_0 wind around it with a constant angular rate. In other words every passive tracer that orbits around C_0 on a closed stream tube will cover an angle θ between two sequenced surface collisions. The angle θ is measured by the center Q_0 and not by the $z-$axis. Furthermore θ is unknown but for simplicity assumed to be constant.

Figure 11.5 illustrates the transfer model. If a tracer collides with the liquid free surface, it gets transferred (projected) on $R^\dagger$ ($y = 0$), slides along $R^\dagger$ until it reaches the release line (L_1) and leaves the contact radius on another closed stream tube which is now closer to Q_0 than its original stream tube. The release points are indicated in figure 11.5 as red dots. Before the tracer reaches the surface again, it winds around C_0 by covering the angle θ (blue arrow). Successive collisions of any tracer on a closed stream tube will finally lead to a transfer to the closed streamline C_0 representing PAS.

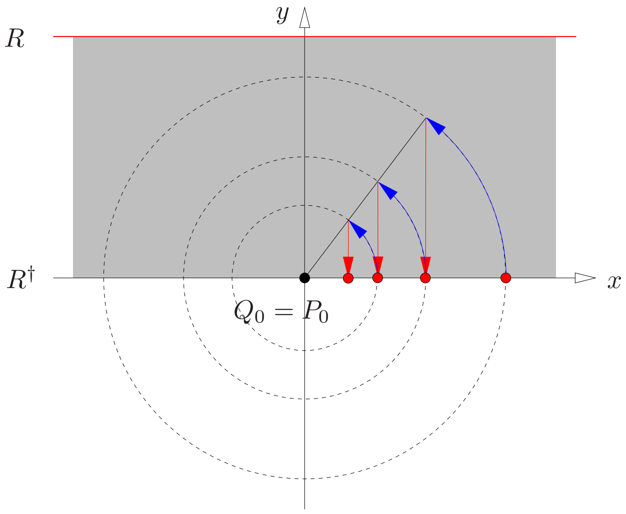

Figure 11.5: Schematic visualization of the transfer process for the tangent streamline.

Intersecting closed streamline

If the Stokes number is increased, C_0 intersects the contact radius $R^\dagger$ and an exact agreement of PAS and C_0 is no longer possible. Figure 11.6 shows the projection of both, the closed streamline C_0 (green) and the closed PAS trajectory (blue), on the unrolled cylinder surface at $R^\dagger$. The short red lines indicate the sliding movement on $R^\dagger$. The piercing points of the closed streamline through $R^\dagger$ are indicated as asterisks. One can see from the figure, that PAS winds around C_0 as already assumed above.

Figure 11.7 sketches the situation of figure 11.6 as cross section. The plane is chosen through Q_0 perpendicular to $\boldsymbol{u}(Q_0)$, where Q_0 represents the point of maximum separation b between the closed streamline C_0 and the contact radius $R^\dagger$. The PAS release point P_0 is no longer identical to Q_0. For simplicity both points, P_0 and Q_0, are considered to lie in the same plane.

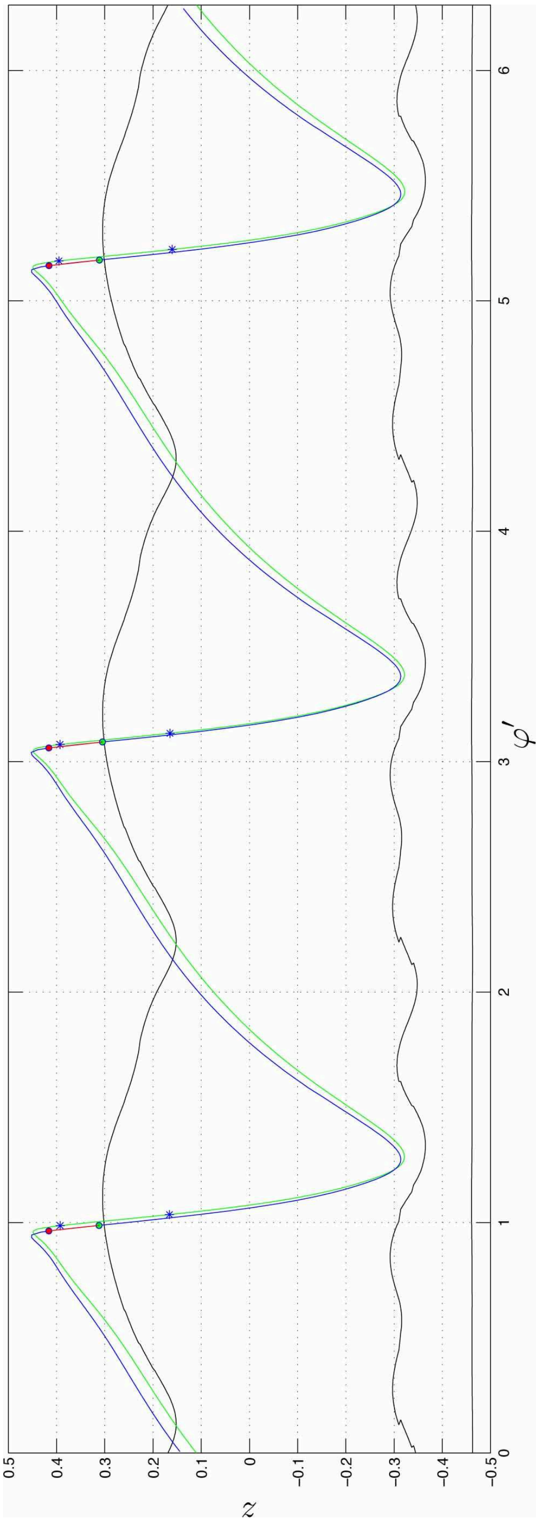

Figure 11.6: Projection of closed streamline C_0 (green) and PAS (blue) on the unrolled cylinder surface at $R^{\dagger}$. The red lines indicate the sliding movement on the contact radius, red dots are surface collisions, green dots surface releases and the black graphs are the surface release lines. The piercing points of the closed streamline are indicated as asterisks.

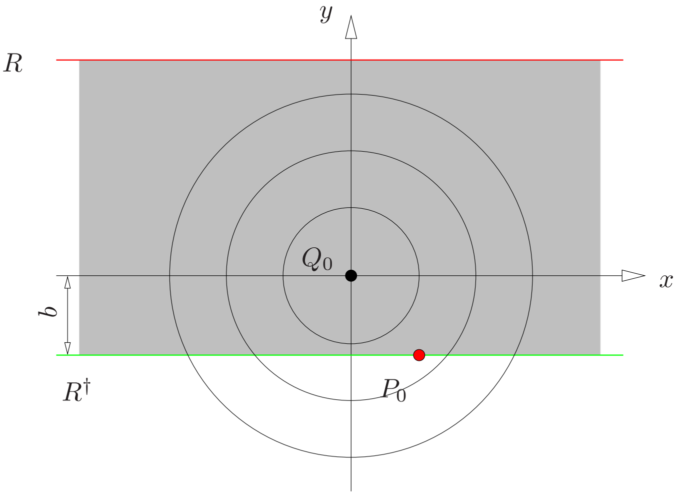

Figure 11.7: Schematic visualization of small stream tubes around the closed streamline with center Q_0. The depicted plane is a cross section through Q_0 perpendicular to $\boldsymbol{u}(Q_0)$. The distance b represents the maximum separation between C_0 and $R^\dagger$. The release point of PAS is indicated as P_0.

The application of the model from above yields the situation sketched in figure 11.8. If a collision is encountered, the particle is transferred (projected) to $y = b$ and releases from the surface at (x_n, y_n). The particle returns to the liquid free surface again by covering the angle $\varphi = 2\pi j/m$ around the $z-$axis and by covering the angle θj around the closed streamline C_0 with $j \in \mathbb{N}$. The rule

$$\begin{aligned} x_{n+1} &= x_n \cos\theta - y_n \sin\theta\,, \\ y_{n+1} &= \min\left(b, x_n \sin\theta + y_n \cos\theta\right) \end{aligned} \tag{11.4}$$

maps the coordinates from the foregoing release point (x_n, y_n) to the coordinates of the following release point (x_{n+1}, y_{n+1}).

The map (11.4) has the trivial fixed points $x_{n+1} = x_n(-1)^k$ for $\theta = k\pi, k \in \mathbb{Z}$ and the non-trivial fixed point

$$(x^*, y^*) = \left(-\frac{b}{\tan(\theta/2)}, b\right) \qquad \text{for} \qquad b \leq 0\,. \tag{11.5}$$

The coordinates (x^*, y^*) represent the stable PAS release point P_0. The map (11.4) and the convergence to the coordinates of the PAS release point P_0 (11.5), hold for the assumption of a constant angular rate ($\theta =$ const.) and an intersection of the closed streamline C_0 with the contact radius $R^\dagger$.

From this result one can clearly see that PAS formation is even possible for an intersecting closed streamline. The result is a stable, (nearly) closed trajectory, namely PAS, which orbits around the closed streamline C_0. The result of the assumed model compare well with the result of the simulation. This becomes particularly clear in figure 11.6, where PAS as closed trajectory orbits around C_0. The tangential streamline is included as limit case with $b = 0$, where PAS and C_0 are exactly identical.

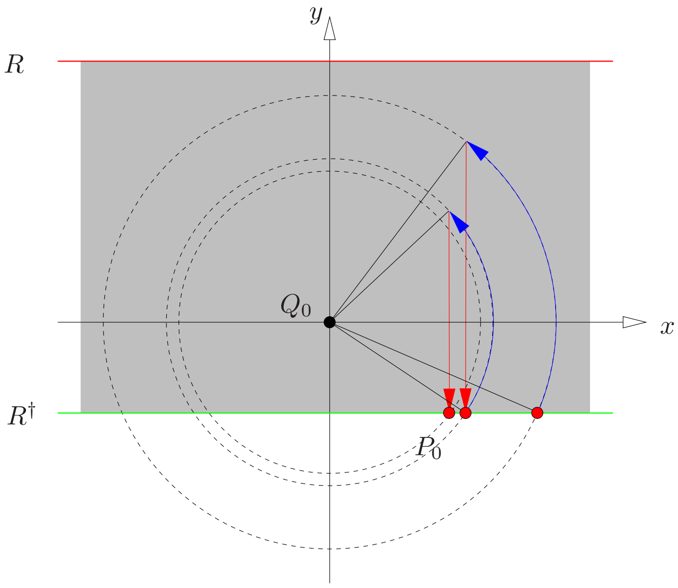

Figure 11.8: Schematic visualization of the transfer process for the intersecting closed streamline.

Non-intersecting closed streamline

The final case considers a Stokes number corresponding to a particle radius which is smaller than the minimum distance between C_0 and the liquid free surface, hence $b > 0$. The situation is sketched in figure 11.9.

The application of the introduced model is shown in figure 11.10. Particles are again transferred by surface interactions to inner stream tubes as long as the particles reach the point P_0 (see figure 11.9) corresponding to the tangent point of the tangential stream tube (red circles in figures 11.9 and 11.10). Once a particle releases from P_0, it will stay on the corresponding tangential stream tube. PAS arises in this case not as a closed trajectory but as a small stream tube enclosing the closed streamline. The proof of this case within a numerical simulation is difficult, because as mentioned in the last chapter, numerical effects lead to an attraction of all particles in the vicinity of the closed streamline.

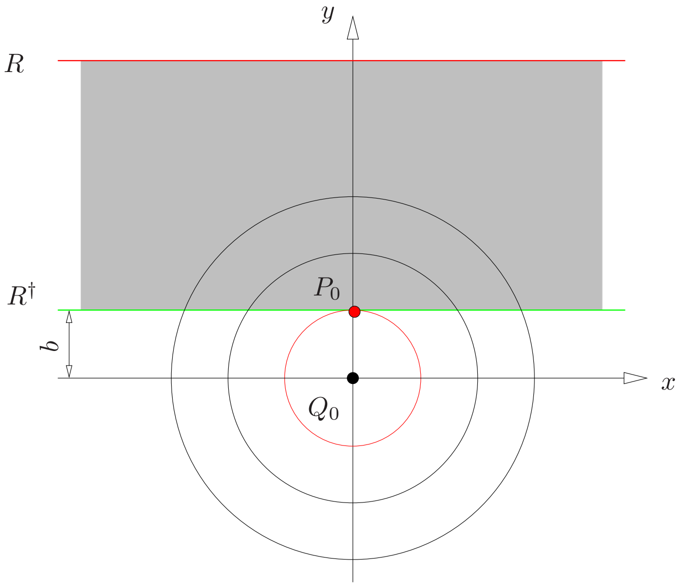

Figure 11.9: Schematic visualization of small stream tubes around the closed streamline with center Q_0. The depicted plane is a cross section through Q_0 perpendicular to $\boldsymbol{u}(Q_0)$. The distance b represents the maximum separation between C_0 and $R^\dagger$. The release point of PAS is indicated as P_0.

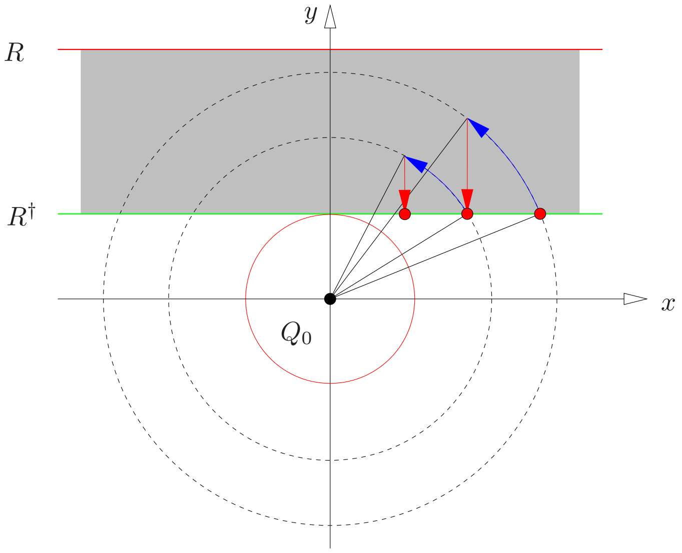

Figure 11.10: Schematic visualization of transfer process for the non-intersecting closed streamline.

12 Summary

This work has numerically studied the dynamics of small, density-matched tracers in purely thermocapillary flows (zero gravity) of a liquid bridge to clarify the formation mechanisms of so-called particle accumulation structures (PAS). The choice of zero gravity and density-matching tries to identify the pure mechanisms behind PAS formation.

The flow is determined in the Oberbeck–Boussinesq approximation with the code of Leypoldt [9] and the particle motion is integrated with a simplified version of the Maxey–Riley equation. The ODE-solver for the particle trajectories was developed by the author in MATLAB.

The assumed one-way coupling and the characteristics of the travelling hydrothermal wave allows a transformation into a rotating frame of reference where the flow is steady. This liberates from a simultaneous simulation of flow and particle motion. The particle–boundary interaction is implemented as the very basic but common partially elastic reflection model.

The primary PAS mechanism, hence the particle transfer to a single streamline, is identified for subcritical 2D–flows as particle–liquid free surface interaction caused by the particle's finite size. In subcritical flows, the collision of particle and liquid free surface is the necessary and sufficient condition for PAS development. This idea of PAS formation is then transferred to the supercritical three-dimensional flow, where the analysis shows as necessary and sufficient condition particle–liquid free surface interactions as well but now restricted to certain regions.

It turns out that particle trajectories and flow streamlines agree in excellent approximation for sufficiently small and density-matched tracers in zero gravity. This realization leads to the speculation that PAS is a representative of a closed streamline in three-dimensional supercritical flows. A basic analysis of the flow topology shows that the supercritical flow contains in fact only a certain number of robust, closed streamlines. Additionally it turns out that PAS is very close to one of these closed streamlines.

At the end PAS arises as a (nearly) closed trajectory that orbits around a closed streamline. In the limit case, PAS is identical to the closed streamline of the three-dimensional flow. The attraction of the particles to the closed streamline is modelled by sequenced particle–liquid free surface interactions.

A Nomenclature

A.1 Basic notation

Frames of reference

The inertial frame of reference, which is the laboratory frame, is denoted by $\mathcal{K}$ and the rotating frame of reference of the hydrothermal wave is identified as $\mathcal{K}'$. Other frames are indicated double primed and so forth. All quantities measured in a frame are primed like the respective frame.

Kinematic quantities

The velocity field of the flow is indicated by $\boldsymbol{u}(\boldsymbol{x}, t)$ whereas the space coordinate for the flow is throughout $\boldsymbol{x}$. The notation of the components of the field is chosen as u_x, u_y, u_z in cartesian coordinates and as u_r, u_φ, u_z in cylindrical coordinates.

The particle position is exclusively identified by $\boldsymbol{y}(t)$ and its velocity by $\dot{\boldsymbol{y}}(t)$.

The acceleration of gravity is indicated by g and points into the direction $\boldsymbol{e}_g$ which is typically $-\boldsymbol{e}_z$.

Indication of dimensional quantities

For a consistent notation, all quantities arising both, dimensional and dimensionless, should be identified clearly either to be dimensional or dimensionless. Typically this is done by using a superscripted asterisk for the dimensional quantities, but in most sections of the present work, the asterisk is set aside for well arranged, not overloaded characters. At the beginning of all concerned sections, a short note will clarify the treatment of the asterisk.

Laplace operator

For a clear determination from the greek capital delta, the Laplace operator is written throughout as ∇^2.

A.2 Dimensional parameters

Table A.1: List of all dimensional material and geometrical parameters used in this work. If not mentioned otherwise, the parameters are measured at the mean temperature T_0 and are set to constants.

Liquid Bridge	
d	height
R	radius
Fluid	
ρ_f	density as function of temperature $\rho_\mathrm{f} = \rho_\mathrm{f}(T^*)$
σ	surface tension as function of temperature $\sigma = \sigma(T^*)$
ρ_0	density at the mean temperature $\rho_0 = \rho_\mathrm{f}(T_0)$
σ_0	surface tension at the mean temperature $\sigma_0 = \sigma(T_0)$
μ	dynamic viscosity
ν	kinematic viscosity
λ	thermal conductivity
c_p	specific heat capacity (at constant pressure)
κ	thermal diffusivity
β	isobaric thermal expansion coefficient
γ	surface tension coefficient
h	heat transfer coefficient
$\mathbf{S}, S_{ij}$	stress tensor
$\mathbf{D}, D_{ij}$	strain rate tensor
Particle	
a	radius
m_p	mass
ρ_p	density

A.3 Scales

The common scaling method for the kinematic quantities is shown below and is done with some representative values for length L_0, velocity U_0 and time t_0. The dimensionless kinematic quantities are found with the scales

$$x_i = \frac{x_i^*}{L_0} \qquad , \qquad u_i = \frac{u_i^*}{U_0} \qquad , \qquad t = \frac{t^*}{t_0} \,. \tag{A.1}$$

According to the geometry of the liquid bridge, the scaling parameters are

$$L_0 = d \qquad , \qquad U_0 = \frac{\nu}{d} \qquad , \qquad t_0 = \frac{L_0}{U_0} = \frac{d^2}{\nu} \,. \tag{A.2}$$

The chosen time scale t_0 is the **viscous diffusion time**.

The scaling procedures for pressure p^* and temperature difference $(T^* - T_0)$ are

$$p = \frac{p^*}{P_0} \qquad , \qquad T = \frac{T^* - T_0}{\Delta T} \tag{A.3}$$

with the mean temperature

$$T_0 = \frac{T_{\text{top}} + T_{\text{bot}}}{2} \tag{A.4}$$

deduced from the temperatures of the top and bottom disks, which are indicated as T_{top} and T_{bot} respectively.

The reference pressure P_0 and the reference temperature difference ΔT act as the scaling parameters and read

$$P_0 = \rho_0 \, U_0^2 = \frac{\rho_0 \nu^2}{d^2} \qquad , \qquad \Delta T = T_{\text{top}} - T_{\text{bot}} \,. \tag{A.5}$$

The scaling procedure for the most important terms of the Navier-Stokes equations yield

$$\frac{\mathrm{d}u_i^*}{\mathrm{d}t^*} = \frac{U_0}{t_0}\frac{\mathrm{d}u_i}{\mathrm{d}t} = \frac{\nu^2}{d^3}\frac{\mathrm{d}\boldsymbol{u}}{\mathrm{d}t} \,, \tag{A.6}$$

$$-\frac{1}{\rho_0}\frac{\partial p^*}{\partial x_i^*} = -\frac{1}{\rho_0}\frac{P_0}{L_0}\frac{\partial p}{\partial x_i} = -\frac{\nu^2}{d^3}\nabla p \,, \tag{A.7}$$

$$\nu\frac{\partial^2 u_i^*}{\partial x_j^* \partial x_j^*} = \nu\frac{U_0}{L_0^2}\frac{\partial^2 u_i}{\partial x_j \partial x_j} = \frac{\nu^2}{d^3}\nabla^2 \boldsymbol{u} \,, \tag{A.8}$$

$$\beta g (T^* - T_0) = \beta g \Delta T \, T \,. \tag{A.9}$$

A.4 Dimensionless parameters

Flow and liquid bridge

The fundamental geometrical parameter is the aspect ratio of the liquid bridge

$$\Gamma = \frac{d}{R} \, . \tag{A.10}$$

The parameter space of the thermocapillary flow inside the liquid bridge is five-dimensional and characterized by the mentioned aspect ratio Γ, thermocapillary Reynolds number, Prandtl, Grashof and Biot numbers

$$\mathrm{Re} = \frac{\gamma d}{\rho_0 \nu^2} \Delta T \quad , \quad \mathrm{Pr} = \frac{\nu}{\kappa} \quad , \quad \mathrm{Gr} = \frac{\beta g d^3}{\nu^2} \Delta T \quad , \quad \mathrm{Bi} = \frac{hd}{\lambda} \, . \tag{A.11}$$

Another very important parameter for the characterization of the flow is the Marangoni number

$$\mathrm{Ma} = \frac{\gamma d}{\rho_0 \nu \kappa} \Delta T = \mathrm{Re} \, \mathrm{Pr} \, . \tag{A.12}$$

as product of thermocapillary Reynolds number and Prandtl number.

Due to the assumption of a non deformed free fluid surface, one needs to achieve vanishingly small Bond and Capillary numbers

$$\mathrm{Bo} = \frac{\rho_0 g d^2}{\sigma_0} \ll 1 \quad , \quad \mathrm{Ca} = \frac{\gamma \Delta T}{\sigma_0} \ll 1 \, . \tag{A.13}$$

These two parameters are preconditions and therefore excluded from the fluid parameter space.

Particle

The parameter space of the particle is three-dimensional and defined by the density ratio ϱ, Stokes and Froude numbers

$$\varrho = \frac{\rho_\mathrm{p}}{\rho_0} \quad , \quad \mathrm{St} = \frac{2a^2}{9d^2} \quad , \quad \mathrm{Fr} = \frac{\nu}{\sqrt{gd^3}} \, . \tag{A.14}$$

A vanishingly small particle Reynolds number $\mathrm{Re}_\mathrm{p} \ll 1$ is a precondition for the particle, such that the inclusion of this value into the parameter space is not necessary.

B Fundamentals

B.1 Cylindrical coordinates

Domain of definition:

$$r \geq 0 \qquad , \qquad 0 \leq \varphi < 2\pi \qquad , \qquad -\infty \leq z \leq \infty \tag{B.1}$$

An arbitrary vector $\boldsymbol{u}$ in cartesian and cylindrical notation writes as

$$\begin{aligned} \boldsymbol{u} &= u_x(x,y,z)\boldsymbol{e}_x + u_y(x,y,z)\boldsymbol{e}_y + u_z(x,y,z)\boldsymbol{e}_z = && \text{(B.2)} \\ &= u_r(r,\varphi,z)\boldsymbol{e}_r + u_\varphi(r,\varphi,z)\boldsymbol{e}_\varphi + u_z(r,\varphi,z)\boldsymbol{e}_z && \text{(B.3)} \end{aligned}$$

with the cylindrical unit vectors

$$\boldsymbol{e}_r = \begin{pmatrix} \cos\varphi \\ \sin\varphi \\ 0 \end{pmatrix} \quad , \quad \boldsymbol{e}_\varphi = \begin{pmatrix} -\sin\varphi \\ \cos\varphi \\ 0 \end{pmatrix} \quad , \quad \boldsymbol{e}_z = \begin{pmatrix} 0 \\ 0 \\ 1 \end{pmatrix} . \tag{B.4}$$

Position vector

The position vector $\boldsymbol{y}$, written in cylindrical coordinates with cartesian and cylindrical unit vectors respectively, writes as

$$\boldsymbol{y} = \begin{pmatrix} r\cos\varphi \\ r\sin\varphi \\ z \end{pmatrix} = r\boldsymbol{e}_r + z\boldsymbol{e}_z . \tag{B.5}$$

The time derivatives up to the order of two of the position vector are

$$\begin{aligned} \boldsymbol{y} &= r\boldsymbol{e}_r + z\boldsymbol{e}_z && \text{(B.6)} \\ \dot{\boldsymbol{y}} &= \dot{r}\boldsymbol{e}_r + r\dot{\varphi}\boldsymbol{e}_\varphi + \dot{z}\boldsymbol{e}_z && \text{(B.7)} \\ \ddot{\boldsymbol{y}} &= (\ddot{r} - r\dot{\varphi}^2)\boldsymbol{e}_r + (2\dot{r}\dot{\varphi} + r\ddot{\varphi})\boldsymbol{e}_\varphi + \ddot{z}\boldsymbol{e}_z . && \text{(B.8)} \end{aligned}$$

Vector transformation

The transformation of an arbitrary vector $\boldsymbol{u}$ from cylindrical notation (B.3) to cartesian notation (B.2) is done by the matrix operation

$$\begin{pmatrix} u_x \\ u_y \\ u_z \end{pmatrix} = \begin{pmatrix} \cos\varphi & -\sin\varphi & 0 \\ \sin\varphi & \cos\varphi & 0 \\ 0 & 0 & 1 \end{pmatrix} \cdot \begin{pmatrix} u_r \\ u_\varphi \\ u_z \end{pmatrix} . \tag{B.9}$$

with the transformation matrix $\mathbf{A}$. The reverse transformation is done with the inverse transformation matrix, which is in this case simply the transposed one, i.e. $\mathbf{A}^{-1} = \mathbf{A}^{\mathrm{T}}$.

Nabla operations

With the nabla operator in cylindrical coordinates

$$\nabla = \boldsymbol{e}_r \partial_r + \frac{\boldsymbol{e}_\varphi}{r} \partial_\varphi + \boldsymbol{e}_z \partial_z \tag{B.10}$$

and the spatial derivatives

$$\partial_\varphi \boldsymbol{e}_r = \boldsymbol{e}_\varphi \qquad , \qquad \partial_\varphi \boldsymbol{e}_\varphi = -\boldsymbol{e}_r \tag{B.11}$$

one can understand the following nabla operations denoted in cylindrical coordinates.

1. Nabla operations on a scalar function $f = f(r, \varphi, z)$
   a) **Gradient**

$$\nabla f = \boldsymbol{e}_r \partial_r f + \frac{\boldsymbol{e}_\varphi}{r} \partial_\varphi f + \boldsymbol{e}_z \partial_z f \tag{B.12}$$

$$\tag{B.13}$$

   b) **Scalar Laplace operation**

$$\nabla^2 f = \left(\frac{1}{r} + \partial_r \right) \partial_r f + \frac{1}{r^2} \partial_\varphi^2 f + \partial_z^2 f \tag{B.14}$$

2. Nabla operations on a vector function of (B.3)
   a) **Divergence**

$$\nabla \cdot \boldsymbol{u} = \left(\frac{1}{r} + \partial_r \right) u_r + \frac{1}{r} \partial_\varphi u_\varphi + \partial_z u_z \tag{B.15}$$

b) **Vectorial Laplace operation**

$$\begin{aligned}\nabla^2\boldsymbol{u} = \boldsymbol{e}_r\left(\nabla^2 u_r - \frac{u_r}{r^2} - \frac{2}{r^2}\partial_\varphi u_\varphi\right) + \\ + \boldsymbol{e}_\varphi\left(\nabla^2 u_\varphi - \frac{u_\varphi}{r^2} + \frac{2}{r^2}\partial_\varphi u_r\right) + \\ + \boldsymbol{e}_z\nabla^2 u_z\end{aligned} \tag{B.16}$$

c) **Convective derivative**

$$\begin{aligned}(\boldsymbol{u}\cdot\nabla)\boldsymbol{u} &= \left(u_r\partial_r + \frac{u_\varphi}{r}\partial_\varphi + u_z\partial_z\right)\boldsymbol{u} = \\ &= \boldsymbol{e}_r\left[\left(u_r\partial_r + \frac{u_\varphi}{r}\partial_\varphi + u_z\partial_z\right)u_r - \frac{u_\varphi^2}{r}\right] + \\ &\quad + \boldsymbol{e}_\varphi\left[\left(u_r\partial_r + \frac{u_\varphi}{r}\partial_\varphi + u_z\partial_z\right)u_\varphi + \frac{u_r u_\varphi}{r}\right] + \\ &\quad + \boldsymbol{e}_z\left(u_r\partial_r + \frac{u_\varphi}{r}\partial_\varphi + u_z\partial_z\right)u_z\end{aligned} \tag{B.17}$$

3. Tensor operation

a) **Strain rate tensor**

$$\begin{aligned}\mathbf{D} = \frac{1}{2}\left(\nabla\boldsymbol{u} + (\nabla\boldsymbol{u})^{\mathrm{T}}\right) &= \boldsymbol{e}_r\boldsymbol{e}_r\partial_r u_r + \frac{\boldsymbol{e}_\varphi\boldsymbol{e}_\varphi}{r}\left(\partial_\varphi u_\varphi + u_r\right) + \boldsymbol{e}_z\boldsymbol{e}_z\partial_z u_z + \\ &\quad + \frac{1}{2}\left(\boldsymbol{e}_r\boldsymbol{e}_\varphi + \boldsymbol{e}_\varphi\boldsymbol{e}_r\right)\left(\partial_r u_\varphi + \frac{\partial_\varphi u_r}{r} - \frac{u_\varphi}{r}\right) + \\ &\quad + \frac{1}{2}\left(\boldsymbol{e}_r\boldsymbol{e}_z + \boldsymbol{e}_z\boldsymbol{e}_r\right)\left(\partial_r u_z + \partial_z u_r\right) + \\ &\quad + \frac{1}{2}\left(\boldsymbol{e}_\varphi\boldsymbol{e}_z + \boldsymbol{e}_z\boldsymbol{e}_\varphi\right)\left(\frac{\partial_\varphi u_z}{r} + \partial_z u_\varphi\right)\end{aligned} \tag{B.18}$$

B.2 Equation of motion in a rotating frame of reference

An inertial frame of reference $\mathcal{K}$ and a rotating and hence non inertial frame of reference $\mathcal{K}'$ is considered. The rotating $\mathcal{K}'-$frame rotates with the constant angular velocity

$$\boldsymbol{\Omega} = \Omega \boldsymbol{e}_z = \Omega \boldsymbol{e}'_z = \text{const.} \tag{B.19}$$

The position vector $\boldsymbol{y}$ denoted in these two frames is

$$\boldsymbol{y} = y_i \boldsymbol{e}_i \;\; = \;\; y'_i \boldsymbol{e}'_i = \boldsymbol{y}' \,. \tag{B.20}$$

For an observer in $\mathcal{K}$, the unit vectors $\boldsymbol{e}'_i$ of frame $\mathcal{K}'$ are time dependent, such that one computes the time derivative of those as

$$\frac{\mathrm{d}\boldsymbol{e}'_i}{\mathrm{d}t} = \boldsymbol{\Omega} \times \boldsymbol{e}'_i \,. \tag{B.21}$$

From (B.21) one finds the relations for the velocities and accelerations between the two frames of reference

$$\dot{\boldsymbol{y}} \;\; = \;\; \dot{\boldsymbol{y}}' + \boldsymbol{\Omega} \times \boldsymbol{y}' \,, \tag{B.22}$$

$$\ddot{\boldsymbol{y}} \;\; = \;\; \ddot{\boldsymbol{y}}' + 2\,\boldsymbol{\Omega} \times \dot{\boldsymbol{y}}' + \boldsymbol{\Omega} \times (\boldsymbol{\Omega} \times \boldsymbol{y}') \,. \tag{B.23}$$

The equation of motion for a particle of mass m, observed in the $\mathcal{K}$-frame, can be easily written down with the fundamental law of Newton

$$m\ddot{\boldsymbol{y}} = \boldsymbol{F} \,. \tag{B.24}$$

For the particle observation in $\mathcal{K}'$, the equation of motion has to get modified by inserting (B.23) into (B.24)

$$m\ddot{\boldsymbol{y}}' + 2m\,\boldsymbol{\Omega} \times \dot{\boldsymbol{y}}' + m\,\boldsymbol{\Omega} \times (\boldsymbol{\Omega} \times \boldsymbol{y}') = m\ddot{\boldsymbol{y}} \,. \tag{B.25}$$

The two arising terms represent Coriolis force and centrifugal force.

For the rotating frame of reference $\mathcal{K}'$ one finally finds

$$\boxed{\ddot{\boldsymbol{y}}' = \ddot{\boldsymbol{y}} - 2\,\boldsymbol{\Omega} \times \dot{\boldsymbol{y}}' - \boldsymbol{\Omega} \times \big(\boldsymbol{\Omega} \times \boldsymbol{y}'\big) \,.} \tag{B.26}$$

B.3 Substantive derivative in a rotating frame of reference

The substantive derivative for the velocity field $\boldsymbol{u} = \boldsymbol{u}(\boldsymbol{x}, t)$ given in the inertial frame of reference $\mathcal{K}$ reads as

$$\frac{\mathrm{D}\boldsymbol{u}}{\mathrm{D}t} = \frac{\partial \boldsymbol{u}}{\partial t} + \boldsymbol{u} \cdot \nabla \boldsymbol{u}\,. \tag{B.27}$$

With the field transformation

$$\boldsymbol{u} = \boldsymbol{u}' + \boldsymbol{\Omega} \times \boldsymbol{x}' \tag{B.28}$$

the convective derivative in terms of the $\mathcal{K}'-$field $\boldsymbol{u}' = \boldsymbol{u}'(\boldsymbol{x}')$ simply follows by using the substitution of (B.28), hence

$$\begin{aligned} \boldsymbol{u} \cdot \nabla \boldsymbol{u} &= (\boldsymbol{u}' + \boldsymbol{\Omega} \times \boldsymbol{x}') \cdot \nabla' (\boldsymbol{u}' + \boldsymbol{\Omega} \times \boldsymbol{x}') = \\ &= \boldsymbol{u}' \cdot \nabla' \boldsymbol{u}' + (\boldsymbol{\Omega} \times \boldsymbol{x}') \cdot \nabla' \boldsymbol{u}' + \boldsymbol{u}' \cdot \nabla' (\boldsymbol{\Omega} \times \boldsymbol{x}') + (\boldsymbol{\Omega} \times \boldsymbol{x}') \cdot \nabla (\boldsymbol{\Omega} \times \boldsymbol{x}') \end{aligned} \tag{B.29}$$

and with the identities

$$\begin{aligned} \boldsymbol{u}' \cdot \nabla' (\boldsymbol{\Omega} \times \boldsymbol{x}') &= \boldsymbol{\Omega} \times \boldsymbol{u}' \\ (\boldsymbol{\Omega} \times \boldsymbol{x}') \cdot \nabla (\boldsymbol{\Omega} \times \boldsymbol{x}') &= \boldsymbol{\Omega} \times (\boldsymbol{\Omega} \times \boldsymbol{x}') \end{aligned} \tag{B.30}$$

the convective derivative in terms of $\boldsymbol{u}'$ writes as

$$\boldsymbol{u} \cdot \nabla \boldsymbol{u} = \boldsymbol{u}' \cdot \nabla' \boldsymbol{u}' + (\boldsymbol{\Omega} \times \boldsymbol{x}') \cdot \nabla' \boldsymbol{u}' + \boldsymbol{\Omega} \times \boldsymbol{u}' + \boldsymbol{\Omega} \times (\boldsymbol{\Omega} \times \boldsymbol{x}')\,. \tag{B.31}$$

The evaluation of the local derivative

$$\frac{\partial \boldsymbol{u}}{\partial t} = \frac{\partial}{\partial t} (\boldsymbol{u}' + \boldsymbol{\Omega} \times \boldsymbol{x}') \tag{B.32}$$

is more delicate, because one has to keep in mind that the local derivative has to be carried out for a fixed position in the $\mathcal{K}-$frame (for $\boldsymbol{x} = \text{const.}$), hence

$$\frac{\partial}{\partial t} (\boldsymbol{\Omega} \times \boldsymbol{x}' + \boldsymbol{u}') = \boldsymbol{\Omega} \times \cancelto{0}{\frac{\partial \boldsymbol{x}'}{\partial t}} + \left. \frac{\partial \boldsymbol{u}'}{\partial t} \right|_{\boldsymbol{x}=\text{const.}} \tag{B.33}$$

For the outstanding term

$$\left. \frac{\partial \boldsymbol{u}'}{\partial t} \right|_{\boldsymbol{x}=\text{const.}} = \frac{\partial}{\partial t} u_i'(\boldsymbol{x}') \boldsymbol{e}_i'(t) = u_i' \frac{\partial \boldsymbol{e}_i'}{\partial t} + \left. \boldsymbol{e}_i' \frac{\partial u_i'}{\partial t} \right|_{\boldsymbol{x}=\text{const.}} \tag{B.34}$$

firstly one has to account for the explicit time dependency of the unit vectors and finds

$$u_i' \frac{\partial \boldsymbol{e}_i'}{\partial t} = u_i' \boldsymbol{\Omega} \times \boldsymbol{e}_i' = \boldsymbol{\Omega} \times \boldsymbol{u}'\,. \tag{B.35}$$

The local derivative of a scalar field $\phi = \phi(\boldsymbol{x}, t)$ given in the $\mathcal{K}-$frame is connected to the local derivative of the transformed field $\phi' = \phi(\boldsymbol{x}', t)$ given a rotating $\mathcal{K}'-$frame by the transformation rule

$$\frac{\partial \phi(\boldsymbol{x}, t)}{\partial t} = \frac{\partial \phi'}{\partial t} - (\boldsymbol{\Omega} \times \boldsymbol{x}') \cdot \nabla' \phi' = \left. \frac{\partial \phi(\boldsymbol{x}', t)}{\partial t} \right|_{\boldsymbol{x}=\text{const.}} \tag{B.36}$$

The application of the transformation rule (B.36) to the components u_i' in (B.34) together with (B.35) yields

$$\frac{\partial \boldsymbol{u}}{\partial t} = \boldsymbol{\Omega} \times \boldsymbol{u}' + \boldsymbol{e}_i' \left(\frac{\partial u_i'}{\partial t} - (\boldsymbol{\Omega} \times \boldsymbol{x}') \cdot \nabla' u_i' \right) \tag{B.37}$$

and with the explicit time independent velocity components $u_i' = u_i'(\boldsymbol{x}')$, the local derivative in terms of $\boldsymbol{u}'$ reduces to

$$\frac{\partial \boldsymbol{u}}{\partial t} = \boldsymbol{\Omega} \times \boldsymbol{u}' - (\boldsymbol{\Omega} \times \boldsymbol{x}') \cdot \nabla' \boldsymbol{u}' \,. \tag{B.38}$$

The final substantive derivative in terms of the $\mathcal{K}'-$field $\boldsymbol{u}' = \boldsymbol{u}'(\boldsymbol{x}')$ follows as

$$\boxed{\frac{\mathrm{D}\boldsymbol{u}}{\mathrm{D}t} = \boldsymbol{u}' \cdot \nabla' \boldsymbol{u}' + 2\boldsymbol{\Omega} \times \boldsymbol{u}' + \boldsymbol{\Omega} \times (\boldsymbol{\Omega} \times \boldsymbol{x}') \,.} \tag{B.39}$$

An alternative formulation of the substantive derivative is found by using the rotating coordinates notation of the $\mathcal{K}-$field $\boldsymbol{u} = \boldsymbol{u}(\boldsymbol{x}')$, hence

$$\boxed{\frac{\mathrm{D}\boldsymbol{u}}{\mathrm{D}t} = \big(\boldsymbol{u} - \boldsymbol{\Omega} \times \boldsymbol{x}'\big) \cdot \nabla' \boldsymbol{u} + \boldsymbol{\Omega} \times \boldsymbol{u} \,.} \tag{B.40}$$

By using the field transformation $\boldsymbol{u} = \boldsymbol{u}' + \boldsymbol{\Omega} \times \boldsymbol{x}'$ in (B.40) and the identities of (B.30), one will end up at (B.39) again.

B.4 Velocity gradient, strain rate tensor and stress tensor

Analysis of the fluid motion

A first-order Taylor series approximation of the velocity component u_j at $\boldsymbol{x} + \mathrm{d}\boldsymbol{x}$ yields

$$u_j(\boldsymbol{x} + \mathrm{d}\boldsymbol{x}) \;=\; u_j(\boldsymbol{x}) + \frac{\partial u_j}{\partial x_i}\mathrm{d}x_i \tag{B.41}$$

The velocity gradient of $\boldsymbol{u}$

$$L_{ij} = \frac{\partial u_j}{\partial x_i} = \partial_i u_j = \operatorname{grad}\boldsymbol{u} = \nabla\boldsymbol{u} \tag{B.42}$$

can be split into the antisymmetric and symmetric fractions

$$L_{ij} = \partial_i u_j = \underbrace{\frac{1}{2}\left(\frac{\partial u_j}{\partial x_i} - \frac{\partial u_i}{\partial x_j}\right)}_{\underbrace{L_{[ij]}}_{\text{antisymm. fraction}}} + \underbrace{\frac{1}{2}\left(\frac{\partial u_j}{\partial x_i} + \frac{\partial u_i}{\partial x_j}\right)}_{\underbrace{L_{(ij)} \;=\; D_{ij}}_{\text{symm. fraction}}}. \tag{B.43}$$

With this decomposition, one finds the Taylor series expansion (B.41) as

$$u_j(\boldsymbol{x} + \mathrm{d}\boldsymbol{x}\,) \;=\; \underbrace{u_j(\boldsymbol{x}\,)}_{a} \;+\; \underbrace{L_{[ij]}\,\mathrm{d}x_i}_{b} \;+\; \underbrace{D_{ij}\,\mathrm{d}x_i}_{c} \tag{B.44}$$

and end up at Helmholtz' interpretation of the fluid motion:

a represents a simple translation.

b represents the rigid body rotation

$$L_{[ij]}\,\mathrm{d}x_i = (\boldsymbol{\omega} \times \mathrm{d}\boldsymbol{x})_j \tag{B.45}$$

with the angular velocity

$$\boldsymbol{\omega} = \frac{1}{2}\nabla \times \boldsymbol{u}\,. \tag{B.46}$$

b represents the strain of the fluid, specified by the strain-rate tensor

$$D_{ij} = \frac{1}{2}\left(\frac{\partial u_j}{\partial x_i} + \frac{\partial u_i}{\partial x_j}\right) = \frac{1}{2}\left(\nabla\boldsymbol{u} + (\nabla\boldsymbol{u})^{\mathrm{T}}\right) = \mathbf{D}\,. \tag{B.47}$$

This tensor is responsible for the viscous forces and therefore connected to the viscous stress tensor τ_{ij}, as one can study in the next paragraph.

From the strain rate tensor to the stress tensor

The stress tensor S_{ij} denoted with the hydrostatic pressure p and the viscous stress tensor τ_{ij} reads

$$S_{ij} = -p\,\delta_{ij} + \tau_{ij}\,. \tag{B.48}$$

In case of a fluid at rest, all components of the viscous stress tensor vanish and only the hydrostatic pressure remains. With some more analysis, one finds that the viscous stress tensor and the strain rate tensor are connected. For a Newtonian fluid this connection is the linear relation [23]

$$\tau_{ij} = 2\mu D_{ij} + \lambda(\partial_k u_k)\delta_{ij} \tag{B.49}$$

with the dynamic viscosity μ and the interim viscosity coefficient λ. Introducing the bulk viscosity or also referred to as second viscosity

$$\zeta = \lambda + \frac{2}{3}\mu \tag{B.50}$$

the full stress tensor of equation (B.48) together with (B.49) gets to

$$S_{ij} = -p\,\delta_{ij} + \mu\left(2D_{ij} - \frac{2}{3}(\partial_k u_k)\delta_{ij}\right) + \zeta(\partial_k u_k)\delta_{ij}\,. \tag{B.51}$$

In the important case of an incompressible fluid, the continuity equation $\partial_k u_k = \nabla\cdot\boldsymbol{u} = 0$ reduces the stress tensor to

$$\boxed{S_{ij} = -p\,\delta_{ij} + 2\mu D_{ij} = -p\,\mathbf{I} + 2\mu\mathbf{D} = \mathbf{S}} \tag{B.52}$$

where the coordinate-free notation uses the identity matrix $\mathbf{I}$.

Stress balance at an interface

Considering an interface of two immiscible fluids, like liquid (l) and gas (g), the trivial static force balance is in case of a flat surface simply $p^{(\mathrm{l})} = p^{(\mathrm{g})}$. In case of a curved interface, one finds the Young–Laplace equation

$$p^{(\mathrm{l})} - p^{(\mathrm{g})} = \sigma\nabla\cdot\boldsymbol{n} = \sigma(\partial_k n_k) \tag{B.53}$$

with the surface tension σ and the normal unit vector of the surface facing into the direction of the gas $\boldsymbol{n}$.

For the dynamical and therefore general case, the pressure has to be replaced by the respective stress tensor, i.e. $-p^{(x)}\delta_{ij} \to S_{ij}^{(x)}$. Additionally, if the surface tension varies along the interface, the tangential force $\nabla_{\|}\sigma$ has to be taken into account. This force, acting along the surface into the direction of increasing surface tension, is responsible for the Marangoni effect.

With the tangential Nabla operator

$$\nabla_{\|} = (\delta_{ij} - n_i n_j)\partial_j \tag{B.54}$$

the general stress balance then reads [24]

$$\boxed{\left(S_{ij}^{(1)} - S_{ij}^{(\mathrm{g})}\right) n_j = -\sigma(\partial_k n_k) n_j + (\delta_{ij} - n_i n_j)\partial_j \sigma\,.} \tag{B.55}$$

For the tangential stress balance, used for the boundary conditions model of Leypoldt (see 3.1.2), surface deformations are assumed to be absent, such that the liquid free surface is of perfect upright cylindrical shape and the normal unit vector $\boldsymbol{n}$ simply gets to the cylindrical radial unit vector $\boldsymbol{e}_r$. Additionally the fluid is considered as incompressible and the ambient gas is considered as inviscid, such that its viscous stress tensor vanish. For a tangential balance, one can neglect all radial acting forces, which are the pressure force and the Laplace pressure force for the present case. In dimensional quantities this is

$$2\mu D_{ij}^{*(1)} n_j - (\delta_{ij} - n_i n_j)\partial_j \sigma = 0 \tag{B.56}$$

Recalling the Oberbeck–Boussinesq approximation with its first–order Taylor series approximation of the surface tension $\sigma = \sigma(T^*) \approx \sigma_0 - \gamma(T^* - T_0)$ and by using the common scales, equation (B.56) gets to

$$2\rho_0 \nu \frac{\nu}{d^2} D_{ij}^{(1)} n_j + \frac{\gamma \Delta T}{d}(\delta_{ij} - n_i n_j)\partial_j T = 0\,. \tag{B.57}$$

From here the thermocapillary Reynolds number

$$\mathrm{Re} = \frac{\gamma d}{\rho_0 \nu^2}\Delta T \tag{B.58}$$

has its origin. By renaming $D_{ij}^{(1)} \to D_{ij}$ one finds the final dimensionless equation

$$2D_{ij} n_j + \mathrm{Re}(\delta_{ij} - n_i n_j)\partial_j T = 0 \tag{B.59}$$

or in coordinate-free notation for the present cylindrical geometry with the radial unit vector as normal vector

$$\boxed{2\mathbf{D} \cdot \boldsymbol{e}_r + \mathrm{Re}(\mathbf{I} - \boldsymbol{e}_r \boldsymbol{e}_r) \cdot \nabla T = 0\,.} \tag{B.60}$$

B.5 Discrete Fourier transform

Given is a set of N (assumed as even) equally spaced data points $\{a_k\}$ of a real and $T-$periodic signal in position space, i.e.

$$a_k = a(\phi_k) = a(k\delta) \qquad , \qquad k = 0, \ldots, N-1 \qquad , \qquad \delta = \frac{T}{N} \,. \tag{B.61}$$

The discrete Fourier transform (DFT) of this data set with the MATLAB built-in function `fft` brings N complex Fourier coefficients

$$\{\tilde{a}_k\} \qquad , \qquad k = 0, \ldots, N-1 \qquad , \qquad \tilde{a}_k \in \mathbb{C} \,. \tag{B.62}$$

The DFTs from position space to fourier space and vice versa are defined as [15]

$$\tilde{a}_k = \sum_{n=0}^{N-1} a_n \mathrm{e}^{-\frac{2\pi \mathrm{i}}{N} kn} \qquad , \qquad a_k = \frac{1}{N} \sum_{n=0}^{N-1} \tilde{a}_n \mathrm{e}^{\frac{2\pi \mathrm{i}}{N} kn} \,. \tag{B.63}$$

The expansion of the exponent by δ in the formula of the inverse transform yields

$$a_k = a(\phi_k) = \frac{1}{N} \sum_{n=0}^{N-1} \tilde{a}_n \mathrm{e}^{\frac{2\pi \mathrm{i}}{N\delta} nk\delta} = \frac{1}{N} \sum_{n=0}^{N-1} \tilde{a}_n \mathrm{e}^{\frac{2\pi \mathrm{i}}{T} n\phi_k} \tag{B.64}$$

and by replacing the discrete variable ϕ_k with the continuous position space variable ϕ, one finds the interpolation function $a(\phi)$ for the discrete data set $\{a_k\}$. Taking into account $T = 2\pi$ and $\tilde{a}_n = |\tilde{a}_n| \mathrm{e}^{\mathrm{i}\varphi_n}$ with $\varphi_n = \mathrm{Arg}(\tilde{a}_n)$, the interpolation function gets to

$$a(\phi) = \frac{1}{N} \sum_{n=0}^{N-1} |\tilde{a}_n| \mathrm{e}^{\mathrm{i}\varphi_n} \mathrm{e}^{\mathrm{i}n\phi} \,. \tag{B.65}$$

Due to the reality of the position space signal, almost all Fourier coefficients appear as complex conjugate pairs, i.e.

$$\tilde{a}_n = \tilde{a}^*_{N-n} \qquad , \qquad n = 1, \ldots, n_{\mathrm{max}} \qquad , \qquad n_{\mathrm{max}} = \frac{N}{2} - 1 \tag{B.66}$$

In (B.66) the zero-component $\tilde{a}_0$ is excluded, because it represents the constant fraction and has to be real at all, such that the phase φ_0 is either $\varphi_0 = 0$ or $\varphi_0 = \pi$ and contains the sign only.

Another important and helpful characteristics of the DFT is the relation

$$\tilde{a}_{N-n} = \tilde{a}_{-n} \qquad , \qquad n = 1, \ldots, n_{\mathrm{max}} \tag{B.67}$$

which allows the so-called **wrapping**, a reordering process of all Fourier components $\tilde{a}_k$ with index $k \in [\frac{N}{2}+1, N-1]$. For the considered real function, equation (B.66) together with (B.67) yields

$$\tilde{a}^*_n = \tilde{a}_{N-n} = \tilde{a}_{-n} \qquad , \qquad n = 1, \ldots, n_{\mathrm{max}} \tag{B.68}$$

and therefore the interpolation function (B.65) can be written as

$$a(\phi) = \frac{1}{N}\left\{|\tilde{a}_0|\mathrm{e}^{\mathrm{i}\varphi_0} + \sum_{n=1}^{n_{\max}} |\tilde{a}_n| \left(\mathrm{e}^{\mathrm{i}(\varphi_n + n\phi)} + \mathrm{e}^{-\mathrm{i}(\varphi_n + n\phi)}\right)\right\}. \tag{B.69}$$

Finally this reads in real notation

$$\boxed{a(\phi) = \frac{1}{N}\left\{|\tilde{a}_0| \cos\varphi_0 + 2\sum_{n=1}^{\frac{N}{2}-1} |\tilde{a}_n| \cos(n\phi + \varphi_n)\right\}.} \tag{B.70}$$

According to the theorem of Nyquist a continuous position space signal which contains modes up to $n_{\max}$ requires for a full reconstruction at least $N = 2(n_{\max}+1)$ equally spaced data points.

C Manual for MTrace

The particle trajectories are determined by **MTrace**, an ODE-solver developed for the recent purpose only. This chapter should give a short overview of the internal structure, the input and output data for quick orientation.

C.1 Structure

The main script for the calculation of the trajectories is `MTrace.m`, generating one output file for every single trajectory. The reading procedure is decomposed to `f_readparam.m`, reading the user-defined data from `MTrace.dat`, and `f_readfluid.m`, reading the flow field data from the ASCII-file `flowdata.dat`. Additionally there are some secondary functions addressed by the mentioned scripts as shown below.

- `MTrace.m` ⟶ `Tr_X_StY_rhoZ_NN.dat`
  - `f_readparam.m` ⟵ `MTrace.dat`
  - `f_readfluid.m` ⟵ `flowdata.dat`
    - `f_FT.m`
    - `f_iFT.m`
  - `f_trace.m`
  - `f_event.m`

For fast post processing within MATLAB, its highly recommended to import the ASCII file `Tr_X_StY_rhoZ_NN.dat` to a MAT-file by the usage of `import_mat.m`. The result are 4 MAT-files, holding the state vectors of all imported trajectories (`yXX.mat`) and the events (`eXX.mat`) in cartesian (`xCa.mat`) and cylindrical (`xCy.mat`) coordinates.

- `import_mat.m` ⟶ `yCa.mat`, `eCa.mat`, `yCy.mat`, `eCy.mat`
  - `f_read.m` ⟵ `Tr_X_StY_rhoZ_NN.dat`

To generate `flowdata.dat` in ASCII format, one has to run the FORTRAN 90 script `import.f90` with the original binary Poseidon output file `flowdata.2`.

Secondary functions

The functions concerning the Fourier transform, `f_FT.m` and `f_iFT.m`, are only a few lines of code and easy to understand. Both functions are required in case the mode filter is on (`flag_DFT`=1), whereas `f_FT.m` performs a DFT from position space to Fourier space and `f_iFT.m` performs the inverse DFT from Fourier space back to position space again, but with user-defined modes (`modes`) only.

The functions `f_trace.m` and `f_event.m` are required by the ODE-solver. In `f_trace.m` most of the `MTrace.m` overall-calculation (exclusive of MATLAB's built-in functions) is done, where at least 80% of all lines are addressed to the interpolation procedure of the flow field. The rest represents the calculation of the values necessary for the ODE-solver's next integration step. A modification of the equations of motion is in principle easy and can be done at the end of the file. In case the reader wants to rebuild the interpolation scheme, a detailed analysis of the code is required, which should not be contents of this manual.

Finally the function `f_event.m` is required either for the reinitialization of the particle state, as the particle hits any boundary or for simple documentation, as the particle crosses any user-defined hyper-surface in phase space. Every MATLAB ODE-solver `odeXXx` supports the option **events** as an implemented subroutine. One can find some more explanation and examples by searching `odeset` in MATLAB help. For the present case `f_event.m` is essential for the implementation of the particle-boundary interaction.

f_readparam.m

The user-defined ASCII-file `MTrace.dat` contains all primary parameters for the calculation and is read by `f_readparam.m`. A short description of all input parameters is given in table C.1 and a representative `MTrace.dat`-file is shown in table C.2.

Table C.1: Description of all input parameters in `MTrace.dat`

MATLAB character	thesis char.	description of character	possible values
`Stokes`	St	Stokes number	real
`rho`	ϱ	particle-fluid density ratio	real
`flag_g`	–	gravity: $0g = 0$, $1g = 1$	0 / 1
`Froude`	Fr	Froude number	real
`Omega`	Ω	angular velocity of HTW	real
`datafilename`	–	filename of Poseidon's output file (ASCII)	char
`flag_old`	–	reading strategy: regular = 0, old = 1	0 / 1
`flag_DFT`	–	filter of flow field: on = 1, off = 0	0 / 1
`no of modes`	–	number of selected modes	integer
`modes`	n	Definition of all modes, which should be included in the flow field.	integers
`method`	–	pre-interpolation method	**linear** / spline
`RT`	–	positive exponent of rel. error for ODE-solver	integer
`AT`	–	positive exponent of abs. error for ODE-solver	integer
`refl_r`	–	PER (0) or FER-model (1) in rad. direction	**0** / 1
`refl_z`	–	PER (0) or FER-model (1) in vert. direction	**0** / 1
`tstart`	–	temporal start of integration	real
`tfinal`	–	temporal abort of integration	real
`tres`	–	temporal resolution of output data	real

The `datafilename` must not refer to Poseidon's original binary output file (suffix: .2), but to the converted ASCII file. The conversion has to be done with the FORTRAN 90 script `import.f90`. If a file is converted by `import.f90`, then `flag_old = 0`. Nevertheless there are sill some old files, converted to ASCII differently, where one would have to set `flag_old = 1`.

If the flow field data should pass the filtering procedure, one has to set `flag_DFT = 1`. Then the user has to tell the reading procedure how many modes there are to read in `modes` with the value `no of modes`. At last, `modes` holds all selected modes for the inverse Fourier transform (Note that $n = 0$ is included anyway!) .

Its highly recommended to use `method = linear` as pre-interpolation method and the PER-model in both cases, i.e. `refl_r = refl_z = 0`.

Table C.2: `MTrace.dat`-file

```
Stokes:        5.0e-5
rho:           1.0
flag_g:        0
Froude:        0
Omega:         -10.145

datafilename:  Pr4Re18_new.dat
flag_old:      0

flag_DFT:      1
no_of_modes:   3
modes:         3 6 9

method:        linear

RT:            6
AT:            8

refl_r:        0
refl_z:        0

tstart:        0
tfinal:        4
tres:          1.0E-3
```

f_readfluid.m

This script reads and prepares all data concerning the liquid bridge, which is in detail:

1. Reading the data from Poseidon's output (ASCII).
2. Preparing the coordinate vectors of the staggered grid and doing some basic calculations concerning the boundaries.
3. Appliance of the filter procedure to the flow field (if selected).

Table C.3: Overview of some important internal variables generated by `f_readfluid.m`

MATLAB character	thesis character	description of character	method of enquiry
`Nr`	N_r	radial resolution	read
`Nz`	N_z	vertical resolution	read
`Nphi`	N_φ	azimuthal resolution	read
`Vr`	u_r	radial velocity field	read/calc.
`Vz`	u_z	vertical velocity field	read/calc.
`Vphi`	u_φ	azimuthal velocity field	read/calc.
`T`	T	temperature field	read/calc.
`P`	p	pressure field	read/calc.
`r_stag`	–	radial coordinate vector	read
`r_center`	–	radial coordinate vector	calculated
`phi_stag`	–	azimuthal coordinate vector	read
`z_stag`	–	vertical coordinate vector	read
`z_center`	–	vertical coordinate vector	calculated
`z_centerE`	–	vertical coordinate vector	calculated
`R`	R	radius of liquid bridge	read
`Gamma`	Γ	aspect ratio of liquid bridge	calculated
`a`	a	particle radius	calculated
`R_star`	$R^\dagger$	contact radius	calculated
`z_star`	$z^\dagger$	vertical contact position	calculated

MTrace.m

In contrast to all other mentioned files, where a inspection of the code by the reader is definitely not necessary, a more detailed view to the code of the (still very short) main file `MTrace.m` is not avoidable. Especially the allocation of the particle's initial positions is designed to be flexible and has to be carried out by the user.

The results of every single trajectory are written to the ASCII file `Tr_X_StY_rhoZ_NN.dat`, where the placeholders of the filename stand for

1. `X`: mode filter is on (`X=f`) or off (`X=o`)
2. `Y`: Stokes number multiplied by 10^5

3. `Z`: density ratio ϱ
4. `NN`: number of trajectory (typically corresponding to initial angle in degree)

The contents of the output-file is shown in table C.4. Additionally some essential parameters used by the simulation are written in a self-explanatory way at the end of the file.

Table C.4: Output variables included in `Tr_X_StY_rhoZ_NN.dat`

MATLAB character	description of character
`size output`	length of trajectory's time vector
`tout`	time vector of trajectory
`yout`	state vector of trajectory $\boldsymbol{Y}(t) = (r, \varphi, z, \dot{r}, \dot{\varphi}, \dot{z}\ )$
`size events`	length of event's time vector
`ieout`	vector with event's identification code (ID)
`teout`	time vector of events
`yeout`	state vector of events $\boldsymbol{E}(t) = (r, \varphi, z, \dot{r}, \dot{\varphi}, \dot{z}\ )$

import_mat.m

With this script, one can import the ASCII data of several trajectories to MAT-files, standing out due to a high access rate. As mentioned at the beginning of this manual, these 4 MAT-files correspond to matrices holding the state vectors of the trajectories (`yXX.mat`) and events (`eXX.mat`) in cartesian (`xCa.mat`) and cylindrical (`xCy.mat`) coordinates.

An increase of the row number corresponds to an increase in time, the allocation of the column numbers can be seen from table C.5 and the allocation of the third matrix index corresponds to the number of the trajectory.

One should keep in mind that the cylindrical matrices hold the azimuthal velocities u_φ instead of $\dot{\varphi}$ as in the ASCII output file.

The event-function `f_event.m` in its original form contains the documentation of events summarized in table C.6. The function can be easily adapted by the user individually.

Table C.5: Allocation of columns in matrices for all MAT-files generated by `import_mat.m`

MAT-file	1	2	3	4	5	6	7	8
`yCa.mat`	t	x	y	z	u_x	u_y	u_z	
`eCa.mat`	t	ID	x	y	z	u_x	u_y	u_z
`yCy.mat`	t	r	φ	z	u_r	u_φ	u_z	
`eCy.mat`	t	ID	r	φ	z	u_r	u_φ	u_z

Table C.6: Decoding table for vector `ieout`

ID	description
1	radial contact point at $R^\dagger$
2	vertical contact point at $\pm z^\dagger$
3	radial release point from $R^\dagger$
4	vertical release point from $\pm z^\dagger$
5	top-down piercing point of trajectory at $z = 0$
6	bottom-up piercing point of trajectory at $z = 0$

C.2 Staggered data handling

Due to the staggered grid all matrices holding the field variables are of different size. Here is a short overview of the internal data management of MTrace.

Basically Poseidon is working with an individual grid resolution of $N_r \times N_\varphi \times N_z$. These values are the numbers of cell layers in each direction or in other words the number of cell centers in each direction.

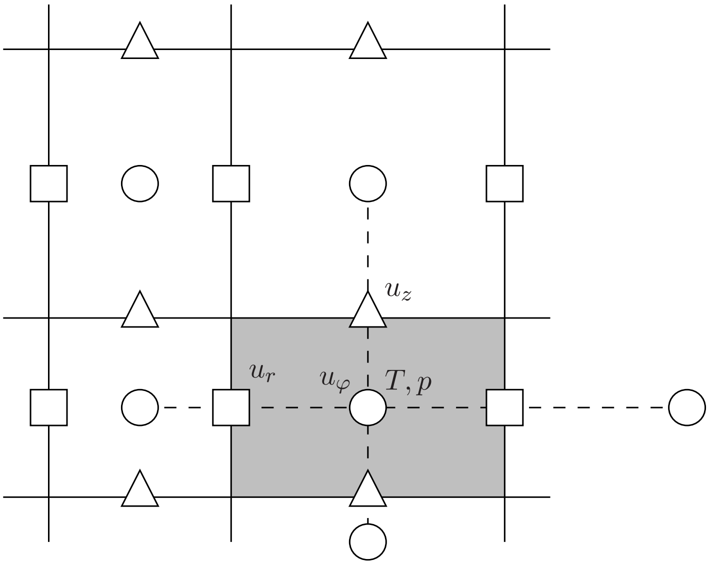

Figure C.1: Staggered grid with the arrangement of all flow field variables, (○ - u_φ, T, p), (△ - u_z) and (□ - u_r). Taken from Leypoldt [9].

In radial direction two coordinate vectors are to distinguish. Firstly `r_stag` indicates the position of the cell boundaries and secondly `r_center` holds the radial positions of the cell centers, i.e.

$$\texttt{r\_stag} = \left[0, \ldots, r_i^{(\mathrm{s})}, \ldots, \frac{1}{\Gamma}\right] \qquad i = 1, \ldots, N_r + 1 \tag{C.1}$$

$$\texttt{r\_center} = \left[\ldots, r_j^{(\mathrm{c})} = \frac{1}{2}(r_{j+1}^{(\mathrm{s})} - r_j^{(\mathrm{s})}), \ldots\right] \qquad j = 1, \ldots, N_r\,. \tag{C.2}$$

For the azimuthal direction only one coordinate vector is needed, holding the equally spaced angles φ_k, which is

$$\texttt{phi\_stag} = \left[\ldots, \varphi_k = \frac{2\pi}{N_\varphi}(k-1), \ldots\right] \qquad k = 1, \ldots, N_\varphi\,. \tag{C.3}$$

In axial direction there are, similar to the radial direction, again two coordinate vectors. The vertical positions of the cell boundaries are indicated with `z_stag` and the vertically centered positions are written in `z_center`, i.e.

$$\texttt{z\_stag} = \left[0.5, \dots, z_l^{(\mathrm{s})}, \dots, -0.5\right] \qquad l = 1, \dots, N_z + 1 \tag{C.4}$$

$$\texttt{z\_center} = \left[\dots, z_m^{(\mathrm{c})} = \frac{1}{2}(z_{m+1}^{(\mathrm{s})} - z_m^{(\mathrm{s})}), \dots\right] \qquad m = 1, \dots, N_z\,. \tag{C.5}$$

The no-slip condition at the upper and lower disks, at $z = \pm 0.5$ where all velocity components vanish, allows an extension of the centered data vector `z_center` to the extended vector `z_centerE`. This brings some advantages for the interpolation. All calculations concerning u_r, u_φ and T are done with the extended vector, which is then

$$\texttt{z\_centerE} = [0.5,\ \texttt{z\_center}\ , -0.5]\ . \tag{C.6}$$

Table C.7: Size of all coordinate vectors

r_stag	$N_r + 1$
r_center	N_r
phi_stag	N_φ
z_stag	$N_z + 1$
z_center	N_z
z_centerE	$N_z + 2$

Table C.8: Coordinate allocation and matrix size of the flow field variables

	z	r	φ	matrix size				
u_r	z_centerE	r_stag	phi_stag	$(N_z + 2)$	×	$(N_r + 1)$	×	N_φ
u_φ	z_centerE	r_center	phi_stag	$(N_z + 2)$	×	N_r	×	N_φ
u_z	z_stag	r_center	phi_stag	$(N_z + 1)$	×	N_r	×	N_φ
p	z_center	r_center	phi_stag	N_z	×	N_r	×	N_φ
T	z_centerE	r_center	phi_stag	$(N_z + 2)$	×	N_r	×	N_φ

The matrix size is denoted as the matrices appear in MATLAB. This was done in the most intuitive way, this means r is increasing by increasing the column number, z is decreasing by increasing the row number and φ is increasing by increasing the third matrix index.

Bibliography

[1] G. Haller and T. Sapsis. Where do inertial particles go in fluid flows? *Physica D*, 237:573–583, 2008.

[2] D. Schwabe, A. I. Mizev, M. Udhayasankar, and S. Tanaka. Formation of dynamic particle accumulation structures in oscillatory thermocapillary flow in liquid bridges. 19:072102–1–072102–18, 2007.

[3] D. Schwabe, P. Hintz, and S. Frank. New features of thermocapillary convection in floating zones revealed by tracer particle accumulation structures (PAS). 9:163–168, 1996.

[4] S. Tanaka, H. Kawamura, I. Ueno, and D. Schwabe. Flow structure and dynamic particle accumulation in thermocapillary convection in a liquid bridge. 18:067103–1–067103–11, 2006.

[5] I. Ueno, Y. Abe, K. Noguchi, and H. Kawamura. Dynamic particle accumulation structure (PAS) in half-zone liquid bridge - Reconstruction of particle motion by 3-D PTV. *Adv. Space Res.*, 41:2145–2149, 2008.

[6] D. Schwabe, S. Tanaka, A. Mizev, and H. Kawamura. Particle accumulation structures in time-dependent thermocapillary flow in a liquid bridge under microgravity conditions. 18:117–127, 2006.

[7] M. K. Smith and S. H. Davis. Instabilities of dynamic thermocapillary liquid layers. Part 1. Convective instabilities. 132:119–144, 1983.

[8] J. Leypoldt, H. C. Kuhlmann, and H. J. Rath. Three-dimensional numerical simulation of thermocapillary flows in cylindrical liquid bridges. 414:285–314, 2000.

[9] J. Leypoldt. *Dreidimensionale numerische Simulation thermokapillarer Strömungen in zylindrischen Flüssigkeitsbrücken.* PhD thesis, Universität Bremen, 1999.

[10] J. Leypoldt, H. C. Kuhlmann, and H. J. Rath. Stability of hydrothermal-wave states. *Adv. Space Res.*, 29:645–650, 2002.

[11] P. G. Drazin and W. H. Reid. *Hydrodynamic Stability.* Cambridge University Press, 2 edition, 2004.

[12] M. R. Maxey and J. J. Riley. Equation of motion for a small rigid sphere in a nonuniform flow. *Phys. Fluids*, 26:883–889, 1983.

[13] A. Babiano, J. H. E. Cartwright, O. Piro, and A. Provenzale. Dynamics of a small neutrally buoyant sphere in a fluid and targeting in Hamiltonian systems. *Phys. Rev. Lett.*, 84:5764–5767, 2000.

[14] Stefano Domesi. *Numerical analysis of particle dynamics in the thermocapillary flow of liquid bridges.* PhD thesis, Universität Bremen, 2009.

[15] MATLAB. Help Manual, Release R2007a.

[16] Wolfgang Haidinger. Anwendung und Dokumentation des Matlab BDF-Codes ode15s zur numerischen Lösung von steifen Differentialgleichungen. Master's thesis, TU Wien, 2000.

[17] Nikolina D. Vassileva, Dirk van den Ende, Frieder Mugele, and Jorrit Mellema. Capillary forces between spherical particles floating at a liquid-liquid interface. *Langmuir*, (21):11190–11200, 2005.

[18] M. Do-Quang, A. Carlson, and G. Amberg. Capillary force dominated impact of a solid sphere onto a liquid free surface. In S. Colin and G. L. Morini, editors, *Proceedings of the 1st European Conference on Microfluidics*, Bologna, 2008. Societe Hydrotechnique de France.

[19] D. Melnikov. Private communication.

[20] H. Kawamura. Private communication with group member I. Ueno.

[21] H. C. Kuhlmann. *Thermocapillary Convection in Models of Crystal Growth*, volume 152 of *Springer Tracts in Modern Physics.* Springer, Berlin, Heidelberg, 1999.

[22] J. Leypoldt. User's Manual for Poseidon, 2002.

[23] H. Schlichting and K. Gersten. *Grenzschicht-Theorie.* Springer, 1997.

[24] H. C. Kuhlmann and C. Nienhüser. The influence of static and dynamic free-surface deformations on the three-dimensional thermocapillary flow in liquid bridges. In R. Narayanan and D. Schwabe, editors, *Interfacial fluid dynamics and transport processes*, volume 628 of *Lecture Notes in Physics*, pages 213–239. Springer, Berlin, Heidelberg, 2003.